ISTANBUL TECHNICAL UNIVERSITY ★ GRADUATE SCHOOL OF SCIENCE ENGINEERING AND TECHNOLOGY

NUMERICAL AND EXPERIMENTAL INVESTIGATION ON THE CRUSHING BEHAVIOUR OF AUXETIC LATTICE CELLS PRODUCED WITH ADDITIVE MANUFACTURING TECHNIQUES

Ph.D. THESIS

Kadir GÜNAYDIN

Aeronautics and Astronautics Engineering Department

Aeronautics and Astronautics Engineering Programme

APRIL 2020

ISTANBUL TECHNICAL UNIVERSITY ★ GRADUATE SCHOOL OF SCIENCE ENGINEERING AND TECHNOLOGY

NUMERICAL AND EXPERIMENTAL INVESTIGATION ON THE CRUSHING BEHAVIOUR OF AUXETIC LATTICE CELLS PRODUCED WITH ADDITIVE MANUFACTURING TECHNIQUES

Ph.D. THESIS

Kadir GÜNAYDIN
(511132111)

Aeronautics and Astronautics Engineering Department

Aeronautics and Astronautics Engineering Programme

Thesis Advisor: Prof. Dr. Halit Süleyman TÜRKMEN
Co-advisor: Assist. Prof. Dr. Antonio Mattia GRANDE

APRIL 2020

İSTANBUL TEKNİK ÜNİVERSİTESİ ★ FEN BİLİMLERİ ENSTİTÜSÜ

EKLEMELİ İMALAT TEKNİKLERİ İLE ÜRETİLMİŞ ÖKZETİK KAFES YAPILARIN EZİLME DAVRANIŞLARININ NÜMERİK VE DENEYSEL OLARAK İNCELENMESİ

DOKTORA TEZİ

Kadir GÜNAYDIN
(511132111)

Uçak ve Uzay Mühendisliği Anabilim Dalı

Uçak ve Uzay Mühendisliği Programı

Tez Danışmanı: Prof. Dr. Halit Süleyman TÜRKMEN
Eş Danışman: Dr. Öğr. Üyesi Antonio Mattia GRANDE

NİSAN 2020

Kadir GÜNAYDIN, a Ph.D. student of ITU Graduate School of Science Engineering and Technology 511132111 successfully defended the thesis entitled "NUMERICAL AND EXPERIMENTAL INVESTIGATION ON THE CRUSHING BEHAVIOUR OF AUXETIC LATTICE CELLS PRODUCED WITH ADDITIVE MANUFACTURING TECHNIQUES", which he prepared after fulfilling the requirements specified in the associated legislations, before the jury whose signatures are below.

Thesis Advisor :	**Prof. Dr. Halit Süleyman TÜRKMEN** Istanbul Technical University	.....
Co-advisor :	**Assist. Prof. Dr. Antonio Mattia GRANDE** Politecnico Di Milano	.....
Jury Members :	**Prof. Dr. Hasan KURTARAN** Adana Alparslan Türkeş Science and Technology University	.....
	Prof. Dr. Vedat Ziya DOĞAN Istanbul Technical University	.....
	Assist. Prof. Dr. Özge ÖZDEMİR Istanbul Technical University	.....
	Assist. Prof. Dr. Demet BALKAN Istanbul Technical University	.....
	Assist. Prof. Dr. Sedat SÜSLER Kocaeli University	.....

Date of Submission :
Date of Defense : **03 April 2020**

To my auntie Aysel Canci and my family,

FOREWORD

First of all, I would like to express my deepest gratitude to my supervisors Prof. Dr. Halit Suleyman TURKMEN and Prof. Antonio Mattia GRANDE for their endless and kind supports during my Ph.D. research. Especially, I would like to mention my sincere thanks to Prof. Antonio Mattia GRANDE for providing an excellent research environment with his constructive comments and suggestions at Politecnico Di Milano. I would also like to express my special gratitude to Prof. Dr. Giuseppe SALA, who is the head of Department of Aerospace Science Technology (DAER) of Politecnico Di Milano, for his special role for me to be a part of DAER during my Ph.D. Additionally, I would like thank to dear Aerospace Materials and Technologies (AMATECH) laboratory members, especially the laboratory head of Silvio Ferragina and test engineer of Paulo Rubini for testing and production supports. Lastly, I would like to gratefully acknowledge the support of The Scientific and Technological Research Council of Turkey (TÜBİTAK) due to its International Research Fellowship Program (1059B141700425) support and of Istanbul Technical University for the projects of Science Research Projects (BAP) 40611 and Researcher Development Program (ITU-AYP-2016-2).

Another important person who supported me is the jury member of Prof. Dr. Hasan KURTARAN. I am appreciated about his motivational and guidance supports. Also, special thanks go to Prof. Alessandro AIROLDI and Dr. Chiara MIRANI for their helps in simulations, Dr. Alessandro DE GASPARI for his equipment support for analyses, and Prof. Dr. Zafer KAZANCI for his motivational support.

Last of all, I would like to thank Prof. Dr. Tomasso GHIDINI, the head of European Space Agency (ESA) Structures, Mechanisms and Materials Division, for his special course of Additive Manufacturing for Space and Aerospace Applications, professional guidance and motivational supports.

Nisan 2020 Kadir GÜNAYDIN

TABLE OF CONTENTS

Page

FOREWORD ..... **ix**
TABLE OF CONTENTS ..... **xi**
ABBREVIATIONS ..... **xiii**
SYMBOLS ..... **xv**
LIST OF TABLES ..... **xvii**
LIST OF FIGURES ..... **xix**
SUMMARY ..... **xxiii**
ÖZET ..... **xxvii**
1. INTRODUCTION **1**
1.1 Purpose of Thesis 3
1.2 Literature Review 4
1.3 Hypothesis 7
1.4 Organization of Thesis 8
2. FDM FOR POLYMERS AND FDM PRINTING PROBLEMS **11**
2.1 Introduction 11
2.2 Printing Errors in FDM 13
2.2.1 Misalignment of the print platform 14
2.2.2 Misalignment of the nozzle 15
2.2.3 Depletion of printing material or disrupted material flow 16
2.2.4 Lack or loss of adhesion to the print platform 17
2.2.5 Vibration and shock 17
2.2.6 Inaccurate adjustments of printer settings 18
2.3 Mechanical Properties of FDM Printed ABS Parts 18
2.4 Overview and Discussion 21
3. CRUSH BEHAVIOUR OF FDM PRINTED POLYMERIC AUXETIC LATTICES **23**
3.1 Introduction 23
3.2 Lattice Geometries 23
3.2.1 Anti-tetrachiral 25
3.2.2 Re-entrant 27
3.3 Experimental Setup 29
3.4 Numerical Analyses 31
3.5 Crush Theory 33
3.6 Results 35
3.6.1 Experimental results for anti-tetrachiral and regular re-entrant 35
3.6.2 Experimental results for anti-tetrachiral and modified re-entrant 38
3.6.3 Deformation modes for anti-tetrachiral and modified re-entrant lattices. 39

3.6.4 Comparison of experimental and numerical results 41
3.7 Benchmark Study 45
3.7.1 Validation study 45
3.7.2 Results 47
3.8 Overview and Discussion 48
4. CRUSH BEHAVIOUR OF AUXETIC FILLED TUBES 51
4.1 Introduction 51
4.2 Deformation Modes for Composite Tubes 52
4.3 FEM Material Models 54
4.3.1 Hashin's failure criteria for composites 54
4.4 Material 56
4.5 Experiments and Results 57
4.6 Overview and Discussion 65
5. EBM TECHNOLOGY FOR CHIRAL LATTICE PRODUCTION AND COMPRESSION ANALYSES 67
5.1 Electron Beam Melting 67
5.2 Material Classification and Tests 69
5.2.1 Lack of Fusion 78
5.2.1.1 Effect of lack of fusion on mechanical performance 80
5.3 Effects of LOF Area to Mechanical Performance 82
5.3.1 Constitutive equation 87
5.4 Chiral Auxetic Cell Production, Tests and Analyses 89
5.4.1 Introduction 89
5.4.2 Material and processing 90
5.4.3 Chiral cellular structures 91
5.4.4 Mechanical characterization and tests 93
5.4.5 Numerical Analysis 96
5.5 Results 98
5.6 Overview and Discussion 106
6. CONCLUSIONS AND RECOMMENDATIONS 109
6.1 Practical Application of This Study 111
REFERENCES 113
APPENDICES 127
APPENDIX A.1: Build Theme for EBM Printed Ti6Al4V ELI 129
APPENDIX A.2: Arcam A2 Properties 130
APPENDIX A.3: Fixture Design for Chiral Cyclic Test 131
APPENDIX A.4: Subroutine for Boundary Conditions 132
CURRICULUM VITAE 137

ABBREVIATIONS

ASTM	**:** American Society for Testing Materials
AM	**:** Additive Manfucaturing
SLS	**:** Selective Laser Sintering
SLA	**:** Streolithography
FDM	**:** Fused Deposition Manufacturing
EBM	**:** Electron Beam Melting
ABS	**:** Acrylonitrile Butadiene Styrene
PLA	**:** Polylactic Acid
STL	**:** Streolithography
Ti6Al4V	**:** Titanium Alloy
ELI	**:** Extra Low Interstitial
LOF	**:** Lack of Fusion
NPR	**:** Negative Poisson's Ratio
SEA	**:** Specific Energy Absorption
EA	**:** Absorbed Energy
CFE	**:** Crush Force Efficiency
CF	**:** Carbon Fibre
FRP	**:** Fiber Reinforced Polymer
FEM	**:** Finite Element Methods
SEM	**:** Scanning Electron Microscopy
GPa	**:** Giga-Pascal
MPa	**:** Mega-Pascal
mm	**:** Milimeter
gr	**:** Grams

SYMBOLS

L_x	: Ligament length along the x direction
L_y	: Ligament length along the y direction
r, d_o	: Radius of the node
d_i	: Inner radius of the node
h	: Chiral lattice cell flatwise length
t	: Wall thickness of the ligaments and nodes
b, e	: The depth of the cell
E_x	: Elastic modulus along the x direction
E_y	: Elastic modulus along the y direction
E_z	: Elastic modulus along the z direction
E_c, E_s	: Elastic modulus constituent material
ρ	: Density of base material
ρ_c	: Lattice structure density
A_n	: Node areas of each unit cell
A_i	: Ligament areas of each unit cell
A_j	: Junction areas of each unit cell
$\alpha, \beta, \eta, \lambda$	: Geometrical non-dimensional parameters I
μ, γ	: Geometrical non-dimensional parameters II
β', θ'	: Topology parameters
θ	: Internal cell angle
l	: Inclined wall length
L	: Ligament length
P	: Load
δ	: Crush displacement

LIST OF TABLES

Page

Table 2.1 : Melting temperature and FDM temperatures of ABS and PLA..... 13
Table 2.2 : The effect of the layer thickness to the tensile stress, specific stress, Young modulus and specific modulus. 21
Table 3.1 : Geometrical parameters of the manufactured anti-tetrachiral samples (all in mm)..... 26
Table 3.2 : Geometrical parameters of the manufactured modified re-entrant samples..... 28
Table 3.3 : Material properties of the 3D printing specimens. 31
Table 3.4 : CFE and SEA values of a)hexachiral (chiral) b)tetrachiral c) anti-tetrachiral d) trichiral e) anti-trichiral f) regular honeycomb. 48
Table 4.1 : Crush properties of hollow and filled composite tubes under axial crush. 64
Table 4.2 : Properties of the hollow and filled composite tubes under lateral crush. 64
Table 5.1 : Chemical specifications of Arcam Ti6Al4V ELI. 69
Table 5.2 : EBM production variables. 70
Table 5.3 : Dimensions of the unit chiral cells. 93
Table 5.4 : Dimensions of C1 and C2 as design, asbuilt and sandblasted (*D - design, A - asbuilt, S - sandblasted). 100
Table 5.5 : Crush indexes for C1 and C2. 103
Table A.1 : Build theme for EBM printed Ti6Al4V ELI. 129
Table A.2 : Arcam A2 properties. 130

LIST OF FIGURES

Page

Figure 1.1 : Classification of cellular solids. 2
Figure 1.2 : Re-entrant auxetic structure in a) undeformed and b) deformed states. 4
Figure 1.3 : Organization of thesis. 9
Figure 2.1 : Illustration of FDM 3D printing. 12
Figure 2.2 : Adhesion problem of layers. 14
Figure 2.3 : Shifted layers. 15
Figure 2.4 : Uncompleted part caused by lack of filmanet. 16
Figure 2.5 : FDM printed ABS tensile specimens. 19
Figure 2.6 : Stress-strain diagram for all layer thicknesses. 20
Figure 3.1 : 2D auxetic lattice types. 24
Figure 3.2 : Anti-tetrachiral unit cell a) iso-view b) front-view c) manufactured sample. 26
Figure 3.3 : Re-entrant hexagonal unit cell a) iso-view b) front-view c) manufactured sample. 28
Figure 3.4 : Tensile test setup using the method of advanced video extensometer. 30
Figure 3.5 : Tensile test results of the ABS material. 30
Figure 3.6 : Production of anti-tetrachiral and re-entrant hexagonal samples. 31
Figure 3.7 : Anti-tetrachiral lattice system a) front-view b) perspective-view. 32
Figure 3.8 : Re-entrant hexagonal lattice system a) front-view b) perspective-view. 32
Figure 3.9 : Produced anti-tetrachiral and regular re-entrant lattices. 35
Figure 3.10 : Crushed anti-tetrachiral and regular re-entrant lattices. 35
Figure 3.11 : Re-entrant hexagonal 1 and anti-tetrachiral auxetic structures load – deflection graph. 36
Figure 3.12 : Deformed anti-tetrachiral auxetic lattice structure. 36
Figure 3.13 : Deformed re-entrant auxetic lattice structure.. 37
Figure 3.14 : Produced modified re-entrant lattice. 37
Figure 3.15 : First re-entrant hexagonal and second re-entrant hexagonal auxetic structures load – deflection graph. 37
Figure 3.16 : Deformed auxetic structure 2 (re-entrant hexagonal 2). 38
Figure 3.17 : a) Force-deflection b) mean crushing force-deflection c) energy absorption-deflection curves of anti-tetrachiral lattices at 10 mm/min velocity. 39
Figure 3.18 : a) Force-deflection b) mean crushing force-deflection c) energy absorption-deflection curves of re-entrant hexagonal lattices at 10 mm/min velocity. 39

Figure 3.19: a) Force-deflection b) mean crushing force-deflection c) energy absorption-deflection curve comparison between anti-tetrachiral and re-entrant hexagonal structure at 10 mm/min velocity. 39
Figure 3.20: Critical crushing times of the anti-tetrachiral lattices. 40
Figure 3.21: Critical crushing times of the modified re-entrant hexagonal lattices. 41
Figure 3.22: Comparison between numerical and experimental results of anti-tetrachiral lattices. 42
Figure 3.23: Comparison between numerical and experimental results of re-entrant lattices 43
Figure 3.24: The deflection images of the samples at every 30 seconds from the initial to the final state at 180 seconds. 44
Figure 3.25: The deformation pattern comparison of the experimental and FEM results. 46
Figure 3.26: The comparison of the experimental and FEM results for validation. 47
Figure 3.27: a) hexachiral (chiral) b) tetrachiral c) anti-tetrachiral d) trichiral e) anti-trichiral f) regular honeycomb 48
Figure 4.1 : Collapse Modes [120]. 53
Figure 4.2 : Chiral axuetic lattice a) production stage b) topology parameters. ... 56
Figure 4.3 : Chiral structure filled composite tube. 56
Figure 4.4 : Produced chiral lattice and its uniaxial and lateral crush of chiral auxetic lattices. 57
Figure 4.5 : Force – displacement curves related to the in-plane crush of chiral lattices. 58
Figure 4.6 : Force – displacement curves related to the out-of-plane crush of chiral lattices. 58
Figure 4.7 : Crushing stages of hollow (A) and chiral lattices filled (B) tubes..... 59
Figure 4.8 : Force – displacement curves related to the hollow composite tubes. 59
Figure 4.9 : Deformed (A, B, C) hollow and chiral (D, E, F) lattices filled composite tubes. 60
Figure 4.10: Axial force – displacement diagram for the chiral lattices filled composite tubes. 61
Figure 4.11: Deformed hollow and chiral lattices filled composite tubes under lateral loading. 61
Figure 4.12: Lateral force – displacement curves for the hollow composite tubes. 62
Figure 4.13: Lateral force – displacement curves for the chiral-filled composite tubes. 63
Figure 4.14: Three different (A, B, C) lateral crushing processes of the chiral lattices filled composite tubes. 63
Figure 5.1 : Floating parts production in EBM: (a)iso view and (b) front view. .. 68
Figure 5.2 : EBM building chamber zones. 70
Figure 5.3 : Tensile specimens and MTS 810 material test system. 71
Figure 5.4 : Mechanical specifications versus production angles. 72
Figure 5.5 : Stress – Strain graphs for 0, 45 and 90 production degrees. 73
Figure 5.6 : 90-degree production with lowest breaking strain. 74
Figure 5.7 : 90-degree production with highest breaking strain. 75
Figure 5.8 : 45-degree production with lowest breaking strain. 76

Figure 5.9 : 45-degree production with highest breaking strain. 76
Figure 5.10 : 0-degree production with lowest breaking strain..... 77
Figure 5.11 : 0-degree production with highest breaking strain. 77
Figure 5.12 : Lack of fusion a) unfused complete powder particles b)semi-fused zones..... 78
Figure 5.13 : Failure surface of a) below part (fixed) and b) above part (pulled).. 79
Figure 5.14 : Influence of the direction of loading on the severity of a lack of fusion [145]..... 81
Figure 5.15 : The effect of defect area ratio to Young's modulus..... 83
Figure 5.16 : The effect of defect area ratio to yield stress..... 84
Figure 5.17 : The effect of defect area ratio to ultimate strength and fracture strength..... 85
Figure 5.18 : The effect of defect area ratio to breaking strain..... 86
Figure 5.19 : EBM printed parts: (a) printed parts in powder cake (b) as-built and sandblasted chiral parts (c)as-built and sandblasted tensile specimens..... 91
Figure 5.20 : Hexagonal chiral unit lattice: (a) geometrical parameters and (b) unit cel..... 93
Figure 5.21 : Flexural test fixture..... 94
Figure 5.22 : Fixture for chiral lattice compressionl..... 94
Figure 5.23 : Crush test setup and specimens of a) 0.8 mm b) 1.6 mm ligament thicknessed chiral unit cells. 95
Figure 5.24 : Specimens, strain gauge properties and test setup..... 95
Figure 5.25 : Compressive load profile for chiral lattices. 96
Figure 5.26 : Unit cell boundary conditions..... 98
Figure 5.27 : Cross-sections for a) 90-degree, 0.8 mm thickness b) 0-degree, 0.8 mm thicknessa) c) 90-degree, 1.6 mm thickness d) 0-degree, 1.6 mm thickness. 99
Figure 5.28 : Load-deflection curves for 0-degree and 90-degree build orientation specimens for bending test..... 101
Figure 5.29 : Compressive load profile experimental and FEM results for chiral unit cells of a) 0.8 mm thickness b) 1.6 mm thickness. 102
Figure 5.30 : Compressive load and deflection graph chiral unit cell with a ligament thickness of a) 0.8 mm b) 1.6 mm. 103
Figure 5.31 : FEM and experimental results for the crush of chiral unitcells of a) 0.8 mm thickness b) 1.6 mm thickness..... 104
Figure 5.32 : Comparison of FEM and experimental deformation stages for the crush of chiral unitcells of a) 0.8 mm thickness b) 1.6 mm thickness. 106
Figure A.1 : Fixture design for chiral cyclic test. 131

NUMERICAL AND EXPERIMENTAL INVESTIGATION ON THE CRUSHING BEHAVIOUR OF AUXETIC LATTICE CELLS PRODUCED WITH ADDITIVE MANUFACTURING TECHNIQUES

SUMMARY

In aerospace, automotive, marine, and military applications, low-density lightweight structures such as sandwich structures and filling materials have an important role in crashworthy applications due to their crush resistance during impact and blast situations. Large deformation can occur during the impact, blast and crush events; therefore sandwich structures and sacrificial crash tubes can bottom out and very high peak load can rise. For preventing this phenomenon, auxetic materials have drawn attention as a core and filling material due to their negative Poisson's ratio (NPR) specification, which provides lateral expansion under tensile loads and shrinkage under compressive loads. The purpose of this study is to examine the energy absorption characteristics of additively manufactured polymer and metal 2D auxetic lattice cells, in the edgewise direction where auxeticity can be experienced, subjected to axial quasi-static loads. Total mass and volume of lattice cell structures are kept almost equal for better comparison.

In the work presented in this dissertation, additive manufacturing (AM) is used to produce auxetic lattice structures. AM is an improved method for quick and complex productions, and layered manufacturing is the most common method for AM; aiming the design verification, visualization, and kinematic functionality testing. AM is a computer-controlled manufacturing method of needed parts which are directly transferred as a solid model from the computer. It is a very sufficient and proved way to reduce the time for product development. There are several methods for AM, which are selective laser sintering (SLS), electron beam melting (EBM), fused deposition modelling (FDM) and stereolithography (SLA). FDM is used in this study because of its device and consumption material are cheaper compared to other mentioned methods. On the contrary of advantages of FDM method, there are some uncontrollable production problems to be solved such as incomplete bottom layers, hanging strands, missing walls, pillowing, shifted layers, unfinished parts, delamination of layers, warping syndrome, burn marks and irregular walls. In this study, FDM production problems are listed and investigated. Furthermore, solution approaches are presented to prevent those production flaws. Zortrax M200 3D printing device and Acrylonitrile butadiene styrene (ABS) are used in this study. NX 12: Siemens PLM Software is used for designing the representation of a solid model then it is converted to a stereolithography (STL) file. The converted file is then imported to the machine software of Zortrax which is called Z-Suite. For the FDM productions, production variables are defined as high quality, maximum infill, normal seam, and no support usage. Different layer thicknesses of the productions are assigned as 0.09, 0.14, 0.19, 0.29 and 0.39 mm. Several specimens in each group are manufactured to determine the effect of the layer thickness on the tensile

properties. As a result, stress-strain graphs are obtained, and the effect of printing options to mechanical properties are investigated to define the feasible layer thickness for producing structures.

Consequently, it is understood that ABS is not enough ductile to maintain the auxeticity of the structures for a certain period. Thus, electron beam melting (EBM) is used in this study. It is one of the promising and sophisticated AM techniques that uses an electron beam to melt metallic powders. Titanium alloy (Ti6Al4V) is used by the reason of its outstanding mechanical properties of high specific strength, high corrosion resistance, excellent biocompatibility; hence titanium alloys are prominent material for aerospace and bioengineering fields. ARCAM EBM A2 3D printing machine and ARCAM Ti6Al4V ELI, which is a gas atomized prealloyed powder in a size range of 45-100 μm, are used in this study. To understand the mechanical behaviour and characterize EBM printed parts tensile tests are conducted. Each test specimens are produced in three different directions, 0^o, 45^o and 90^o due to characteristic anisotropic behaviour of EBM printed parts. Moreover, a study on the effect of inner defects, which are detected as the lack of fusion, in the EBM printed parts is conducted to define the mechanical performance of EBM printed components. The area of defect regions are observed using a scanning electron microscope and measured to investigate the defect area effect to mechanical performance. As a result, EBM printed Ti6Al4V parts experiences isotropic elasticity and yield stress, however, strain at break specifications show substantial differences according to build orientation which is dominated by the lack of fusion (LOF) problems. As an output, it is understood that the increase in the LOF region shows an almost linear decreases pattern with the strain at break value.

Furthermore, firstly a comparative study with re-entrant and anti-tetrachiral auxetic is conducted to define the better auxeticity mechanism for 2D auxetic lattices. However, anti-tetrachiral auxetic structures show greater results than the re-entrant auxetic structures and, a modification for the re-entrant structure is needed to increase its energy absorption ability. Besides, another 2D auxeticity mechanism, which is called rotating rigid auxeticity, exists, however, this type of structure is not feasible for crushing applications due to bulky parts in the structure so it is not counted in this study. A comparative compression investigation of anti-tetrachiral and modified re-entrant lattices is conducted in-plane direction using experimental and numerical analyses. Lattice structures are manufactured using FDM 3D printing technology and crushed at the quasi-static condition. Non-linear finite element (FE) models of both structures are established, and the FE results are systematically compared with the experimental results. The onset of densification phases of both structures is determined numerically. Results indicate that deformation modes strongly affect the force-deflection response of both designs. In this manner, failure regions and buckling deformation in the tests are identified to find a relation with theory and to modify geometries. The anti-tetrachiral design exhibits higher specific energy absorption than modified re-entrant hexagonal lattices. Beyond the auxetic characteristics, deformation mechanism of the anti-tetrachiral lattices provides an opportunity to construct excellent crush absorption in-plane direction thanks to its high shear strength stem from its unique deformation mechanism. After having the validated constitutive equation for FDM printed ABS, a benchmark test is conducted using ABAQUS commercial finite element method (FEM) software to evaluate and define the energy absorption effective chiral mechanism among hexachiral, trichiral, anti-trichiral, tetrachiral, anti-tetrachiral and regular hexagonal topologies. As a result, hexachiral (chiral) auxetic lattice

is selected, and a part of the study is devoted to the understanding of the energy absorption characteristics of filled chiral auxetic lattices cylindrical composite tubes subjected to a uniaxial and lateral quasi-static load. The lattice structures are manufactured using an FDM 3D printing technique and ABS material. Composite tubes without filling material are initially subjected to uniaxial and lateral quasi-static crushing loads at a rate of 10 mm/min. The same types of experiment are then performed on chiral lattices and chiral lattices filled composite tubes. For the different cases, the load-displacements curves are analyzed and the specific energy absorption (SEA) values are compared. The SEA capability for the axial quasi-static crushing of the chiral lattices filled composite tubes reach 43 J/kg with a 45% decrease in comparison with the hollow composite design. On the contrary – and quite remarkably - the average SEA value in the case of lateral loading is 2.36 J/kg, with a 450% increase in comparison with the hollow composite configuration.

Finally, chiral auxetic unit cell structures are produced from Titanium Alloy (Ti6Al4V) metallic powder using Electron Beam Melting (EBM) additive manufacturing technology. EBM printed chiral auxetic lattices are compressed with a three steps cyclic load profile in the edgewise direction numerically and experimentally. Also, a crush study is performed numerically and experimentally to evaluate the energy absorption ability of EBM printed metallic chiral lattice cells. For material characterization and understanding the material behaviour of EBM printed parts tensile and three-point flexural tests are conducted. Tensile and bending specimens are produced in two different thicknesses and orientations. Moreover, a surface roughness study is conducted due to high surface roughness of EBM printed parts, and an equation is offered to define load-carrying effective area for preventing cross-section measurement mistakes. In compliance with the equation and tensile test products, a constitutive equation is formed and used in the numerical analyses after selection and calibration process. The constitutive equation is verified by the comparison of experimental and numerical three-point bending test results. Furthermore, a compressive load profile is applicated to the EBM printed chiral lattice unit cells with two different thicknesses to track their Poisson's ratio variation, and displacement limit under large displacements without the formation of degradation, permanent deformations and failures. The utilization of a finite element code to verify a numerical model for optimum topology design and mechanical performance forecast, the same scenarios investigated in the compressive load profile experiments are then evaluated using non-linear computational models. In the computational models, a Fortran subroutine is used to define the load and displacement controls. In addition, in the numerical crush analysis, auxetic lattice cells are crushed between two rigid plates using damage and failure criteria for simulating failures. As a result, it is revealed that the thickness of the chiral lattice cells is the dominating parameter about its stiffness and auxeticity. Increase in the chiral node radius to thickness rate of 0.15 to 0.30 causes loss of auxetic behaviour. Lastly, their compression behaviours are compared, and the one showing auxeticity presents better energy absorption ability in terms of crush force efficiency, however, considering specific energy absorption value the results show the opposite.

EKLEMELİ İMALAT TEKNİKLERİ İLE ÜRETİLMİŞ ÖKZETİK KAFES YAPILARIN EZİLME DAVRANIŞLARININ NÜMERİK VE DENEYSEL OLARAK İNCELENMESİ

ÖZET

Havacılık, otomotiv, denizcilik ve askeri uygulamalarda, sandviç yapılar ve dolgu malzemeleri gibi düşük yoğunluklu hafif yapılar, darbe ve patlama durumlarında ezilme dirençleri göz önünde bulundurulduğunda önemli bir role sahiptirler. Çarpma, patlama ve ezilme olayları durumunda büyük deformasyonlar meydana gelebilir; bu nedenle sandviç yapılar ve kaza tüpleri tükenebilir ve yüksek pik kuvvetleri ortaya çıkabilir. Bu durumu önlemek için ökzetik malzemeler önemli bir role sahiptir. Ökzetik malzemeler, klasik malzeme davranışının aksine çekme yükleri altında yanal genişleme ve basma yükleri altında yanal daralma davranışı gösteren negatif Poisson oranlı malzemeler olmaları nedeniyle çekirdek ve dolgu malzemesi olarak dikkat çekmektedir. Bu çalışmanın amacı eksenel sanki-statik yüklere maruz kalan eklemeli imalat yöntemleri ile üretilmiş polimer ve metal ökzetik kafes yapıların enerji emilim özelliklerini ökzetiklik gösterdikleri doğrultuda incelemektir. Bu çalışma yapılırken kafes yapıların toplam kütlesi ve dış hat ölçümleri daha etkili karşılaştırma çalışması yapılabilmesi için eş tutulmaya çalışılmışılmıştır.

Bu tezde sunulan çalışmada ökzetik kafes yapıları üretmek için eklemeli imalat yöntemi kullanılmıştır. Eklemeli imalat yöntemi hızlı ve karmaşık üretimler için geliştirilmiş bir yöntemdir ve katmanlı üretim eklemeli imalat için en yaygın yöntemlerden biridir. Ek olarak tasarım doğrulaması, görselleştirme ve kinematik işlevsellik testi gibi amaçlar için birçok yönden avantaj sağlayan bir üretim yöntemidir. Eklemeli imalatta bilgisayarda oluşturulan katı model doğrudan aktarılarak gerekli parçaların bilgisayar kontrolü ile etkili bir üretim yöntemidir. Ürün geliştirme süresini azaltmanın yanı sıra uygulanabilirliği yüksek ve kanıtlanmış bir üretim yöntemidir. Eklemeli imalat için seçici lazer sinterleme, elektron ışını ergitme, eriyik yığma modelleme ve stereolitografi olmak üzere çeşitli yöntemler vardır. Eriyik yığma modelleme tekniği; cihaz ve sarfiyat malzemelerinin bahsedilen diğer yöntemlere göre daha ucuz olması ve daha fazla kullanıcıya ulaşan bir yöntem olması nedeniyle bu çalışmada kullanılmıştır. Eriyik yığma yönteminin belirtilen avantajlarının aksine, tamamlanmamış alt katmanlar, asılı sarkıtlar, eksik duvarlar, yastıklama, kaydırılmış katmanlar, bitmemiş parçalar, katmanların ayrılması, çözgü sendromu, yanma izleri ve düzensiz duvarlar gibi çözülmesi sorun teşkin eden bazı üretim sorunları vardır. Bu çalışmada, eriyik yığma metodu üretim sorunları listelenmiş ve incelenmiştir. Ayrıca, bu üretim kusurlarını önlemek için çözüm yaklaşımları sunulmaktadır. Eriyik yığma metodu üretimleri için Zortrax M200 3B yazdırma cihazı ve sarf malzemesi olarak Akrilonitril bütadien stiren (ABS) kullanılmıştır. NX 12: Siemens PLM 3B modelleme yazılımı katı modellerin temsilini tasarlamak için kullanılmıştır ve ardından stereolitografi (STL) dosyasına dönüştürülmüştür. Dönüştürülen dosya daha sonra Z-Suite adı verilen Zortrax'ın makine yazılımına aktarılmıştır.

Eklemeli imalatta üretim parametreleri üretilen yapının mekanik özellikleri üzerine etkisi yüksek olması sebebi ile optimum üretimlerin yapılabilmesi üzerine çalışma yapılmıştır. Bu çalışmada belirtilen bazı parametreler sabit tutulurken bazıları değiştirilerek çekme testleri yapılmıştır. Eriyik yığma modelleme tekniği ile yapılan üretimlerde sabit olan üretim parametreleri maksimum dolgu, normal dikiş ve desteksiz üretim olarak tanımlanmıştır. Kontrol edilebilir parametrelerden olan ve mekanik özellikler için önemli bir etken olan katman kalınıkları için farklı katman kalınlıkları olarak 0.09, 0.14, 0.19, 0.29 ve 0.39 mm belirlenmiştir. Katman kalınlığının üretilen malzemenin mekanik özellikleri üzerindeki etkisini belirlemek için her grupta belirli sayılarda numuneler üretilerek çekme testleri yapılmıştır. Sonrasında, gerilim-gerinim grafikleri elde edilmiş ve yazdırma seçeneklerinin mekanik özelliklere etkisi ve yapıların üretilmesi için en uygun katman kalınlığının etkisi üzerine çalışılmış ve kafes yapıların üretiminde kullanılmıştır.

Sonuç olarak çalışmada kullanılan ABS malzemelerin; ökzetik yapıların ökzetik davranışlarının belirli bir süre devam edebilmesi için yeterli derecede sünek olmadığı anlaşılmıştır. Bu nedenle farklı uygulamalarda ve farklı malzeme ile aynı yapının vereceği cevaplar için çalışmada diğer bir katmanlı imalat yöntemi olan elektron ışını ergitme yöntemi kullanılmıştır. Elektron ışını ergitme metodu metalik tozları ergitmek için elektron ışını kullanan sofistike eklemeli imalat tekniklerinden biridir ve elektron ışını ergitme cihazı yanı sıra malzeme olarak Titanyum alaşımı (Ti6Al4V) olan yüksek özgül mukavemet, yüksek korozyon direnci, üstün biyouyumluluk gibi üstün mekanik ve kullanım özelliklerine sahip alaşım kullanılmıştır. Bu malzeme bu özellikleri dolayısıyla uzay ve biyomühendislik alanları için öne çıkan malzemelerdendir. ARCAM EBM A2 3B yazıcı ve 45-100 μm boyutundaki metal toz taneciklerden oluşan ve gaz atomizasyon yöntemi ile üretilen bir alaşım olan ARCAM Ti6Al4V ELI kullanılmıştır. EBM ile üretilen parçaların karakterize edilmesi ve mekanik davranışının anlaşılabilmesi için çekme testleri yapılmıştır. EBM ile üretilen parçalar izotropik olmayan davranış gösterdiği için 0^o, 45^o and 90^o olarak üç oryantasyonda üretim yapılmıştır. Ayrıca, EBM ile üretilmiş parçalarda füzyon eksikliği olarak tespit edilen iç kusurların üretilen parçaların mekanik etkisi üzerine bir çalışma yapılmıştır. Üretilen parçaların içindeki iç hataları gözlemlemek ve hataların büyüklüklerini ölçmek için tarayıcı elektron mikroskobu kullanılarak bunların mekanik performansa etkisine bakılmıştır. Sonuç olarak EBM ile üretilen Ti6Al4V parçalar izotropik elastisite ve akma dayanımı gösterirken kopma uzamalarında füzyon problemleri kaynaklı büyük farklılıklar görülmüştür. Çalışmanın çıktısı olarak füzyon eksikliğinden kaynaklı oluşan bölgelerin toplam alanı ile kopma uzamaları arasında neredeyse lineer bir bağlantı görülmüştür.

Ökzetikler ile ilgili çalışmalara gelindiği zaman ilk çalışma girintili altıgen kafes yapı ile anti-tetrakiral ökzetik yapılar eriyik yığma yöntemi ile ABS'den üretilere ezme testleri yapılıp 2B ökzetik yapıyı oluşturan mekanizmalardan hangisinin ezilme yönünden daha işlevsel olduğu üzerine bir çalışma yapılmıştır. Bu çalışmaya bir diğer ökzetik mekanizması olan dönen rijit ökzetik kafes yapı olan ve içerisinde yüksek dolgulu geometriler içeren yapıların ezilme açısından verimli olmaması ile dahil edilmemiştir. 2B ökzetik yapılar eriyik yığma ve elektron ışınlı ergitme gibi katmanlı imalat yöntemleri için uygun geometrilerdir. Üretim tablası üzerinde ekstrüzyon yapılarak üretimleri sağlanabilir. 3B gibi kompleks yapılar üretilmek istendiğinde yapının boş olan iç kısımlarında ve çevresinde destek yapıları kullanmak gerekmektedir. Bu yapıların üretim sonunda el yordamı ile

temizlenmesi gerekmektedir. Kompleks geometrilerde bazı ulaşılamayan bölgelerden temizlenemezken bazı bölgelerde temizlik sonrası yüzeyde oluşan bozulmalar yük altında gerilme yığılması ve çatlak oluşumu gibi mekanik problemlere sebebiyet vermektedir.

Girintili altıgen kafes yapı ile anti-tetrakiral ökzetik yapıların ezilme davranışları kıyaslandığında girintili altıgen kafes yapının ezilme davranışının düşük olması sebebi ile geometrisinde modifikasyona gidilmiştir. Bu modifikasyondan sonra anti-tetrakiral ve modifiye edilmiş girintili altıgen kafes yapıların karşılaştırmalı ezme araştırması deneysel yöntem ve sayısal analizler kullanılarak ökzetiklik gösterdikleri doğrultuda gerçekleştirilirmiştir. Kafes yapılar eriyik yığma 3B yazdırma teknolojisi kullanılarak üretilmiş ve yarı-statik yük altında ezilmiştir. Her iki yapının doğrusal olmayan sonlu elemanlar modelleri ABAQUS ticari sonlu elemanlar yazılımı kullanılarak oluşturulmuş ve sonlu elemanlar sonuçları sistematik olarak deneysel sonuçlarla karşılaştırılmıştır. Ezme sonucunda ezilen yapılar ezilmenin ilk fazında lineer elastik bir davranış gösterirken, ikinci fazında plato ve son fazından yoğunlaşma denilen fazlar sergilemektedir. İlk fazda eğilme etkili deformasyon modu iken ikinci fazla burkulma, plastik deformasyon, gevrek kırılmalar meydana gelir. Son fazda ise kafes yapının içindeki boşluklar kapanarak yapı yığın bir malzeme gibi davranmaya başlar. Yapının absorbe ettiği toplam enerji hesaplanırken bu yoğunlaşma noktasından öncesi hesaba katılır. Bu çalışmada her iki yapının yoğunlaşma fazlarının başlangıcı sayısal olarak belirlenmiştir. Sonuçlar deformasyon modlarının her iki tasarımın kuvvet-deplasman cevabını güçlü bir şekilde etkilediğini göstermektedir. Bu şekilde, testlerdeki kırılma bölgeleri ve burkulma deformasyonu teori ile bir ilişki bulmak ve geometrilerin modifikasyonu için tanımlanmıştır. Anti-tetrakiral tasarım, modifiye edilmiş girintili kafes altıgen yapılardan daha yüksek özgül enerji emilimi sergilemektedir. Ökzetik karakteristiğinin ötesinde anti-tetrakiral ökzetik yapılar deformasyon mekanizlarından kaynaklı yüksek kesme kuvveti dayanımı sayesinde ezilme altında yüksek özgül enerji emilimi sağlamaktadılar. Eriyik yığma üretim metodu ile üretilen ABS malzeme için deneysel ve nümerik analiz ile korelasyon sağlanıp oluşturulan nümerik analiz modelinin validasyonu yapıldıktan sonra hekzakiral, trikiral, anti-trikiral, tetrakiral, anti-tetrakiral gibi kiral deformasyon mekanizması içeren yapılar arasındaki enerji emilimi yönünden en etkili kiral mekanizmayı değerlendirmek, bal peteği yapı ile kıyaslamak için ABAQUS ticari sonlu elemanlar yöntemi (FEM) yazılımı kullanılarak kıyaslama testi yapılmıştır. Sonuç olarak hekzakiral (kiral) ökzetik kafes seçilmiştir ve çalışmanın bir kısmı tek eksenli ve yanal yarı-statik yüke maruz kalan dolgulu kiral ökzetik kafes yapı dolgulu silindirik kompozit tüplerinin enerji emme karakteristiklerinin anlaşılmasına ayrılmıştır. Kafes yapılar eriyik yığma modelleme tekniği kullanılarak üretilmiştir. Dolgu malzemesi içermeyen boş kompozit tüpler başlangıçta tek eksenli ve yanal yarı-statik ezme yükleri altında 10 mm/dakika hızında deformasyona maruz bırakılmıştır. Aynı deneyler daha sonra kiral yapılar ve kiral ökzetik yapı ile doldurulmuş kompozit tüpler üzerinde gerçekleştirilir. Farklı durumlar için yük-deplasman eğrileri analiz edilirek özgül enerji emilim değerleri karşılaştırılır. Kiral kafeslerle doldurulmuş kompozit tüplerin eksenel yarı statik ezilmesi için özgül enerji emilimi kapasitesi içi boş kompozit tasarıma kıyasla %45'lik bir azalma ile 43 J/kg'a ulaşılmıştır. Aksine - ve oldukça dikkat çekici bir şekilde - yanal yükleme durumunda ortalama özgül enerji emilimi değeri içi boş kompozit konfigürasyonuna kıyasla %450'lik bir artışla 2.36 J/kg'dır.

Kafes yapılar kendilerini oluşturan ve birbirini tekrarlayan en küçük yapılar olan birim hücrelerin oluşturduğu ağ ile ortaya çıkmaktadır. Bu birim hücrelerde yapılan değişiklikler kaynaklı ortaya çıkan mekanik özellik değişimleri tüm yapıyı etkilemektedir. Bu sebeple de çalışma birim hücre üzerindeki çalışmaya indirgenerek kiral ökzetik kafes yapıların birim hücreleri elektron ışın ergitme üretim teknolojisi kullanılarak Titanyum alaşımı (Ti6Al4V) metalik tozdan üretilmiştir. Elektron ışın ergitme ile üretilen kiral ökzetik kafes yapılar sayısal ve deneysel olarak ökzetiklik gösterdiği doğrultuda üç aşamalı çevrimsel yük profili ile basma kuvvetine maruz bırakılmıştır. Ayrıca EBM ile üretilmiş Ti6Al4V alaşımlı kiral ökzetik yapıların enerji emme özelliklerini belirleyebilmek için ezme testi yapılmıştır. Malzeme karakterizasyonu ve elektron ışın ergitme ile üretilen parçaların malzeme davranışlarını anlamak için çekme ve üç nokta eğme testleri yapılmıştır. Çekme ve eğme test örnekleri iki farklı kalınlık ve üretim oryantasyonu doğrultusunda üretilmiştir. Ayrıca elektron ışın ergitme baskılı parçaların yüksek yüzey pürüzlülüğü nedeniyle yüzey pürüzlülüğü çalışması yapılmış ve kesit ölçüm hatalarının önlenmesi için yükü taşıyan etkin alanını tanımlamak için tarayıcı elektron mikroskobu ile etkin alanlar belirlenip bir eşitlik sunulmuştur.

Eşitlik ve çekme testi sonuçları kullanılarak seçim ve kalibrasyon işleminden sonra yapısal bir denklem nümerik analiz için oluşturulmuş ve kullanılmıştır. Yapısal eşitlik denklemi deneysel ve sayısal üç nokta eğme testi sonuçlarının karşılaştırılması ile doğrulanmıştır. Ayrıca elektron ışınlı ergitme ile üretilen kiral ökzetik birim hücreler iki farklı kalınlıkta üretilirek farklı yükler altında Poisson oranı değişimi ve büyük deformasyonlarda lineer olmayan deformasyon sınırını, hasar ve kalıcı deformasyonlar olmaksızın izlemek için bir basma yük profili uygulanmıştır. Optimum topoloji tasarımı ve mekanik performans tahmini için sayısal modeli doğrulamak amacıyla sonlu eleman kodunun kullanılmış ve daha sonra basma yük profili deneylerinde incelenen aynı senaryolar doğrusal olmayan hesaplama modelleri kullanılarak değerlendirilmiştir. Hesaplamalı modellerde yük ve yer değiştirme sınır şartları kontrollerini tanımlamak için bir Fortran altyordamı kullanılmıştır. Ezme testleri analizlerin kiral yapıların ezilmesi sırasında ortaya çıkan kırılmaların simülasyonunu yaparak daha iyi sonuçlar elde edebilmek için hasar kriterleri kullanılmıştır. Sonuç olarak kiral kafes hücrelerin kalınlığı, rijitliği ve ökzetikliği konusunda etkin bir parametre olduğu deneysel olarak belirlenmiştir. Kiral ökzetik kafes yapıyı oluşturan silindir yapıların duvar kalınlığı-yarıçapı oranı olan değerin 0.15'ten 0.30'a olan oran artışı ökzetik davranış kaybına neden olmuştur. Son olarak ezilme davranışları karşılaştırılmıştır ve ökzetiklik gösteren yapının ezme kuvveti etkinlik oranında daha iyi enerji emilim kabiliyeti sağlandığı özgül enerji emilim değerinde ise tam tersine bir davranış gösterdiği görülmüştür.

1. INTRODUCTION

Impact phenomenon can be encountered in many occasions such as bird hit to an aircraft, debris or meteoroid impacts in space, ballistic impact on a protection shield, traffic accidents and military applications, etc. There are several studies to prevent or reduce the harmful effects of impact on the people and vital parts of the structures or vehicles. Every year, the vast majority of people are injured or killed by trauma which is caused by impacts, drops, falls and blasts. It is known that the trauma is the globally third commonest cause of death, and 12% of the reason for global disease burden [1]. Besides, almost ever-increasing terrorist attacks are started to highlight the importance of sacrificial structures.

In aerospace, marine, automotive and military applications, lightweight structures like sandwich and crashbox structures have an important role considering the crush resistance during an impact and blast situations. Sandwich structures usually consist of two relatively thin, stiff and robust facesheets or skins separated by a relatively thick, lightweight, low modulus core; for instance, honeycomb, balsa or foam cores. The purpose of the sandwich structure is to achieve a stiff, simultaneously light, transversely high load carrying and crashworthy components. The sandwich structures facesheets, which support bending and in-plane membrane forces, are generally made of lightweight materials such as fibre-reinforced composites and aluminium alloys. Sandwich structure cores have more importance in terms of its structure and material type because it supports most of the loads and especially the shear loads. Additionally, core structures can be used as a filling material for different applications such as crash tubes, sacrificial walls, helmets and body armours. The core structures are generally made of Nomex, fibreglass-reinforced thermoplastic, aluminium, and foam-type cores. However, improvements in additive manufacturing have provided the production of the arbitrary core structures by metals and polymers. The polymer and metallic core structures have drawn attention due to their wide range of material options and plastic deformation specifications. Polymer and metallic core structures have been used in

various fields such as aerospace, marine and transportation industry [2, 3]. The plastic deformation specifications of polymers and metals and different core geometries can improve the energy absorption capability value of the crashworthy structures. For crashworthy structures, different type of cellular core structures has been proposed, this includes foams [4–6], lattices [7–11] and trusses [12, 13]. Cellular solid structures can be grouped as shown in Figure 1.1. Cellular solid structures can be divided into two group called stochastic and non-stochastic structures. This is explained as random probability distribution and hierarchical identical distribution solid structures, respectively [14].

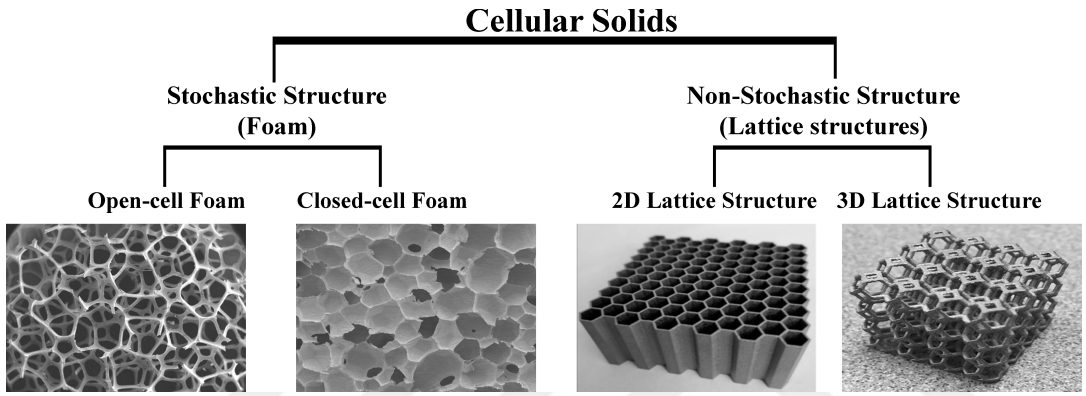

Figure 1.1 : Classification of cellular solids.

Moreover, lattice structures are known as not-stochastic hierarchical solid structures used in many fields such as aerospace applications, automobile industry and military applications due to their vibration damping and impact absorbing capabilities. They are tailored structures and can be produced in micro [4, 15–21], and macro levels [15, 22–24]. Foam structures can also be classified as macro-level structures. In crash tube applications, foam materials are generally used to increase impact absorption capability of crash tubes due to their easy implementation to different shell structures. On the other hand, macro-level lattice solid structures are generally used in sandwich structures as core materials. Thus, it is important to measure the crushing efficiency of sandwich core structures by itself since the facesheets of sandwich structures have no considerable effect on crush applications. Core structures are generally made of conventional materials and structures that show positive Poison's Ratio, however, auxetic materials have come forward for these applications because of their special specifications about showing negative Poison's Ratio - they shrink when compressed, and expand when stretched- which is very important parameter for high energy

absorbing capability during impact and crush situation [20, 21, 24, 25]. The term "auxetic" was first introduced by Evans [26] during his search for materials beyond the conventional limits. Since auxetic materials are obtained with varying geometrical parameters, they are labelled as meta-materials. By altering material cells on micro or macro levels, auxetic properties could be obtained. Regarding these alterations, interesting material properties such as negative rigidity or the negative coefficient of thermal expansion could also be obtained. The impact of these parameters on mechanical properties of materials has begun to be studied since the 2000s.

1.1 Purpose of Thesis

In aerospace, marine, automotive and military industries, thin-walled tubes and sandwich structures with different kind of cores or fillers are generally used as energy absorbing sacrificial structures. Large deformation occurs during the crash events; therefore tubes and sandwich structures can bottom out and very high peak load can occur. For preventing this phenomenon, auxetic materials have drawn attention to reduce weight and increase energy absorption of sacrifical structures. The core of this thesis study can be highlighted as understanding the additive manufacturing techniques of EBM and FDM for producing lattice cells, production problems and solutions for FDM, the lack of fusion effect for EBM printed parts, obtaining constitutive equations for FDM printed ABS and EBM printed Ti6Al4V ELI materials, determining the effective load-carrying area for the EBM printed parts, production of auxetic lattice cells using FDM and EBM, comparison of re-entrant and chiral deformation mechanisms, benchmark analysis for chiral auxetic lattice cells in terms of energy absorption ability, using chiral auxetic lattice cell as a filling material for carbon fibre reinforced composite tubes, production of chiral lattice unit cells using EBM and determining permanent deformation limitations of the chiral unit cell under low cyclic compressive loading conditions and their crush test. Furthermore, reliable numerical analyses are also established to simulate the crushing behaviour of auxetic lattice cells for being validated with the experiments. These numerical analyses allows the prediction and simulation of the behaviour of auxetic structures in a cost efficient manner. In addition, an extensive study as a part of this thesis is about crashworthiness

of tubes, and they are essential in order to investigate tubes and auxetic structure interaction during uniaxial and lateral crush.

There are several types of research related to auxetic lattice cell behaviours in the literature, however, neither of them was able to cover the content of the crush of 2D auxetic cells from additive manufacturing and analysis point of view. Thus, the merit of this dissertation study is performing determined purposes and provide a profitable concept to the research community.

1.2 Literature Review

In aerospace, automotive, marine, and military applications, low-density lightweight structures such as sandwich structures have an important role considering crush resistance during impact and blast situations. For crashworthy structures, different types of lightweight sandwich structures have been proposed with different cores such as foams, lattices, and trusses because they offer very small weight to area ratio while retaining excellent rigidity, strength, and impact energy absorption abilities [27]. The lattice cores have come forward regarding crashworthiness, and one of the most promising lattice structures are auxetic cellular solid structures [28]. Auxetic cellular solid structures are a special type of structures exhibiting negative Poisson's ratio (NPR) with anti-rubber or dilatational features by experiencing lateral expansion under tensile loads and shrinkage with the effect of compressive loads, as seen from Figure 1.2.

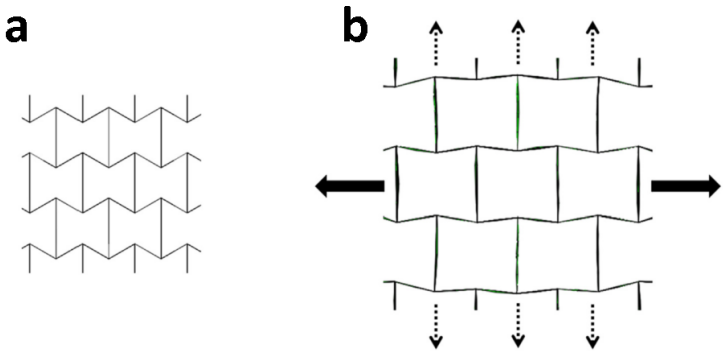

Figure 1.2 : Re-entrant auxetic structure in a) undeformed and b) deformed states.

In addition to large global flexibility and large local deformation within elastic limits, the enhanced mechanical properties of auxetic materials, can be listed compared to traditional materials as follows: (a) improved edgewise (in-plane) indentation

resistance (b) high fracture toughness (c) better transverse shear modulus [29]. Due to their superior properties, auxetic structures have been utilized in various applications such as innovative stent designs [30, 31], smart actuators, propellers, flexible microelectronics, and biomechanical devices [32, 33]. Additionally, special auxetic structures are tailored for the coefficient of thermal expansions [34]. There are several studies in the literature about NPR structures, however, the first artificial synthetic foam material having negative Poisson's ratio was introduced by Lake [35] in 1987, and the terminology of auxetic was first proposed by Evans in 1991 [28]. Structures with NPR are also termed as metamaterials because of their unique properties beyond conventional ones [18,36–40]. These unique properties are obtained through geometrical configurations. Adjusting Young's modulus or Poisson's ratio can be succeeded through modifying geometrical parameters of the unit cell, which are the repeated smallest topology of the network. Needed auxetic properties can be obtained from a wide selection of geometries, each of which may be suited better to provide a specific purpose (such as better vibration damping, acoustic insulation etc). Each of these structures needs to be studied and evaluated separately. Classification of different types of auxetic structures such as woven, foam or lattice structures can be found in the literature [41–43]. Moreover, some research has been conducted on the production of auxetic structures. Duncan et al. [44] compared auxetic foam fabrication methods considering sports safety. Wang et al. [45] introduced the interlocking assembly concept for producing 3D periodic auxetic cellular structures and compared with the former used conventional additive manufacturing methods. Li and Zeng [46] studied on an understanding of critical issues for the auxetic polyurethane (PU) foams fabrication process. Duncan et al. [47] studied the production of large (355 x 344 x 20 mm) homogenous auxetic foam sheets using thermo-mechanical conversion method with the help of pins for control the planar compression. Yuan et al. [48] presented the investigation of 3D soft auxetic lattice structures production via selective laser sintering.

Auxetic structures can be offered as crashworthy structures regarding their energy absorption characteristics that can be tuned by the change of geometrical parameters. In particular, it is known that the energy absorption capability of the cellular materials is closely related to relative density, the thickness of the cell walls and the angle

between walls [49]. Generally, hexagonal honeycomb structures are used as a core structure for sandwich structures. Nakamoto et al. [50] presented an analytical approach for the progressive and plastic in-plane collapse of hexagonal lattices. Re-entrant structures can be obtained as a result of hexagonal structures modification by changing the interior angles of adjacent cell walls greater than 180^{o}. Zhou et al. [51] investigated the plastic in-plane compression behaviour of re-entrant lattices. Several researchers introduced the elasticity equations of different lattices exhibiting NPR [17, 18, 52–55] and zero Poisson's ratio (ZPR) [56]. For instance, Chen et al. [18] calculated the in-plane elasticity equations of anti-tetrachiral lattices and compared with the experimental results. Innovative novel 2D designs of tetrachiral and anti-tetrachiral auxetic lattices were proposed by Huimini et al. [27] and Wengwang [57]. In their studies, analytical expressions are derived for the in-plane mechanical properties and validated with FEA and experimental results. A large deformation compression studies were conducted for anti-trichiral honeycomb specimens with various ligament length which are produced by ABS polymer by cutting with a laser. As a result of studies, the ratio of ligament length to node radius is to be less than 5.5 for the exhibition of auxeticity, and the increase of the ratio of the oblique ligament to horizontal ligament increases the global stress and specific energy [58, 59]. In addition, a study was conducted for the 3D isotropic anti-tetrachiral structure. An expression based on rigid cubic node rotation and kinematic deformation geometrical relation was constituted in the study by validating experimental and FEA results to obtain dimensionless geometrical parameters for tuning [60]. Moreover, 3D novel designs called chiral- chiral- antichiral and chiral- antichiral– antichiral auxetic lattices were proposed and their compression performances were compared [61]. Huang et al. [17] have studied the in-plane elasticity equation of modified re-entrant hexagonal lattices. They have modified re-entrant cells to make the structure stronger against the possible out-of-plane loading. Chen and Fu [62] modified 3D re-entrant lattices and obtained better stiffness comparing typical re-entrant design. However, there are a few experimental and numerical studies on the elastic and plastic collapse behaviour of auxetic lattice structures. Zhang et al. [21] conducted a parametric study for the dynamic crushing response of re-entrant honeycombs with different cell angles at different strain rates. Ingrole et al. [22] manufactured 3D auxetic lattices with re-entrant unite cells and investigated their in-plane static crushing response

suggesting modified re-entrant cells for better energy absorption. Zhou et al. [51] have investigated plastic collapse behaviour of metal re-entrant lattice structure by changing some geometrical parameters. Ren et al. [63] proposed a buckling induced auxetic design composed of a solid sphere and three cuboids. However, this study only deals with the elastic behaviour of the auxetic design. Additionally, some re-entrant lattice compression studies were performed under quasi-static and dynamic loads. Dong et al. [64] investigated the effect of cell-wall thickness on the deformation mode indicating that thickness greater than 0.4 mm shows deformation mode similar to thick-walled honeycombs. A numerical and experimental study [65] on the uni- and bidirectionally graded re-entrant auxetic honeycomb's compression behaviour to investigate the deformation mode and Poisson's ratio distribution, and a numerical dynamic compression research [66] on regular re-entrant auxetic honeycomb under the low, medium, and high-velocity compressions for the investigation of the effect of inertia on NPR were performed.

It has been proved that auxetic structures demonstrate high levels of specific strength. However, studies in the literature are not sufficient about the numerical and experimental study of auxetic structures produced using additive manufacturing technologies regarding crush loads. In addition, there is no study about the interaction of the tube fill material auxetic lattice structures with the composite tubes. Studies in the context of this study aim to fill the gap in the literature and productize it. With the studies in this dissertation, the crush behaviour of auxetic meta-materials will be characterised and productized as a core and filling material. Genuineness of the study will be provided by the investigation of differences of auxetic lattice structures deformation mechanisms which are claimed to have a capability of high energy absorption and how they can increase the energy absorption capacities.

1.3 Hypothesis

In this thesis, the objective is to investigate auxetic lattice structures deformation mechanisms, in the edgewise direction where auxeticity can be experienced, experimentally and numerically to determine the effective auxetic deformation mechanism and geometry. Furthermore, understanding the production process of auxetic cells using metallic and polymeric additive manufacturing techniques is

another objective in conjuction with material characterizing for understanding the material behaviours and obtaining the constitutive equations for numerical analyses. Another significant component of this thesis is understanding the effect of internal defects on mechanical performance of EBM printed Ti6Al4V, and selecting material models for elastic and plastic behaviour is another subject of thesis. Moreover, a unit cell of a chiral lattice structure with different wall thicknesses was tested with a compressive load profile at very low velocity to investigate its displacement limit by applying large displacements without experiencing permanent deformations, degradation or failures for determining the limitation of auxeticity of a chiral cell. Same unit cells are crushed and compared to understand the effect of wall thickness on the auxeticity and energy absorption. Lastly, for understanding the interaction of auxetic filling with CFR composite tube, empty and auxetic-filled tubes are axially and laterally compressed between two rigid plates during a quasi-static loading process and investigated the benefits of auxetic lattice filling to crashworthiness of CFR tubes.

1.4 Organization of Thesis

The organization of thesis can be seen in the flow chart in Figure 1.3.

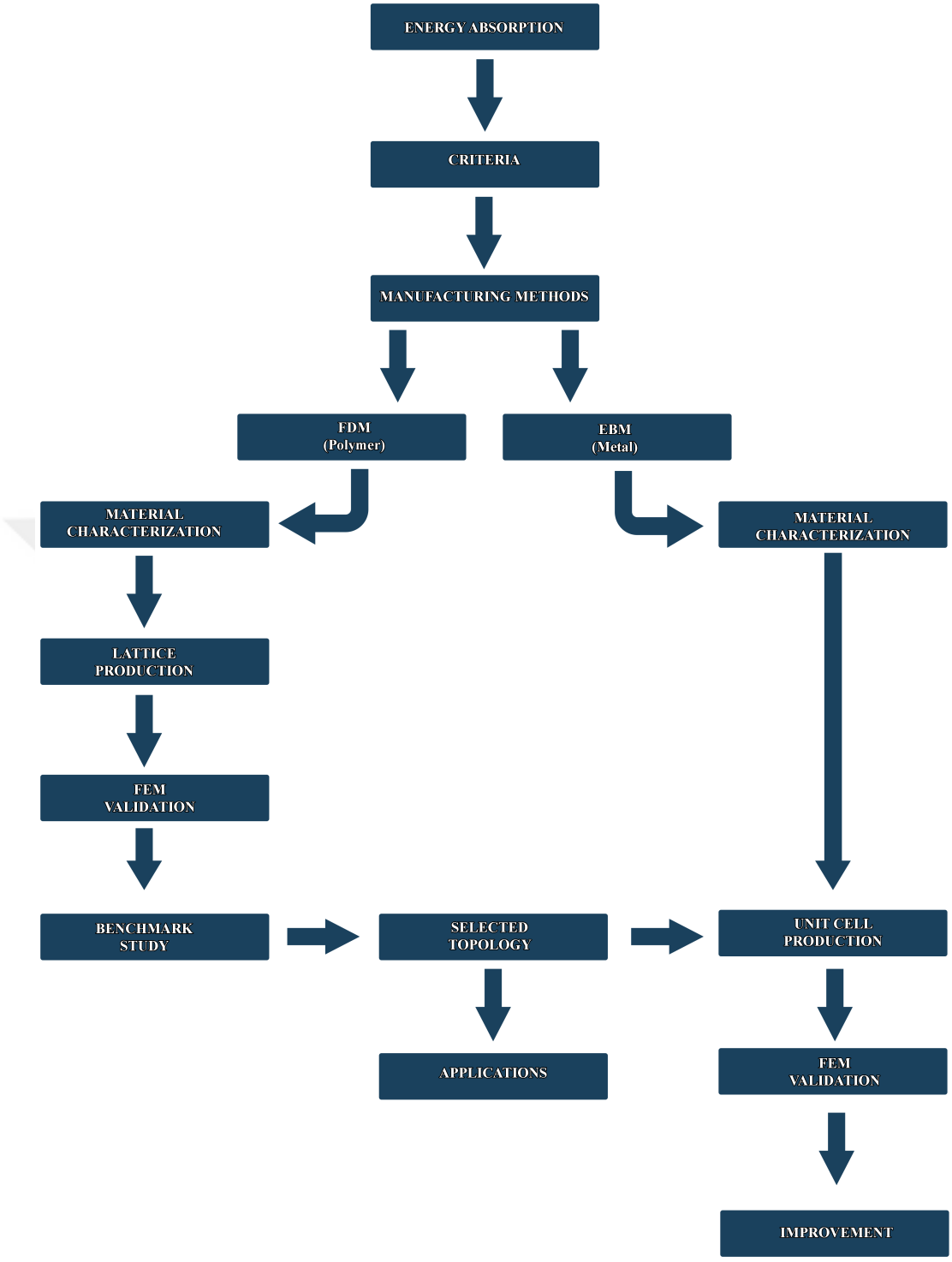

Figure 1.3 : Organization of thesis.

The main body of this dissertation is organized as a total number of five compact chapters to be understood easily and straightforward to follow. In the first chapter, introduction, literature review, hypothesis and thesis organization are took place to have an overview of the subject. In the next chapter, FDM is discussed about its abilities, printing flaws and mechanical tests to obtain FDM printed ABS constitutive

equation. In the following chapter, the production of re-entrant and anti-tetrachiral auxetic lattices using FDM is discussed, and their crush results are investigated. Moreover, in this chapter as a supplementary study, the crush performance of modified re-entrant and anti-tetrachiral auxetic structures is compared numerically and experimentally to draw a conclusion about their deformation mechanism difference in terms of crush ability. Additionally, benchmark study is conducted to define better energy absorber geometry among auxetic lattices having chiral deformation mechanism. In the fourth chapter, FDM printed ABS chiral auxetic lattice structures are used as filling material for composite and aluminium tubes to define the interaction between chiral lattice and tubes in terms of crush behaviour. In the last chapter, EBM production method, the mechanical effect of production orientation in the building chamber, the effect of internal defects on the mechanical performance, the behaviour chiral lattice cells under compressive cyclic and crush loads results for different wall thicknesses are discussed. Moreover, as a result of experimental studies for the EBM printed Ti6Al4V ELI, inputs for the constitutive equation is obtained, calibrated and imported to FEM codes to represent the behaviour of the material, and the results of numerical studies are validated with experimental results. In conclusion, all the outputs are summed up, and recommendations are presented for improvements.

2. FDM FOR POLYMERS AND FDM PRINTING PROBLEMS

2.1 Introduction

Rapid prototyping (RP) is an advanced and one of the most promising methods to produce prototypes and models which can be directly used in several fields, and layered manufacturing (LM) is the most common technique for RP aiming the design verification, visualization, and kinematic functionality testing [67, 68]. LM is a computer-controlled manufacturing method for production of arbitrary parts, and these parts are directly transferred to a 3D printer as a solid model from a computer. It is a quite sufficient and proved way to reduce the time and costs for product development and production [69]. One of the most important advantages is geometric flexibility due to the enablement of the production of complex parts comparing to other conventional methods, at the same time manufacturing costs do not increase in most of the cases [70]. There are several methods for LM, which are selective laser sintering (SLS), fused deposition modelling (FDM), stereolithography (SLA) and three-dimensional printing (3DP) [71].

Fused deposition modelling (FDM), the name itself also explains the method that the fused material is deposited in layers to produce a part, is the one of most promising RP method considering cost-effectiveness and production speed. It is widely used, and almost half of the 3D printing machines are in this category [68, 72, 73]. Dimensional accuracy is one of the important aspect in the manufacturing, and comparing with conventional manufacturing processes RP methods is inaccurate [74]. So, to increase dimensional accuracy, the method must be understood clearly to avoid undesired production problems such as skewness, and low dimensional accuracy.

The FDM method was developed in 1988 by Steven Scott Crump who also founded Stratasys and commercialized the FDM process after one year later. This company put the first 3D printing device on the market with the name of 3D Modeler in 1992. After that, several new FDM systems were introduced, and the common point of these

systems was the use of two nozzles; one is used to produce physical part material, and another one is aimed for the support material [73, 75]. The FDM process utilizes a simple mechanism for building a physical component by the addition of fused material of layers by the help of adhesion; it simply provides the phase of melting, extrusion, and resolidification. As it is understood from the process, thermoplastic materials are needed for this production method. The illustration of the FDM system is briefly presented in Figure 2.1.

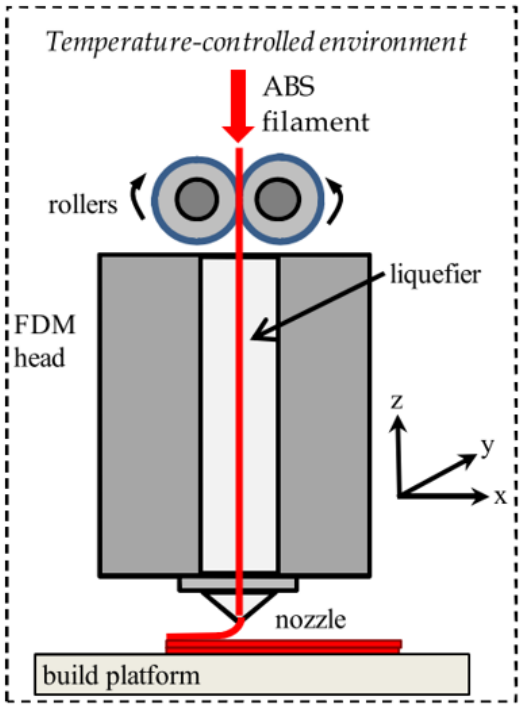

Figure 2.1 : Illustration of FDM 3D printing.

The filament material is extruded through the nozzle in a liquefied phase to form a model, previously designed on CAD software, by the means of an electric motor and heat. The feed rate of the extruder is maintained by controlling a feeding motor extrusion by a controller. The feeding rate and motor torque can be changeable according to an inner pressure change in FDM nozzle and layer thickness [76, 77]. The build material is heated to above its melting point (Table 2.1), and it is expected to solidify less than 0.1s after the extrusion process, thus extruded material is combined with the previous layer by a weld. The nozzle is mounted on a gantry-robot which moves in X and Y directions. The table where the physical part is built on is perforated for Zortrax to avoid detachment of the part, moves only in the Z direction. Furthermore, glass or aluminium flat plates are also used for different FDM printers.

The table goes down according to layer thickness when one of the layers is completely extruded, and nozzle takes its position for the next layer. Four electric motors are used for this operation; three for X, Y and Z directions and one for extrusion [9, 74, 76]. For building complex shaped physical parts, FDM system uses support materials which supports the overhanging parts during the production process, and it provides integrity. After removing the main part from the build platform, these support structures are cleaned by breaking them or by using some special solvents like Acetone [73]. Moreover, supporting structures are laid down layer by layer to build flat support which is called the printing bed, and the main part is built on it [8]. Supporting materials can be designed and produced horizontally or vertically for minimizing the material usage and build time [78].

In the last decades, the size of common consumer-grade 3D printers have decreased, and they substituted with the cubic desktop printers which generally have the range of 50 cm edge lengths and a mass of about 10 kg. The decreased size of 3D printers enables the usage of them in nearly everywhere, but they must be placed away from the user because of harmful fumes that rise from the melting of the filament [79]. Thermoplastic materials in the form of filament are used in most of FDM machines, especially Acrylonitrile Butadiene Styrene (ABS) and Polylactide (PLA) thermoplastics are often used in the 3D printing process [73]. The melting and FDM printing temperature of ABS and PLA is given in Table 2.1 to show the melting and FDM temperature differences. ABS is known as an unpleasant material which causes a headache or health problems if it is inhaled.

Table 2.1 : Melting temperature and FDM temperatures of ABS and PLA.

Material Type	Metling Temperature (^{o}C)	FDM Temperature (^{o}C)
ABS	105	230
PLA	65	180

2.2 Printing Errors in FDM

When a physical part is printed, in some cases the material flow can be interrupted due to some special issues therefore minor and major defects can occur. Minor defects may not be considered if the previous and/or latter layers compensate missing or defected layer. On the contrary, if major defects occur, 3D printed part cannot fulfil the desired

production, and even if it can be rejected. Furthermore, the 3D printing process must be understood clearly, and some measures must be taken to avoid these kinds of defects. Otherwise, misprint causes loss of material, time and fund [79]. The printing defects can be grouped according to [68, 80] as listed:

- Misalignment of the print platform
- Misalignment of the nozzle
- Depletion of printing material or disrupted material flow
- Lack or loss of adhesion to the print platform
- Vibration or shock (from the printer or another source)
- Inaccurate adjustments of printer settings

2.2.1 Misalignment of the print platform

Misalignment of the print platform can cause severe problems, even the print platform or nozzle can be deformed if the 3D printer is not calibrated or tuned well. The print platform moves only in Z-direction, and the movement of the print platform determines the layer thickness. In some cases, if the length of steps cannot be tuned well, the next layer cannot adhere to the previous layer as seen in Figure 2.2 or extruded materials can bow out.

Figure 2.2 : Adhesion problem of layers.

Additionally, misalignment of the print platform can cause different problems such as print does not stick to print platform, the nozzle is too close to print platform, nozzle

penetration or deformation of print platform, print bows out at the bottom which is so-called elephant's foot, print edges are bent (warping syndrome), and fine detail is not captured. Consequently, the threaded rods or lead screws which are used for levelling up or down the building plate and movement of the nozzle in X and Y direction must be checked if there is bending or some printing debris which obstructs the movement of the print-bed. Thus, wiping off the rods to remove leftover debris before applying a fresh coat of lubricant is important.

2.2.2 Misalignment of the nozzle

The nozzle can be moved with the help of gantry-robot which includes two stepper motor, belts, and pulleys. Some problems which affect the working of motors, belts and pulleys also affect the nozzle position, and as a result, a physical model cannot be obtained as it is modelled with the CAD software, as seen from Figure 2.3. There are some main issues with these parts of printers such as tightness of the belts, loose grub screws and printing debris which hinders the steady movement of the nozzle.

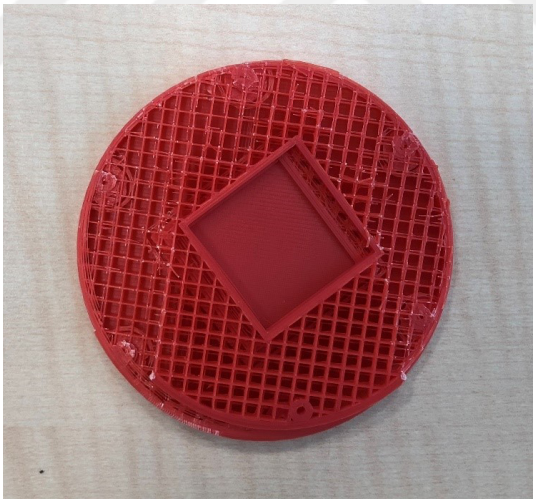

Figure 2.3 : Shifted layers.

The situations mentioned above can cause following problems; print head misses the bed, layers do not line up well, some layers are missing, printed parts slant and print offsets in some places (shifted layers). To prevent these problems, some measures must be taken such as tightening the grub screws on the pulleys on the X and Y-axis motors, checking the rods whether they are straight or not by rolling on a flat surface. It is also important to clean print debris, wiping rods and lubrication of needed parts. Moreover, end switch/stop problems can cause missing the print platform problems. If the nozzle

rests one of the edges without moving that means the end switch does not work on the X or Y-axis.

2.2.3 Depletion of printing material or disrupted material flow

Before starting to print out the physical model, the spool must be checked if there is enough material on the spool. Otherwise, lack of material can ruin the model with the stopping of extrusion in mid-print, and re-printing can be needed in this case, as seen from Figure 2.4. However, out of filament is not the only issue, in some cases, different problems may occur. Blocked nozzle, snapped filament, tangled filament, low diameter filament and stripped filament are also common problems. To prevent filament-based problems, high-quality filaments must be used, and spool must be checked.

Figure 2.4 : Uncompleted part caused by lack of filmanet.

One of the frequent and important problem is the blocked nozzle which prevents the melted filament flow. The blocked nozzle can be cleaned with different methods; heating the nozzle to moderate temperatures and cleaning with a lower diameter needle comparing to the nozzle diameter is the most common methods. However, safety is important in this case due to the high temperature of the nozzle. Besides, some other methods can be used such as heating nozzle to the high temperatures in an oven to convert filament leftover in the nozzle into a carbonized material, trying to push the filament through with another piece of a filament and keeping the nozzle in a solvent such as Acetone can be the way to clean.

2.2.4 Lack or loss of adhesion to the print platform

In some cases, the print does not bond to the print platform, and because of this situation, the warping syndrome can occur until ruining of the physical model. There are several reasons for this problem which can be listed as an unlevel platform, lack of calibration, low heated platform, low heated filament and dirty platform. This problem can be solved by using these methods: adding texture to the platform, tuning print platform distance, cleaning the platform applying agents, and usage of supports and printing bed. Zortrax is using perforated print platforms to prevent this situation, and it is a good solution. For other type print platforms (flat platforms), a thin layer of water-soluble glue can be used by applying to the platform, and this glue can be washed away after printing with hot water. Also, decorator tape is one of the solutions for PLA filament using prints. As it is mentioned before, the nozzle distance from the platform is also important for the adhesion of the first layer that must be tuned well.

2.2.5 Vibration and shock

One of the critical variables that affect print quality is vibration. The reason for vibration or shock is the moving parts of 3D printers, especially acceleration and jerk of gantry robot. Shock or vibrations can cause visual waves on the print surface. To prevent this phenomenon, firstly, the 3D printer must be located on a sturdy and flat surface or table to support the machine. The reason for the vibrations can also arise due to poor maintenance and worn linear bearings. Thus, all the bolts, grub screws, bits and pulleys must be tight enough. Also, the rails must be free of dirt, dust and fluff, and rods must be well lubricated for easy movement of the gantry robot. If all the mechanical measures have been taken, but still there are visual waves on the print due to vibration, the print speed can be reduced. This problem is not very effective for Bowden type extruder using printers because Bowden type extruders are much lighter compared to direct type extruders. In the Bowden type, an extruder is located at the behind of the printer or somewhere which is close to the spool, and this extruder is fixed, it is not moving as direct type. So it reduces the weight of the moving part and also inertia.

2.2.6 Inaccurate adjustments of printer settings

Printer settings enable to control many variables such as layer thickness, support angle, extrusion temperature, platform temperature, print speed, extruder flow ratio, nozzle distance, infill type, infill density, surface layers, supports, seam type and fan speed. They are all very important parameters for print quality to be considered. The most common problem relevant to printer setting is stringing problem which can be prevented by cleaning nozzle and increasing the fan speed. If it still happens after taking these precautions, tuning the melting temperature of the filament can be the solution. Besides, the size of holes may be too small comparing to indented because of contradiction, in this case increasing the hole diameters for about 0.3 mm than the desired one can prevent these problems. Hanging strands is also printer setting problem which can prevent by increasing the support angle, fan speed, and decreasing layer thickness.

2.3 Mechanical Properties of FDM Printed ABS Parts

NX 12: Siemens PLM Software was used to create the solid model of the tensile specimens according to EN ISO 527-2-2012, then the solid model was converted into stereolithography (STL) file and imported into the 3D printer through the Z-Suite software. The thickness of the layer was selected as 0.09, 0.14, 0.19, 0.29 and 0.39 mm with maximum infill, normal seam and no material support used. The tensile specimen structures were produced horizontally, and they can be seen in Figure 2.5. In this way, it was possible to decrease the effect of vibration and shocks, which is very problematic when they create echoes or waves on the produced physical model. Echoes and waves on the extruded models can have an adverse effect on its mechanical properties. Besides, every variable belongs to the filament, 3D printing device and 3D printing device slicing software affects the mechanical properties of the produced physical model.

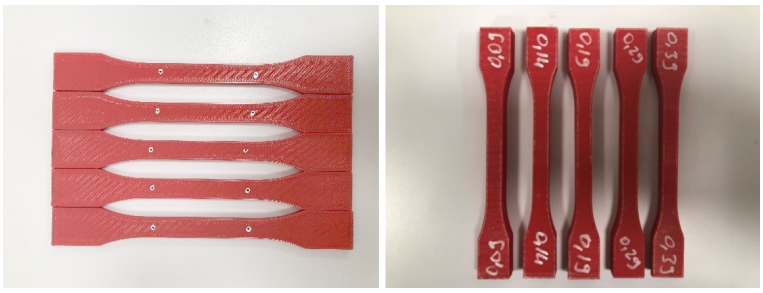

Figure 2.5 : FDM printed ABS tensile specimens.

There are studies in the literature which enlighten the mechanical effect of printing variables and material specifications. Such as the colour of filament has no considerable effect on the tensile strength [81, 82]. Montero et al. [82] showed that the colour of filament affects the tensile strength value almost 3%. Tymrak et al. [83] studied the effect of layer thickness on the tensile strength. Three different layer thickness was used in the study which are 0.4, 0.3 and 0.2 mm, and as a result, the average tensile strengths of 28.2, 27.6, 29.7 in MPa were obtained respectively. Dawoud et al. [84] presented that the density of produced part which increased from 0.94 g/cm^3 to 1.03 g/cm^3, the tensile strength (MPa) increases 28 to 33. Zou et al. [85] showed that the change in the raster orientation could change the tensile strength maximum of 6%. For determining the mechanical properties of produced parts, tests were conducted with using the Instron Universal Testing machine model 5890 100kN. To determine the mechanical specifications of used ABS for understanding its mechanical behaviour and establishing a ground for further numerical studies, five tensile tests were performed for each layer thickness according to EN ISO 527-2-2012 under a rate of 2 mm/min. Video extensometer was used for obtaining strain data of the tensile specimens. As a result, the stress-strain diagram was obtained and presented in Figure 2.6.

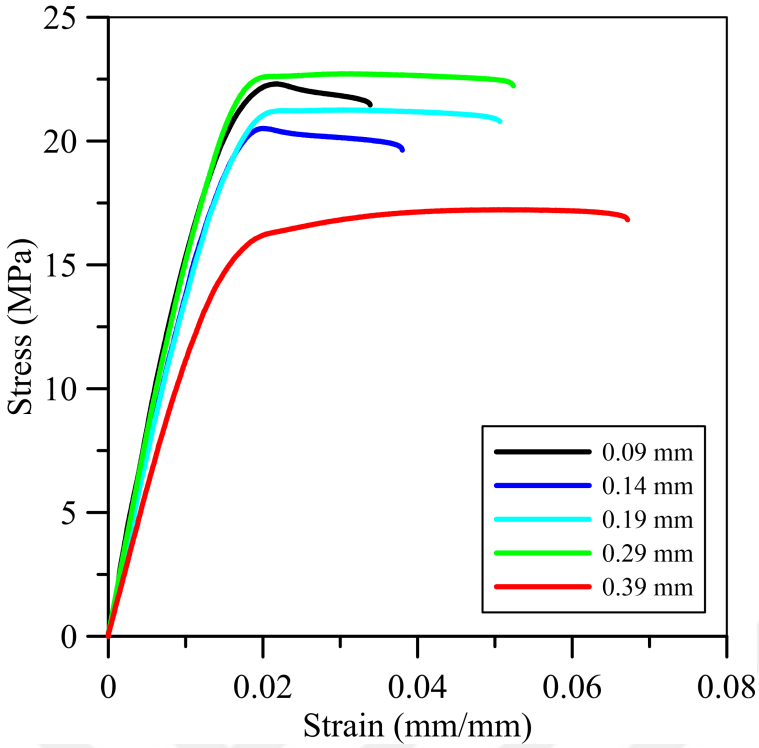

Figure 2.6 : Stress-strain diagram for all layer thicknesses.

As seen in Figure 2.6, the increase in the layer thickness does not directly change the tensile stress in the same manner. 0.29 mm layer thickness experiences the maximum tensile stress comparing to other layer thicknesses. The thickest layer thickness which is 0.39 mm shows the minimum tensile stress. It can be directly seen from Table 2.2 that the density of the produced materials in other words voids in the specimens directly determines the amount of tensile stress. For the specific stress and specific modulus, tensile stress to density and Young modulus to density ratio, similar results can be seen, but 0.09 mm layer thickness tensile specimens show the highest specific modulus and considerable specific stress.

Table 2.2 : The effect of the layer thickness to the tensile stress, specific stress, Young modulus and specific modulus.

Layer Thickness (mm)	Density (kg/m^3)	Young Modulus (GPa)	Tensile Stress (MPa)	Specific Modulus (kNm/kg)	Specific Stress (kNm/kg)
0.09	845±6	1.59±0.22	21.38±0.85	1.89	2.53
0.14	833±6	1.36±0.15	20.51±0.46	1.64	2.46
0.19	821±6	1.35±0.07	21.16±0.73	1.65	2.58
0.29	863±2	1.42±0.07	22.59±0.36	1.64	2.62
0.39	804±4	1.16±0.07	16.06±0.36	1.45	2.00

However, considering Young modulus for different layer thickness the same pattern for the tensile stress was not achieved. The highest Young modulus can be observed for 0.14 mm layer thickness. For the specific Young modulus, Young modulus to density ratio, similar results with slight differences can be seen and 0.09 mm thickness presents the highest result.

2.4 Overview and Discussion

Several factors affect the print quality considering the FDM printing method. Some of them can be understood and obtained by experiences. However, there is no universal methods that can be applied to all FDM procedures due to the differences with commercial FDM machines considering its structure, usage and slicing software. Nevertheless, for avoiding bad prints, some measures must be taken. Especially the room where FDM machines are located must be lack of draughts, and the table or surface where the printer is stood must be sturdy and flat. Besides, to prevent low-quality prints, high-quality filaments must be used and 3D printing flaws, slicing software options and FDM machine working principles must be understood clearly to take precautions.

The effect of layer thickness was examined in this chapter to determine the relationship between layer thickness and mechanical properties to select the best layer thickness

for an FDM 3D print. Zortrax slicing software enables to the use of five different layer thicknesses which were studied in this chapter. Although the layer thickness of 0.29 mm was the best for obtaining the maximum amount of tensile stress, 0.09 mm layer thickness experienced the best specific tensile stress and Young modulus.

3. CRUSH BEHAVIOUR OF FDM PRINTED POLYMERIC AUXETIC LATTICES

3.1 Introduction

In this chapter, quasi-static crush response of anti-tetrachiral [18] and re-entrant hexagonal [17] lattices which exhibit in-plane negative Poisson's ratio were experimentally investigated. Re-entrant lattices have been used as comparing geometry against anti-tetrachiral lattices. However, re-entrant auxetic lattices showed low crush performance due to some weak parts in the unit cell connections and some modifications were needed to improve its energy absorption characteristic. After modification, modified re-entrant auxetic lattices were reproduced, crushed and compared with regular re-entrant lattices. Afterwards, the crush behaviour of anti-tetrachiral and modified re-entrant hexagonal lattices were compared experimentally and numerically to define better energy absorbing deformation mechanism. Moreover, a benchmark study was conducted to find effective chiral topology to use in applications. In summary, this work is devoted to giving an insight into the in-plane compressive response of these 3D printed lattices in the plastic region and finding efficient topology. For this purpose, lattice structures have been manufactured via fused deposition modelling technique and tested in quasi-static condition. In addition, models were simulated by Finite Element Analysis (FEA) using commercial software, ABAQUS. The deformation mechanism of lattice structures was observed and modelled in order to understand the relationship between failure, deformation modes, and force response.

3.2 Lattice Geometries

2D auxetic lattice geometries can be grouped as re-entrant, rotating rigid and chiral as seen in Figure 3.1, which are all have different mechanism for auxeticity [86]. Considering crush behaviour, rotating rigid geometries are not suitable due to their bulky parts. For comparison, anti-tetrachiral and re-entrant lattices exhibiting NPR

in-plane direction and in the elastic phase were crushed at the quasi-static condition to observe their elastic and plastic deformation. Firstly, formulation on the strength of structures in the y-direction, where auxeticity is experienced, and its relation with other parameters were given in this section.

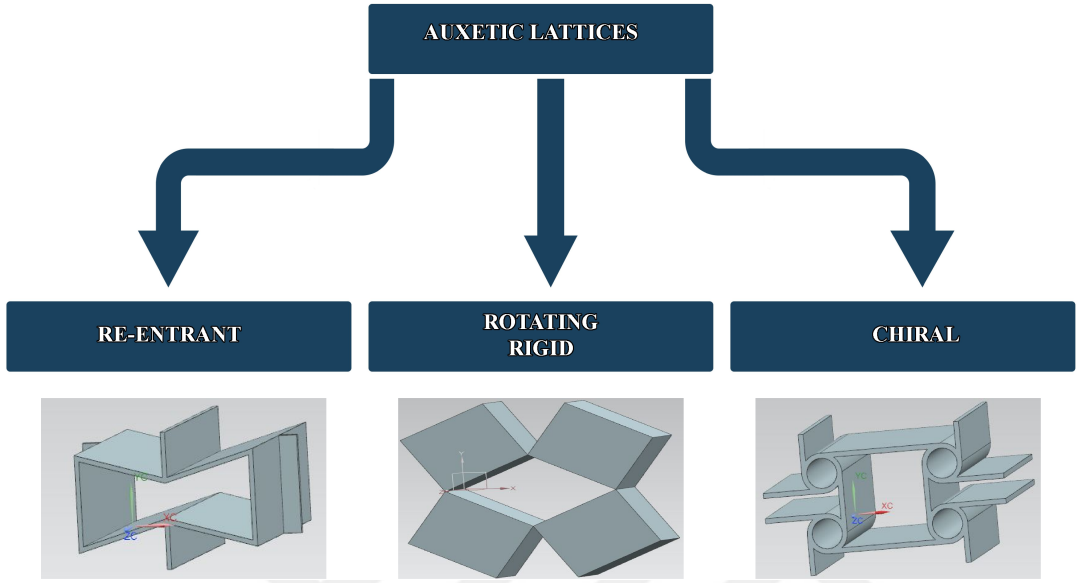

Figure 3.1 : 2D auxetic lattice types.

The chiral auxetic system can be defined by the interconnected systems of nodes and ligaments, each tip of the ligaments is connected to the nodes tangentially. The number of the ligaments connected to one node characterises the chiral honeycombs as hexachiral, tetrachiral and trichiral systems which include 6, 4 and 3 tangential ligaments for each node, respectively. The prefix anti is used to describe the spatial relations between ligaments and nodes; lattice structures with cylindrical nodes on the opposite sides of the ligaments are called chiral systems, and conversely, cylinders on the same side of the ligament are called antichiral systems. However, all the chiral systems do not show auxeticity, 6 and 4 ligaments connected systems and the anti-trichiral systems with short ligament limit only show negative Poisson's ratio [54]. The deformation of chiral systems starts with the rotation of nodes, and flexing and bending of the ligaments as a result of rotation. Then ligaments become half wave-shaped for antichiral systems and full wave-shaped, which is better for energy absorption, for chiral systems [36]. Although anti-tetrachiral and re-entrant auxetic systems have similar outline topology, the deformation mechanisms are quite different. Based on the unit cell deformation mechanism, re-entrant structures have the diagonal ligaments leads to auxetic effect by ligament rotations, and chiral structures maintain

auxeticity by the coupled deformation of node rotation and ligament bending. Basic re-entrant auxetic structure and honeycomb structure have been studied for many years, and comparison studies according to energy absorption for both topologies can be found in the literature. As a result of comparison studies, it can briefly concluded as re-entrant auxetic structures show low initial peak force and better mean crushing load to initial peak load ratio beside better energy absorption [62, 87].

3.2.1 Anti-tetrachiral

The anti-tetrachiral lattice is composed of four edge ligaments, and compressive deformation likely develops through bending moments around these ligaments. Chen et al. [18] presented elasticity equations for anti-tetrachiral lattices parameters that are presented in Figure 3.2. The results provide a better understanding of the relation between modulus parameters (E_x, E_y and G_{xy}), geometrical parameters (α_x(=L_x/r), α_y (=L_y/r)), and Poisson's ratio. By this means, these elastic relations benefit to design stiffer unit lattice. Young's modulus of anti-tetrachiral lattice honeycombs was defined as in Equations 3.1 and 3.2 [18] as follows:

$$E_x = \frac{E_c \beta^3 \alpha_x}{12(1-\frac{\beta}{2})^2}\left(\frac{1}{\alpha_x - 2\sqrt{2\beta-\beta^2}} + \frac{1}{\alpha_y - 2\sqrt{2\beta-\beta^2}}\right) \tag{3.1}$$

$$E_y = \frac{E_c \beta^3 \alpha_y}{12(1-\frac{\beta}{2})^2}\left(\frac{1}{\alpha_x - 2\sqrt{2\beta-\beta^2}} + \frac{1}{\alpha_y - 2\sqrt{2\beta-\beta^2}}\right) \tag{3.2}$$

where α_x, α_x and β equals to L_x/r, L_y/r and t/r respectively.

Dimensions of the manufactured sample were listed in Table 3.1. These dimensions have been selected due to the manufacturing constraints of the ZOTRAX 3D printer. Smaller L_x, L_y parameters were selected due to global buckling risk under static crushing conditions. When Equation 3.2 is revisited, it is concluded that scaling the unit lattices down to half of its original, α_x, α_y and β stay the same as the original, and relative volume increases proportionally to the relative density.

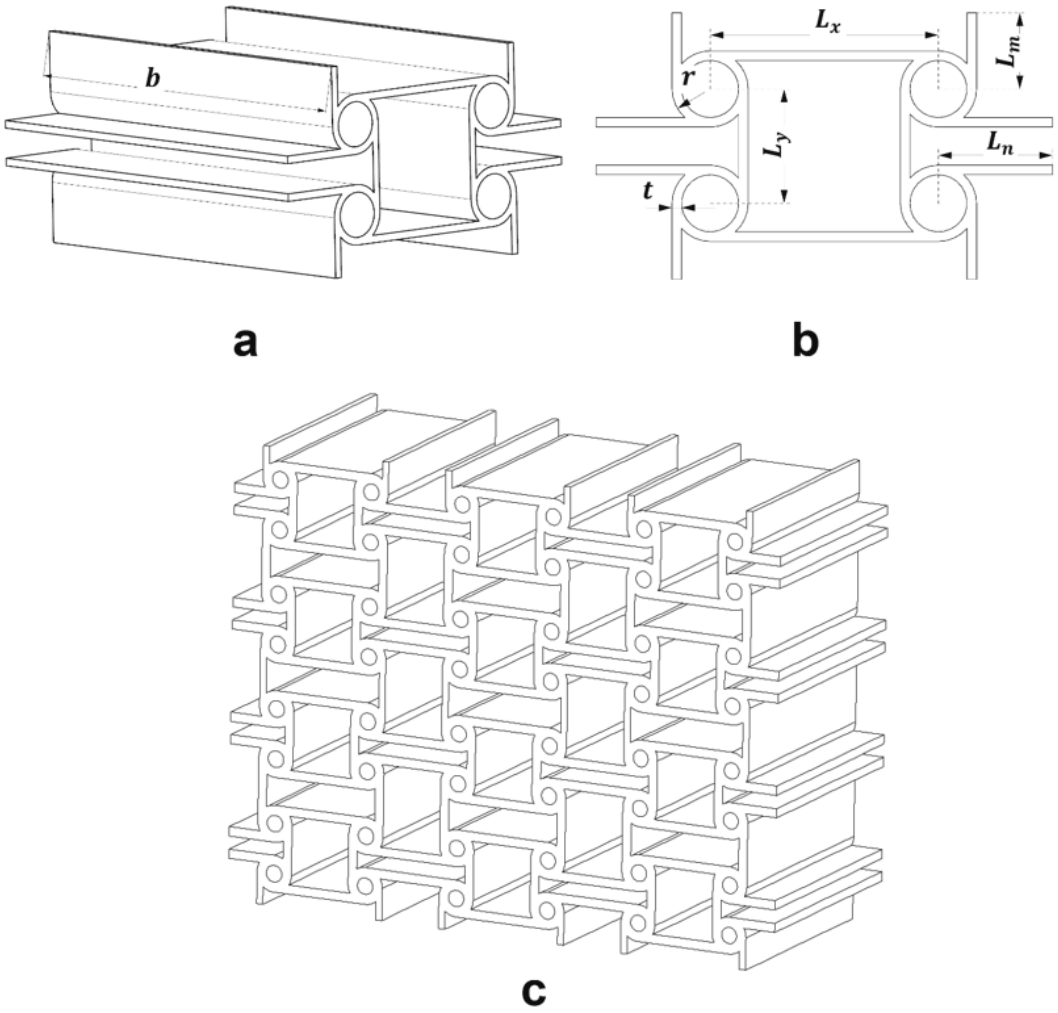

Figure 3.2 : Anti-tetrachiral unit cell a) iso-view b) front-view c) manufactured sample.

Table 3.1 : Geometrical parameters of the manufactured anti-tetrachiral samples (all in mm).

	L_x	L_y	r	t	b	L_m	L_n
Planned	12	6	2	1	28	4	6
Produced	12	6.55	2.4	1.25±0.25	28	4.5	6.5

In addition to E_x and E_y formulations, when the relative density of honeycomb structure has been increased, lattice system becomes stiffer in the z-direction (out of plane) since these cellular topologies are thought to have a uniform wall thickness and depth [50]. The relation between E_z and E_c, the elastic modulus of constituent material, are defined by the density of the lattice system which is given in Equation 3.3:

$$\frac{E_z}{E_c} = \frac{\rho}{\rho_c} \tag{3.3}$$

in which ρ_c and ρ denote core material and lattice structure densities, respectively. Another representation with a relation between core material area (A_c) and unit cell area (A_u) relevant to the density of the cell-based core structures is obtained as:

$$\frac{\rho}{\rho_c} = \frac{A_c}{A_u} = \frac{A_n + A_l - A_j}{A_u} \tag{3.4}$$

where A_n, A_l and A_j are nodes, ligaments and junction areas of each unit lattice [55]. The increased surface area does not change E_x and E_y if α_x, α_y and β are constant [18]. Therefore, scaling down of a unit lattice system with constant α_x and α_y do not change E_x and E_y, but increases relative density. While the relation between energy absorption and relative density at dynamic crushing regimes depends on the unit cell geometry, in the quasi-static regime, increased relative density benefits the energy absorption [87, 88]. According to the formulations in Equation 3.1 and Equation 3.2, geometries can be tuned to obtain higher E_x and E_y values. However, E_y increases when α_y is increased and α_x is decreased or E_x increases when α_x is increased and α_y is decreased. Due to this inverse relationship, higher E_y is required for higher stiffness in the y-direction loading. Consequently, L_m and L_n are selected as equal to 2, and α_x and α_y are defined as 3 and 6, respectively to obtain higher E_y.

3.2.2 Re-entrant

Re-entrant is another example of auxetic lattice geometries, Huang et al. [17] proposed the re-entrant hexagonal geometry for in-plane auxetic behaviour and high bending stiffness in the out of the plane. Unit cell parameters and dimensions have been presented in Figure 3.3 and Table 3.2.

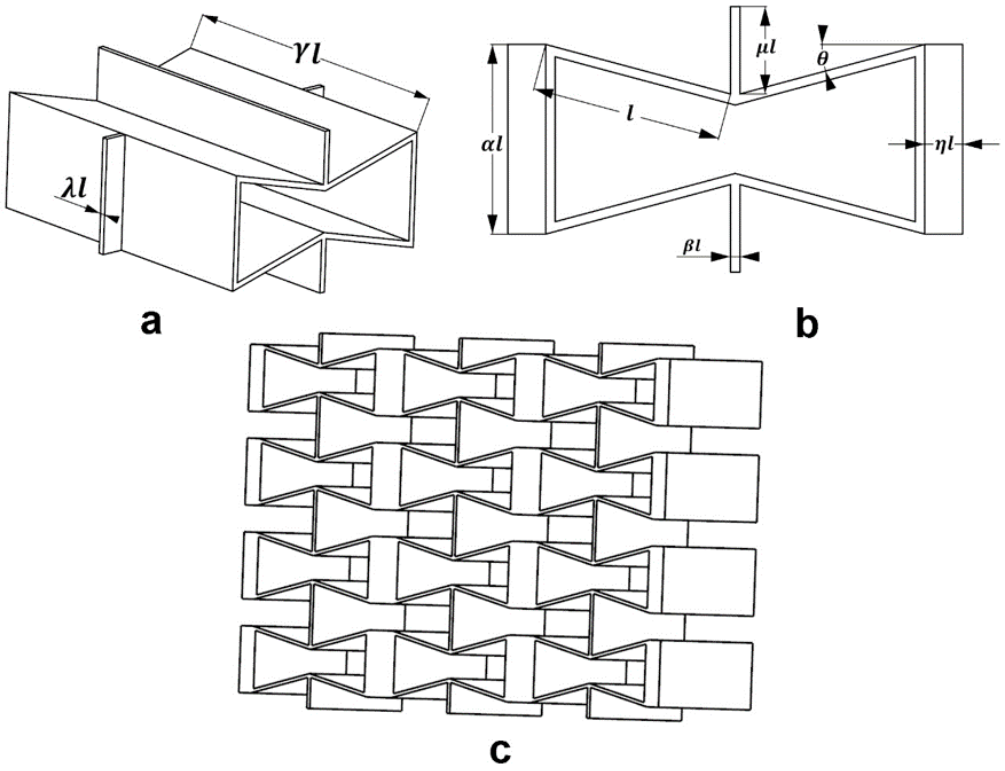

Figure 3.3 : Re-entrant hexagonal unit cell a) iso-view b) front-view c) manufactured sample.

Table 3.2 : Geometrical parameters of the manufactured modified re-entrant samples.

l	α	β	μ	λ	γ	η	θ	ν
10 mm	1	0.1	0.46±0.04	2.8	2.8±0.05	0.1	15^{o}	-0.6

However, re-entrant hexagonal geometry proposed by Huang et al. [17] was used for in-plane compression tests. It was observed that the connections between each unit cells were broken down prematurely. The results regarding thin joint walls were also presented in this work [89]. Therefore, the sidewalls of the modified re-entrant lattices were thickened with the equality of the λl=ηl. This geometry was taken into account to compare with anti-tetrachiral lattices. It was reported that the change in the parameters of the re-entrant lattices exhibited high out-of-plane strength [17]. Moreover, the compressive deformation was investigated in the in-plane direction where auxetic behaviour is present. Both the limit of auxeticity and subsequent plastic buckling phase can be observed. The elastic moduli in two directions were defined in Equation 3.5 and Equation 3.6 as:

$$\frac{E_x}{E_s} = \frac{\alpha\gamma\beta^3(\eta + \cos\theta + \frac{\beta}{2})}{\frac{1}{2}\alpha + \mu - \sin\theta[\alpha\lambda(\sin^2\theta + \beta^2\cos^2\theta) + 2\eta\nu\beta^3]} \tag{3.5}$$

$$\frac{E_y}{E_s} = \frac{\beta^3(\frac{\alpha}{2} + \mu - \sin\theta)}{(\eta + \cos\theta + \frac{\beta}{2})(2\mu\beta^2 + \beta^2 + \cos^2\theta - \beta^2\cos^2\theta)} \tag{3.6}$$

where α, β, η, λ, μ, and ν denotes geometrical non-dimensional parameters of the re-entrant hexagonal lattice depicted in Figure 3.3. The internal cell angle is represented by θ. The length of the inclined walls is represented by l. It is shown that wall thickness and top-bottom struts affect the stiffness. However, compression response is sensitive to global buckling (slenderness) and local bucklings that are the results of non-dimensional parameters.

3.3 Experimental Setup

Two different auxetic geometries were manufactured using FDM technique on Zortrax M200 3D printer with acrylonitrile butadiene styrene (ABS) polymer build material. Elastic material properties of the ABS are provided by the supplier; Young's modulus, Poisson's ratio, and density were given as 1850 MPa, 0.35 and 1040 kg/m^3, respectively [90]. However, provided material specifications are different from the manufactured ones due to FDM manufacturing method characteristics. In FDM, a nozzle deposits melted polymer layer by layer, and the formation of inner gaps cannot be prevented. In addition, different infill patterns and strategies are employed in FDM for thick parts to prevent the wrapping of manufactured parts. Thus, thinner tensile specimens can be selected to reduce the magnitude of inner gaps and to obtain solid infill approaching constituent material specifications. EN ISO 527-2:2012 standard was used to obtain tensile test results. All the tensile specimens were printed at 90^o raster orientation which is parallel to building plate, and test set-up is shown in Figure 3.4.

Figure 3.4 : Tensile test setup using the method of advanced video extensometer.

Tensile tests were carried out using an INSTRON 5980 100 kN Universal Testing System with AVE 2 non-contacting video extensometer and its own commercial DIC software. Tensile results are illustrated in Figure 3.5 and measured mechanical and physical material properties were listed in Table 3.3.

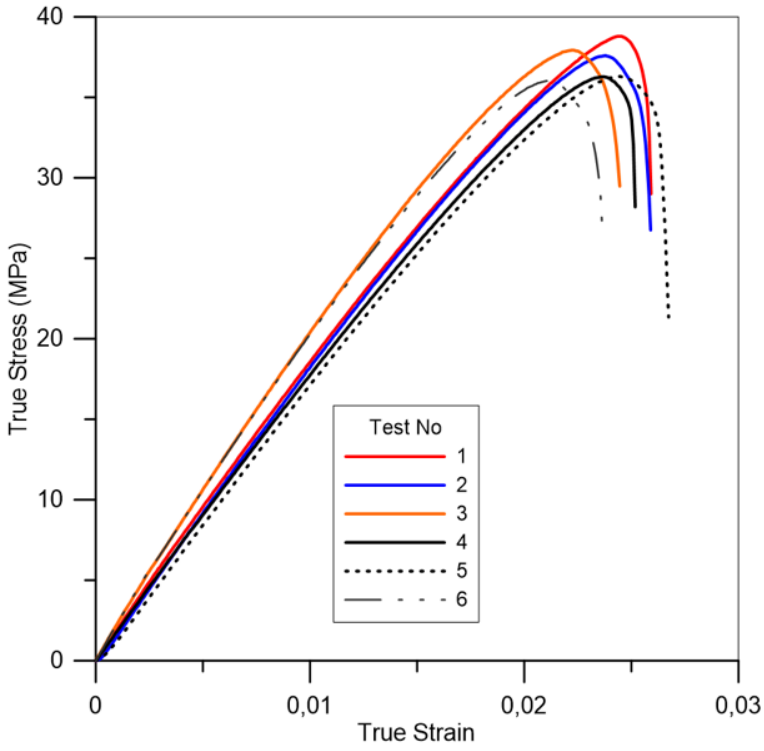

Figure 3.5 : Tensile test results of the ABS material.

Table 3.3 : Material properties of the 3D printing specimens.

Young's Modulus (GPa)	Tensile Stress (MPa)	Strain at Break (%)	Density (kg/m^3)
1.99±0.22	26.75±4.00	2.53±0.15	845±6.00

The 3D printer resolution for the production was selected as 0.09 mm for both geometries, and infill was chosen as maximum to avoid empty spaces. Manufactured samples were illustrated in Figure 3.6. The quasi-static in-plane crushing tests were conducted using INSTRON 5980 100 kN Universal Testing System with a crushing velocity of 10 mm/min. Load change and the displacement of the crosshead values were recorded. The wall thickness dimensions for lattice structures were selected as 1 mm to manufacture solid infilled lattice structures. All test sample dimensions were listed in Table 3.1 and Table 3.2. Both designs were manufactured, considering their topology parameter limitations, for trying to capture similar box-volume, as well as mass (Figure 3.6).

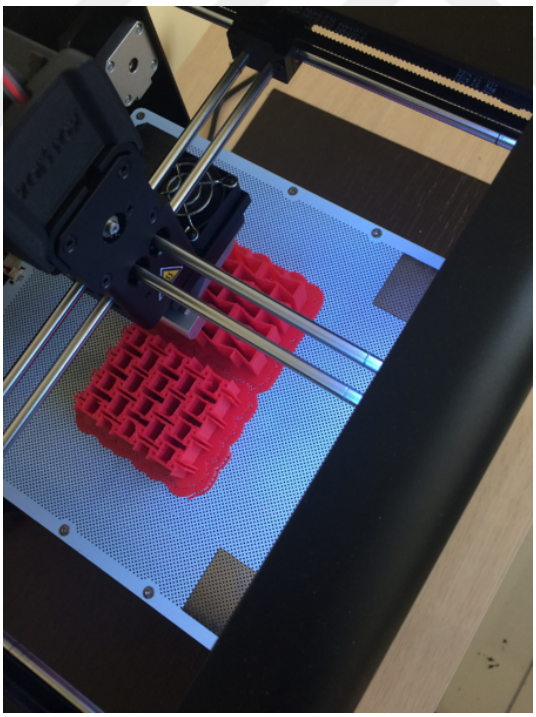

Figure 3.6 : Production of anti-tetrachiral and re-entrant hexagonal samples.

3.4 Numerical Analyses

Finite element analyses are conducted using the explicit solver of ABAQUS software. Quasi-static crushing state based on experimental conditions has been created using

mass scaling method in the solver to decrease the computational costs. Kinetic energy should not overpass 10% of internal energy to obtain the correct result while using the mass scale [91]. Numerical models of manufactured lattices are represented in Figure 3.7 and 3.8. Linear elastic material model and classical material plasticity material model are used in the analyes which are explained in Chapter 5.

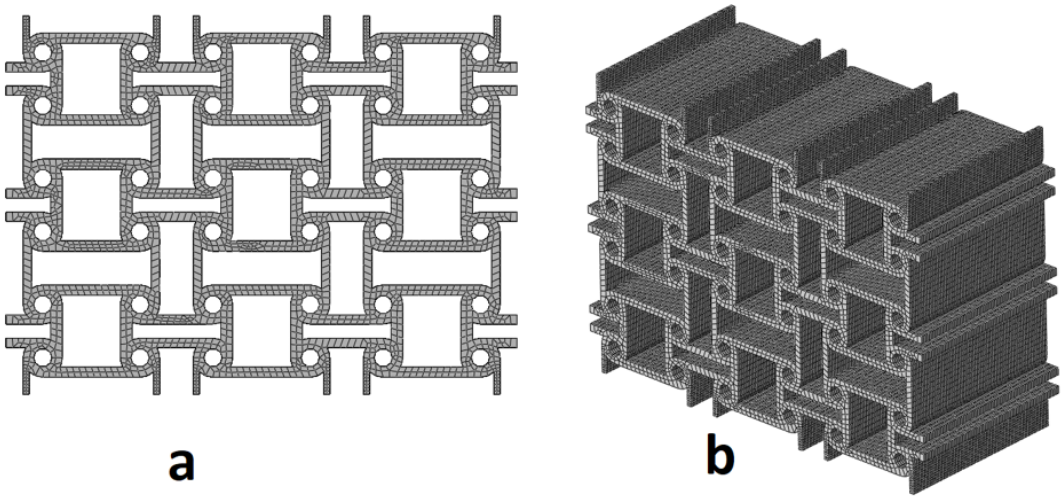

Figure 3.7 : Anti-tetrachiral lattice system a) front-view b) perspective-view.

Out of the complex shape, the automatic mesh was generated by taking into the account of the maximum deviation factor as 0.1 and a minimum fraction of global size as 0.9. As a result, approximately 670000 solid C3D8R elements were created for 0.4 mm unit mesh input. The models consist of the rigid top plate, the auxetic sample with solid elements and rigid plate at below.

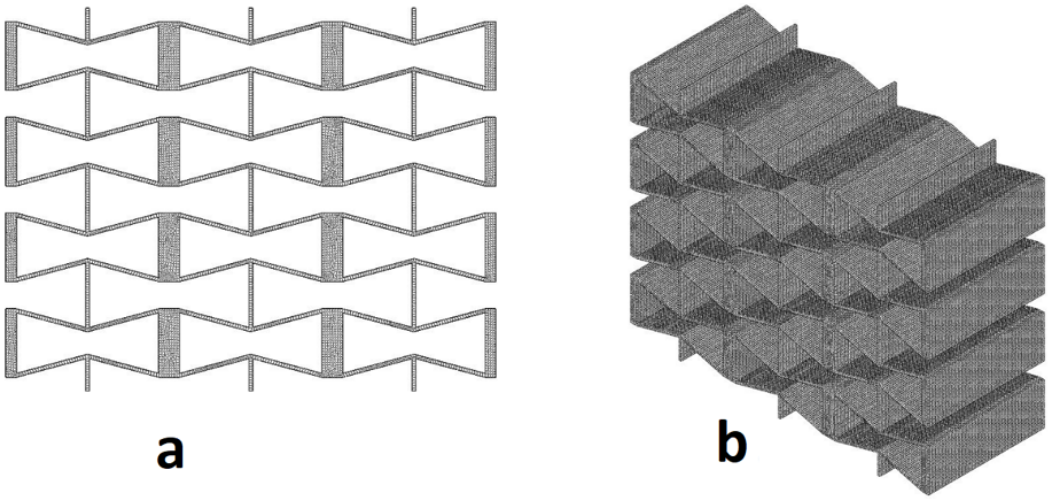

Figure 3.8 : Re-entrant hexagonal lattice system a) front-view b) perspective-view.

The top plate is free only in the axial direction. Force-displacement boundary condition has been applied to simulate experimental condition. The interaction was created as "all with self" definition. Tangential and normal friction coefficients were deployed with a value of 0.2. Load-displacement curves have been produced and compared with experimental findings.

3.5 Crush Theory

The load-deflection diagrams characterize the energy absorption capacity of crashworthy structures and can be divided into three phases which are elastic, plateau, and densification phases. Amongst them, a low amount of the energy can be absorbed by elastic deformation while the larger amount of deformation energy is absorbed by the plastic deformation and fracture. Thus, a longer plateau phase is desired for the better energy absorption of the crashworthy structures. The energy absorption (EA) is calculated from the area under the load-deflection curve as in Figure 3.19. The test curve which was drawn for 240 seconds showed a dramatic increase in the load due to the fact that the densification phase has started. Densification phase is not principally taken into the account for deciding the energy-absorbing capability of the manufactured samples. The calculation for the energy absorption is defined as

$$EA = \int_0^d F d\delta \tag{3.7}$$

where F is reaction force in the crushing process, and d denotes the maximum deflection until the densification phase. Therefore, the onset deflection of the densification phase is needed to be determined to define where the plateau phase ends, and the densification phase starts. In literature, there are several ways to define the onset deflection of densification, such as intersecting the tangents of densification phase and load/stress plateau phase [92–94], picking a last local minimum deflection/strain point before dramatic increase [95, 96], and specifying a point using the same tangent of elastic phase [94], however, an energy efficiency parameter, $\eta(\delta)$, expressed in Equation 3.8,

$$\eta(\delta) = \frac{1}{F(\delta)} \int_0^d F(\delta) d\delta \tag{3.8}$$

is used in this study to determine the onset deflection of densification numerically and consistently [21,97]. By the means of the energy absorption efficiency, a representative onset deflection of densification is defined in which the energy absorption efficiency reaches the highest point on the efficiency-deflection plot, it is expressed in Equation 3.9,

$$\frac{d\eta(\delta)}{d\delta}\bigg|_{\delta=d} = 0 \tag{3.9}$$

The energy absorption capability can be captured via specific energy absorption (*SEA*) as defined in Equation 3.10,

$$SEA = \frac{EA}{m} \tag{3.10}$$

which expresses the amount of dissipated energy divided by structural mass (m). Besides, mean crushing force (MCF) is another efficiency parameter to be considered to observe crashworthiness capacity of the structure which is given below.

$$MCF = \frac{1}{d}\int_0^d F d\delta \tag{3.11}$$

Regarding the occupant safety of a vehicle, mean crushing force is divided by peak crushing force (PCF), which is the highest force in the load-deflection curve, to obtain crushing force efficiency (CFE) that is aimed to be close to 1 [51] as defined in Equation 3.12,

$$CFE = \frac{MCF}{PCF} \tag{3.12}$$

Comparison of energy-deflection, force-deflection and mean crushing force-deflection curves are other efficiency measurement tools. The cellular structures exhibit normally three regimes in the force-deflection response. After the initial elastic region is completed, the plateau regime that is the main energy absorption period for the crushed structure starts and generally continues in the same level of force. Higher force level in the plateau regime makes the structure better energy absorber. A nominal stress-strain curve or mean crushing force-deflection curves are used to compare the

crushing efficiency of different cellular structures. Their plateau regimes are observed to understand the energy absorption capacity in terms of mean crushing force- and/or stress. When the plastic collapse reaches the limit, the densification phase starts, and force increase to an extremely high level. The impact energy should be dissipated before the crushing has arrived at this section.

3.6 Results

3.6.1 Experimental results for anti-tetrachiral and regular re-entrant

All tests were conducted in identical conditions with INSTRON 5980 100 kN Universal Testing System. The deformation velocity for both experiments are 10 mm/min. Figure 3.9 represents the producted anti-tetrachiral and re-entrant lattice cells and Figure 3.10 presents the conducted experiments.

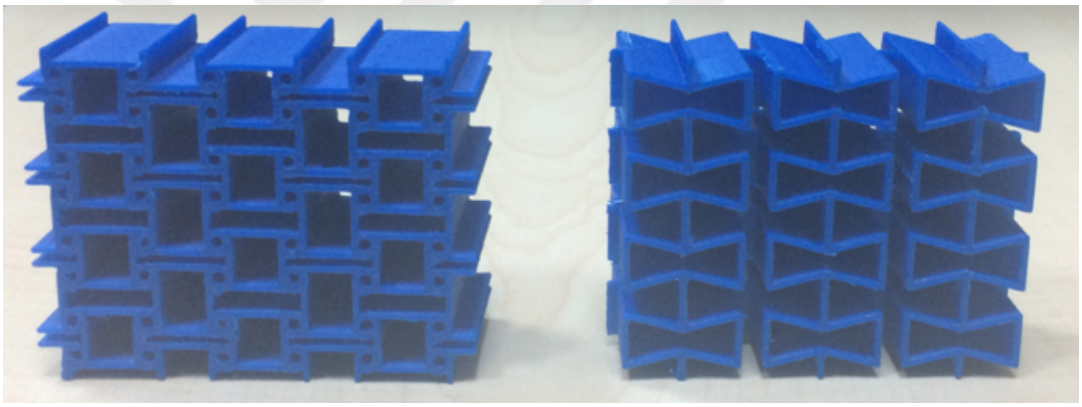

Figure 3.9 : Produced anti-tetrachiral and regular re-entrant lattices.

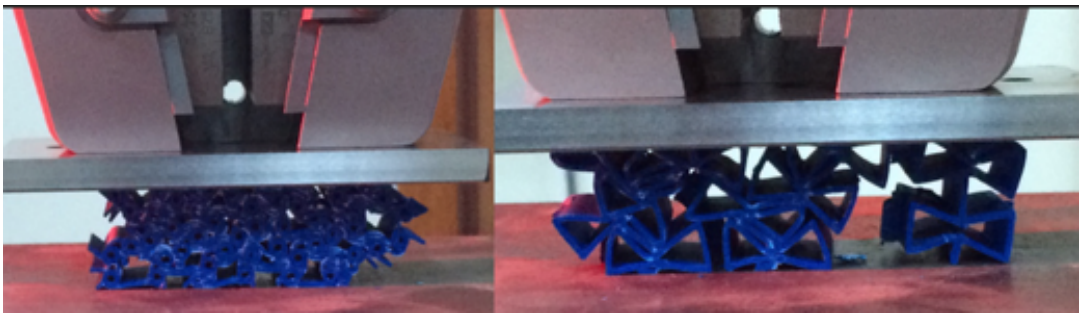

Figure 3.10 : Crushed anti-tetrachiral and regular re-entrant lattices.

As a result, compressive load and deflection graphs have been obtained as in Figure 3.11. There is a huge different comparing the total energy that absorbed. Crushed anti-tetrachiral lattice structure is shown in Figure 3.12. The re-entrant hexagonal

structure was easily deformed and fragmented due to its supports (struts) between unit lattice cells as seen from the deformed shape of re-entrant hexagonal structure in Figure 3.13. There is very thin struts between unit cells to connect them (1x2.8x10 mm). To increase absorbed energy, re-entrant hexagonal was modelled again, and support structures between the unit cell structures extended along through the whole geometry in other words the sidewalls of the modified re-entrant lattices were thickened with the equality of the $\lambda l = \eta l$.

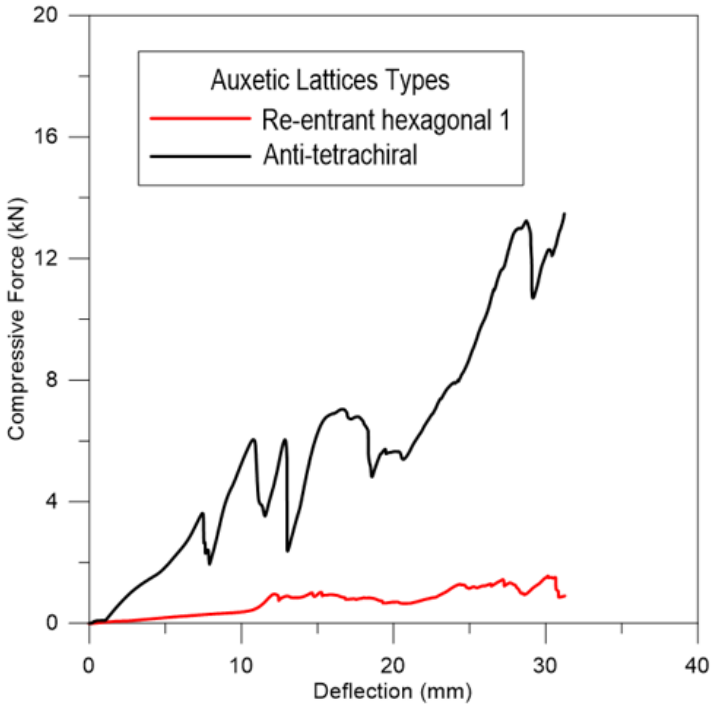

Figure 3.11 : Re-entrant hexagonal 1 and anti-tetrachiral auxetic structures load – deflection graph.

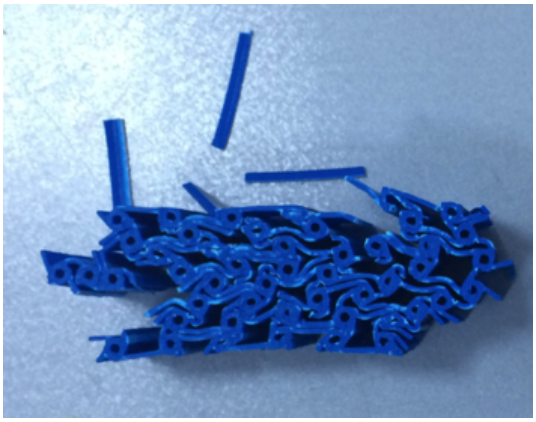

Figure 3.12 : Deformed anti-tetrachiral auxetic lattice structure.

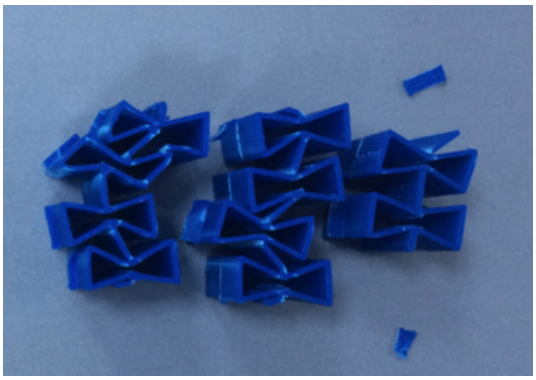

Figure 3.13 : Deformed re-entrant auxetic lattice structure..

As a result of the modification in the re-entrant hexagonal structures, struts starts to carry more load and it can be seen the effect of those struts in the Figure 3.15 and 3.16 where modified re-entrant auxetic lattice is mentioned as re-entrant hexagonal 2. The effect of modification in the topology of re-entrant auxetic lattice on the crush performance of cell is extensively covered in Section 3.6.3.

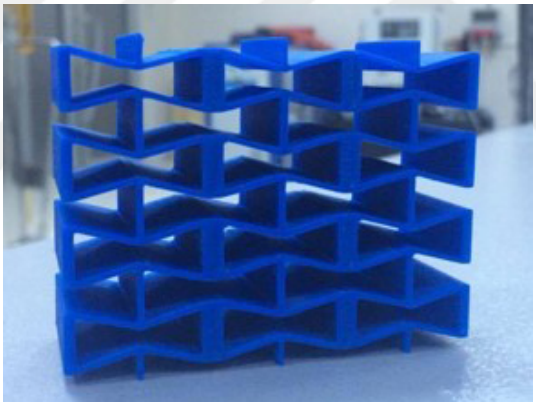

Figure 3.14 : Produced modified re-entrant lattice.

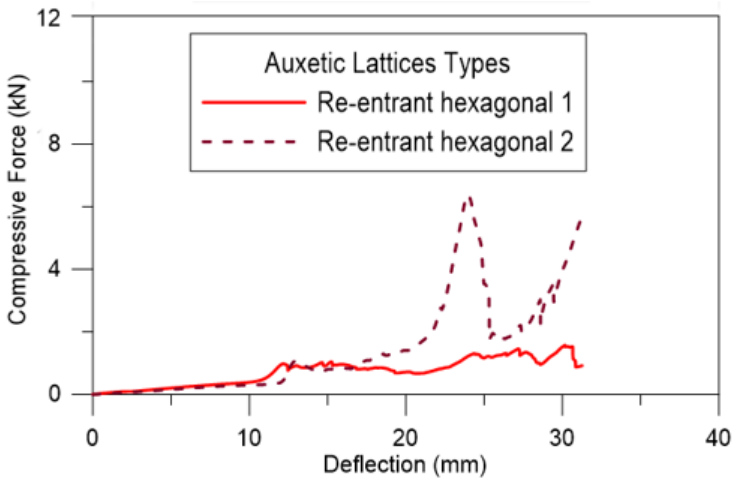

Figure 3.15 : First re-entrant hexagonal and second re-entrant hexagonal auxetic structures load – deflection graph.

Figure 3.16 : Deformed auxetic structure 2 (re-entrant hexagonal 2).

3.6.2 Experimental results for anti-tetrachiral and modified re-entrant

Crushing tests for both anti-tetrachiral and modified re-entrant hexagonal are illustrated in Figure 3.17 and 3.18, respectively. It is noted that Figure 3.15 and Figure 3.18(a) show different load - displacement curves for the same topology. The reason beneath this situation is the usage of same of ABS polymer material in different environmental conditions and duration after package opening of the ABS filament. Sunlight exposure and humidity reduce the mechanical performance of polymers. However, it seems that all tests for anti-tetrachiral and re-entrant lattices show a similar trend in their own experiment group. Figure 3.19 depicts a comparison of anti-tetrachiral and re-entrant curves. Anti-tetrachiral lattices absorb more energy due to their collapse mechanism that depends on ligaments bending and node rotation on the four corners of each lattice. In contrast, from thin-walled metal tubular structures commonly used under axial crushing loading for crashworthiness purpose, MCF curves of current geometries exhibited increasing energy absorption response. That behaviour shows that the topology is feasible to use them as one of the lattice structure for filling of the thin-walled crash absorbers to increase crashworthiness ability. From the calculation of the onset deflection of densification via the energy efficiency parameter, the densification phase of anti-tetrachiral and re-entrant geometries started at 25.32 mm and 26.14 mm deflection, respectively.

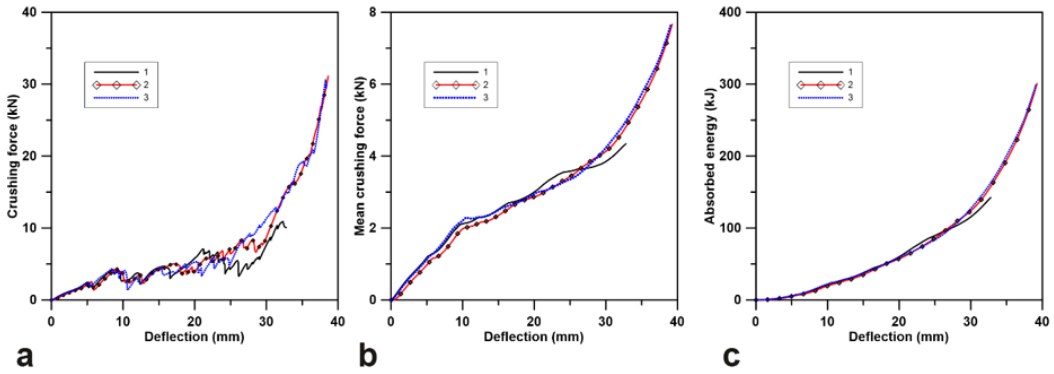

Figure 3.17 : a) Force-deflection b) mean crushing force-deflection c) energy absorption-deflection curves of anti-tetrachiral lattices at 10 mm/min velocity.

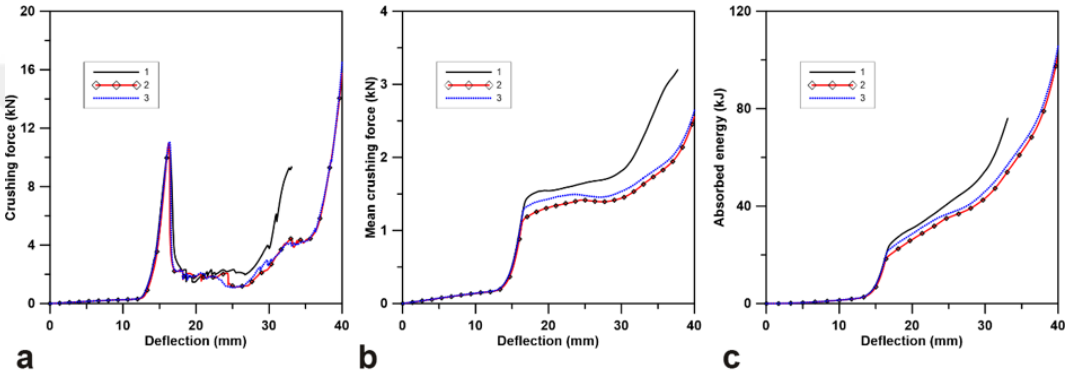

Figure 3.18 : a) Force-deflection b) mean crushing force-deflection c) energy absorption-deflection curves of re-entrant hexagonal lattices at 10 mm/min velocity.

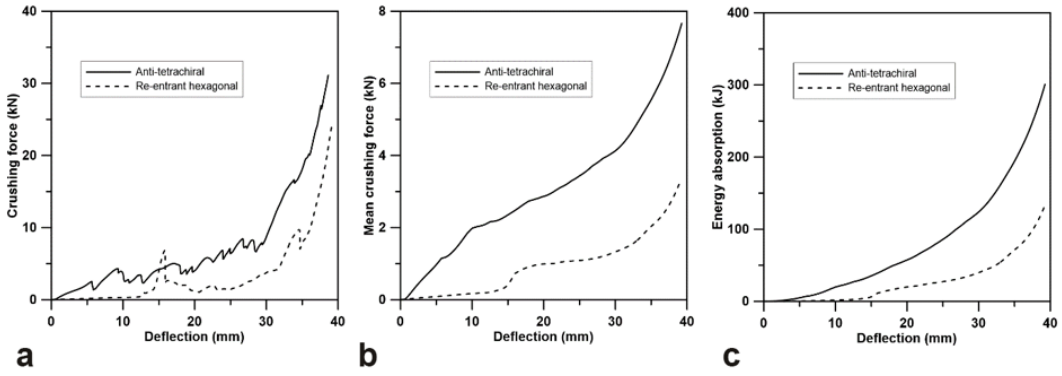

Figure 3.19 : a) Force-deflection b) mean crushing force-deflection c) energy absorption-deflection curve comparison between anti-tetrachiral and re-entrant hexagonal structure at 10 mm/min velocity.

3.6.3 Deformation modes for anti-tetrachiral and modified re-entrant lattices.

After the elastic deformation phase was completed, plastic collapses and local bucklings on the struts are observed for each design. The collapse occurs via bending

around the ligament (edge circles) of the anti-tetrachiral lattices. However, the existence of these ligaments provides higher bending stiffness against the expected collapse. For instance, when the bending moment around the ligaments reached a high level, the vertical struts of the top lattices could not withstand the compressive load and failed after 5 mm deflection. Moreover, these broken struts contacting with the top surface were marked with arrows as in Figure 3.20. The auxetic behaviour continues until around 7 mm deflection. Lower struts start to break and slightly slanting was become visible at around 10 mm deflection. Then, the contact between lattice walls and resistive effect of ligaments caused a high reaction force through local bucklings and local contact forces between unite lattice walls. It seems that upper and bottom lattice rows collapsed locally and made a slanting movement; two lattice rows in the middle have not started to collapse after 15 mm deflection yet. The system endured until a high level of loading, later the material could not stand anymore and failed at the lower and upper part. The failures observed includes buckling, slanting. Similar motion sequences were observed in all three repeated tests.

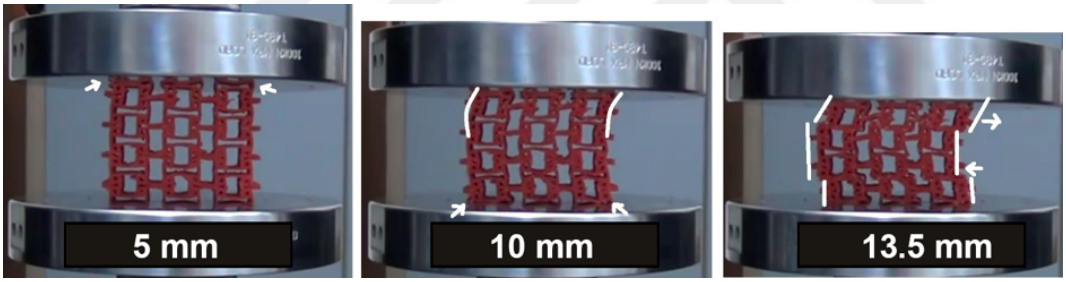

Figure 3.20 : Critical crushing times of the anti-tetrachiral lattices.

Re-entrant hexagonal lattices showed longer elastic phase due to the nature of the unit cell, which provides better energy absorption ability. When the vertical struts and thick mid-walls of each array touch each other, the structure starts to store the energy of elastic and plastic deformation due to the more constrained organization of unit cells. The collapse of this design showed that it collapses easier than anti-tetrachiral lattices. The struts between lattices in the original design are thickened to enhance energy absorption capability and not to separate of lattices from each other easily. λl represents the thickened sections in Figure 3.3. Figure 3.21 depicts a summary of the crushing characteristics of modified re-entrant hexagonal lattices. Both elastic and auxetic characteristics continue until almost 11.5 mm deflection. A significant number of local bucklings on the struts developed after 15 mm deflection. Subsequent phase

shows an increase of local buckling events, however, after 17 mm deflection, slanting movement develops on the block of the lattices.

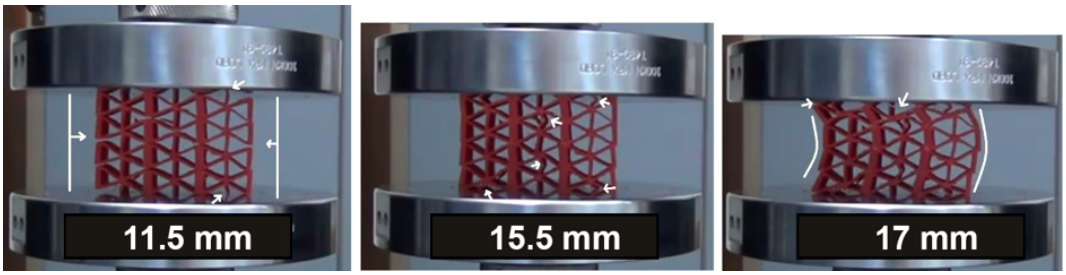

Figure 3.21 : Critical crushing times of the modified re-entrant hexagonal lattices.

3.6.4 Comparison of experimental and numerical results

Firstly, a mesh sensitivity study was conducted for different unit cell dimensions. The force-deflection comparison of the numerical model and experimental test is illustrated in Figure 3.22 and 3.23 for anti-tetrachiral and re-entrant lattices, respectively. Figure 3.22 depicts the correlation between the experimental and numerical results of the mean crushing force and absorbed energy, respectively. The crushing response of numerical models is similar to the experimental results. However, experimental results of re-entrant hexagonal lattice system showed more energy absorption compared to the numerical analysis. The imperfections, yield stress and stiffness of the material are the main parameters to predict the response of the design. Due to the nature of 3D FDM printing process of ABS polymer material, anisotropy, brittleness and imperfection cause some differences in predicting buckling deformation or buckling shape of the lattice systems. Although the behaviour of the material is assumed as isotropic in numerical analyses, the results obtained were close to that of the experiment.

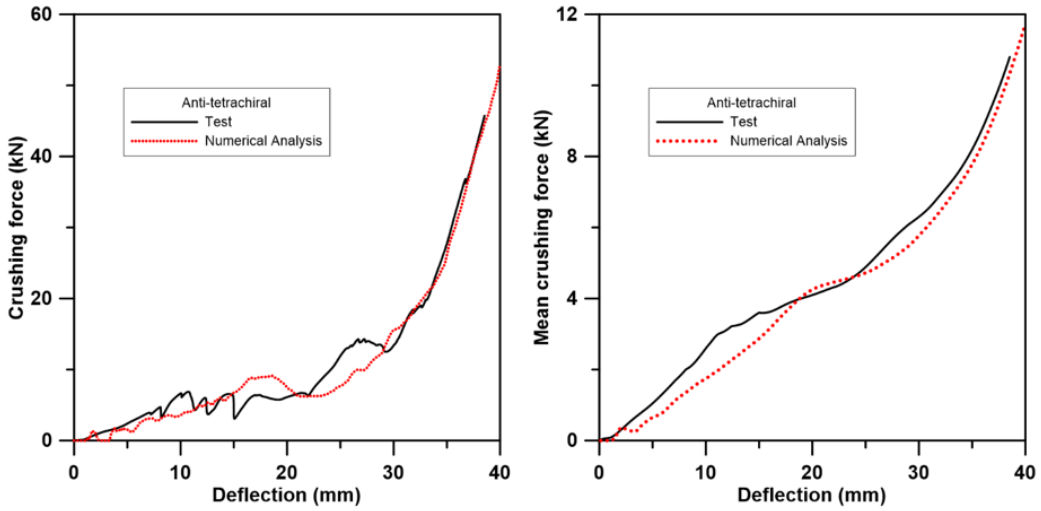

Figure 3.22 : Comparison between numerical and experimental results of anti-tetrachiral lattices.

For better understanding, the elaboration of numerical results is needed. In the experimental results of the anti-tetrachiral lattices, it is shown that the vertical struts of the top lattices failed at 5 mm deflection in a local buckling and crushing manner and this phenomenon causes an almost linear increase of the crushing force as seen in Figure 3.27. Furthermore, slight slanting can be monitored on the left upper side of the anti-tetrachiral lattices which whipped up the sliding of the middle unit cell network and premature global buckling. However, in the FEM analysis, this phenomenon is not deployed to prevent the increase of computational cost due to the usage of failure criteria. Instead of buckling and crushing, upper and lower vertical struts touching the crushing plates slid out of the geometrical boundaries and become lateral in the range of 5 to 15 mm deflection. The global buckling is observed in the experiment under 10 mm deflection, however, in the analysis, it is not experienced even under high local buckling formation due to lack of failure. The onset of global buckling can be seen under the 15 mm deflection in the FEM analysis, where the same deformation pattern and crushing load is obtained under the 20 mm deflection in the experimental results. After the displacement of 30 mm, where the densification phase is strongly dominating, the correlation of FEM and experimental results are high by reason of crushed lattices behave like a constituent solid material in the densification phase.

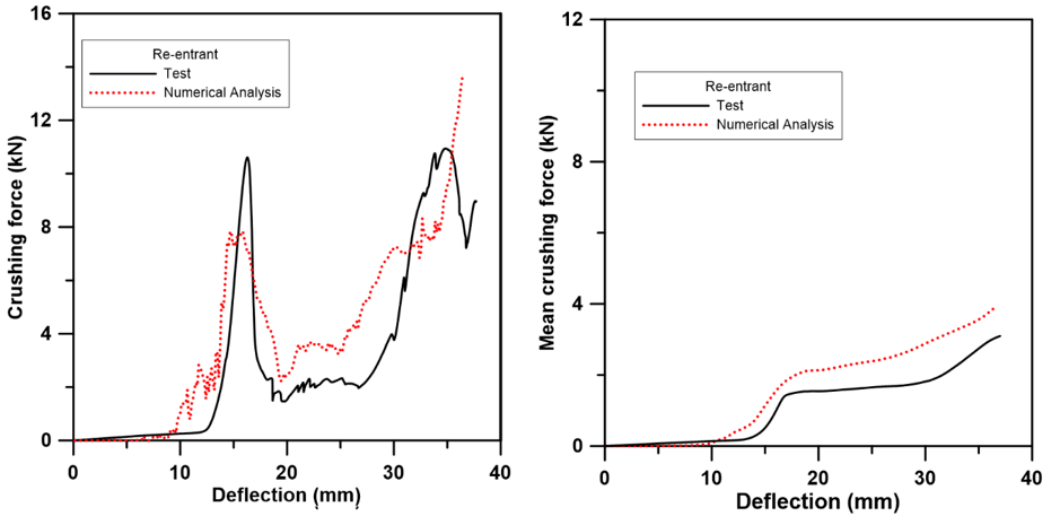

Figure 3.23 : Comparison between numerical and experimental results of re-entrant lattices.

Considering modified re-entrant lattices, in the experimental results, the local buckling of struts starts from the vertical struts on the lower-right side of the lattice structure. The local buckling of mentioned strut under 5 mm deflection triggers the failure of lower and upper vertical struts. However, in the analysis, local buckling formation starts from the upper vertical struts on both sides. Upper and lower vertical middle struts experienced only compression deformation without any local buckling until 15.5 mm deflection. Under the 10 mm deflection, deformations are observed in both the upper and lower side of the lattice structure but in the analysis, deformation starts only from the upper side and it proceeds to 15 mm stroke. In the modified re-entrant structures, vertical thick mid-wall elements are important to absorb energy by compression without performing any premature buckling. For this phenomenon, they start to touch each other after local collapses on the vertical axis to absorb more energy. In the analysis, this phenomenon is captured for the thick mid-walls but it cannot be captured for the vertical thinner struts on both sides. The dislocation of the thinner struts which are located on both sides of the modified re-entrant lattices can be explained by the lack of failure criteria in the analysis, and the local buckling behaviour of the inner vertical thin struts forced to change the orientations of them. The densification phase results of experiment and FEM are quite far due to the higher inner gaps of anti-tetrachiral lattices.

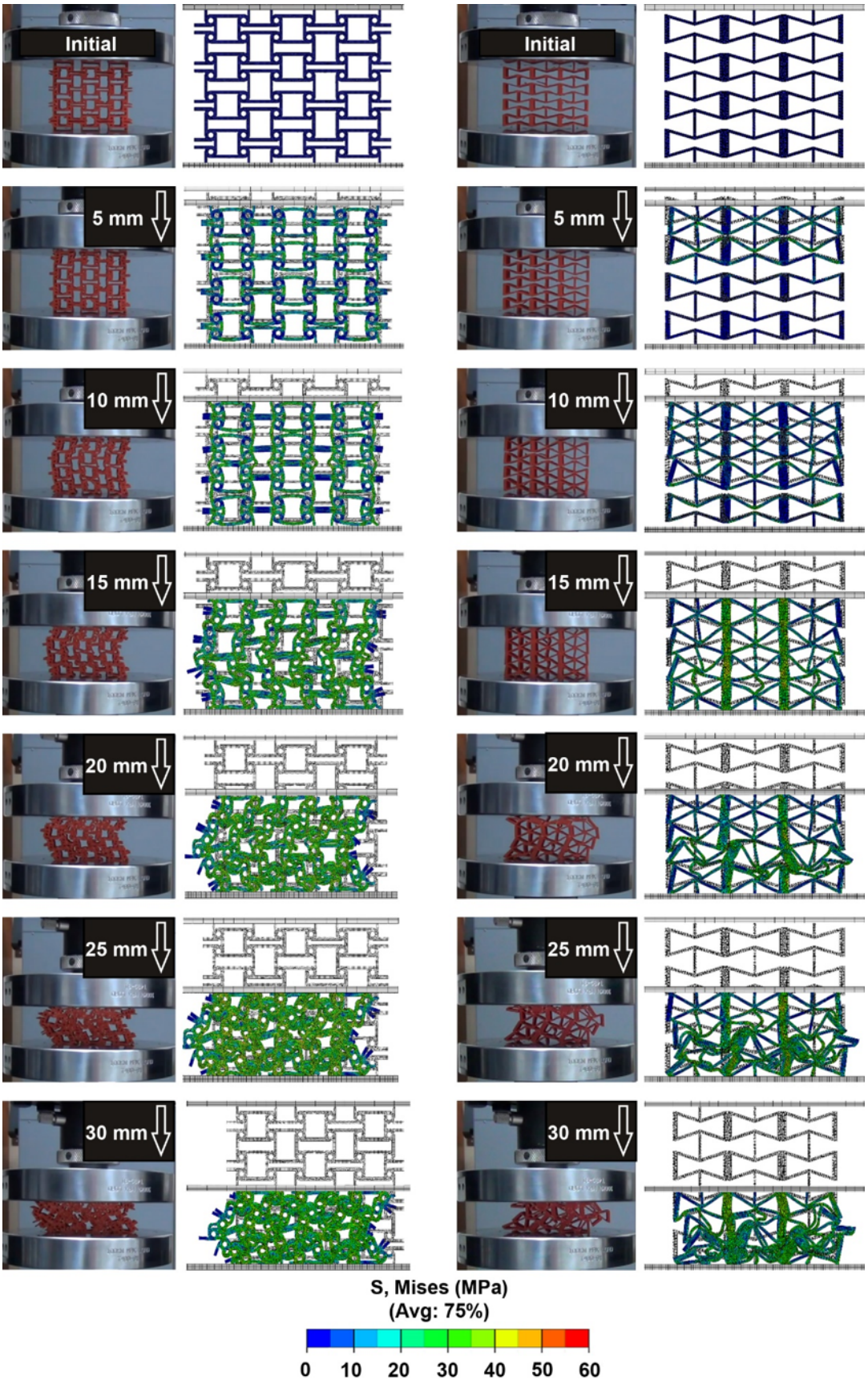

Figure 3.24 : The deflection images of the samples at every 30 seconds from the initial to the final state at 180 seconds.

3.7 Benchmark Study

In the previous section, re-entrant and anti-tetrachiral typologies were compared due to their ability to have similar box-volume, and being a good candidate topologies for comparing re-entrant and chiral auxetic mechanisms. Moreover, it was proved that the anti-tetrachiral topology showed better energy absorbing ability in comparison with re-entrant topology even improvements in the re-entrant topology. In this section, it is aimed to find best chiral topology in the chiral auxetic family in terms of energy absorbing by comparing their SEA and CFE values. For this purpose, a numerical model is validated with a experimental study, and validated numerical model is used for the crush analyses of the members of the chiral family for benchmark study.

3.7.1 Validation study

The hexachiral lattice structures were compressed in the flatwise direction, where axueticiy can be experienced, between two rigid plates by using a quasi-static loading process, and the crosshead velocity was kept at 10 mm/min. The compression tests were performed using an Instron Universal Testing Machine model 5890 with 100 kN loading capacity, tests were recorded by using a camera, and their load-displacement diagrams were sketched based on the testing machine data. For determining the effect of chiral lattices on the energy absorption, four specimens were tested during quasi-static crushing tests. Furthermore, FEM study was conducted by using ABAQUS-Explicit. The tensile tests material data was used for explicit analysis, and the anisotropic behaviour of the 3D printed material was neglected. The chiral lattice structure was crushed between two discrete rigid elemented plates, and a mass scale was used to reduce simulation time. The kinetic energy to total energy ratio was checked during to analysis, and this ratio must be less than 5% [91]. The total number of nodes was 47439, the total number of elements was 31080, and 31080 linear hexahedral reduced integration elements of type C3D8R was used. Penalty contact algorithm with 0.2 friction coefficient was used as the general contact. The comparison of the experimental and FEM results is given in Figure 3.25 and 3.26. As a result, quite close corelation relationship was captured between numerical and experimental studies.

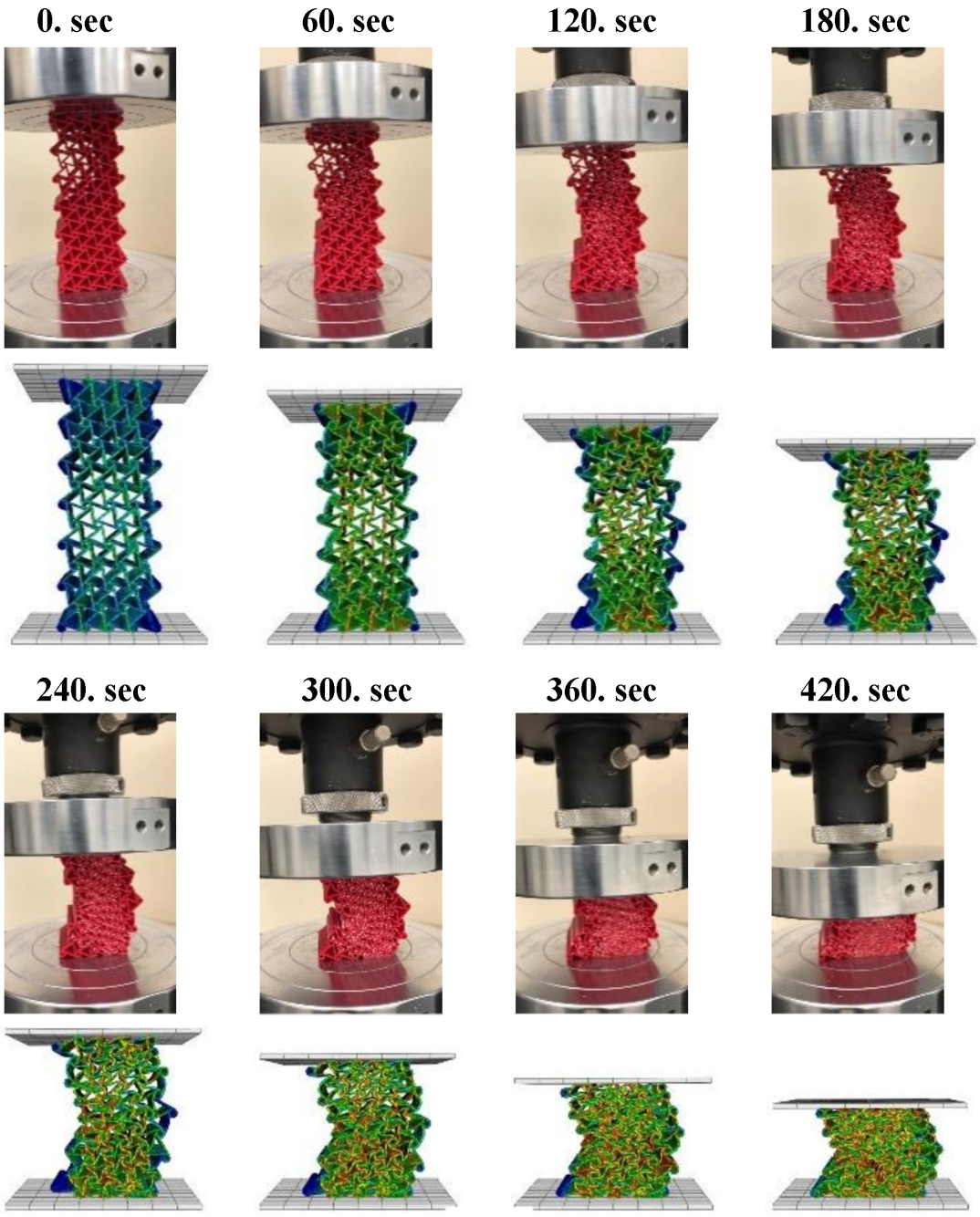

Figure 3.25 : The deformation pattern comparison of the experimental and FEM results.

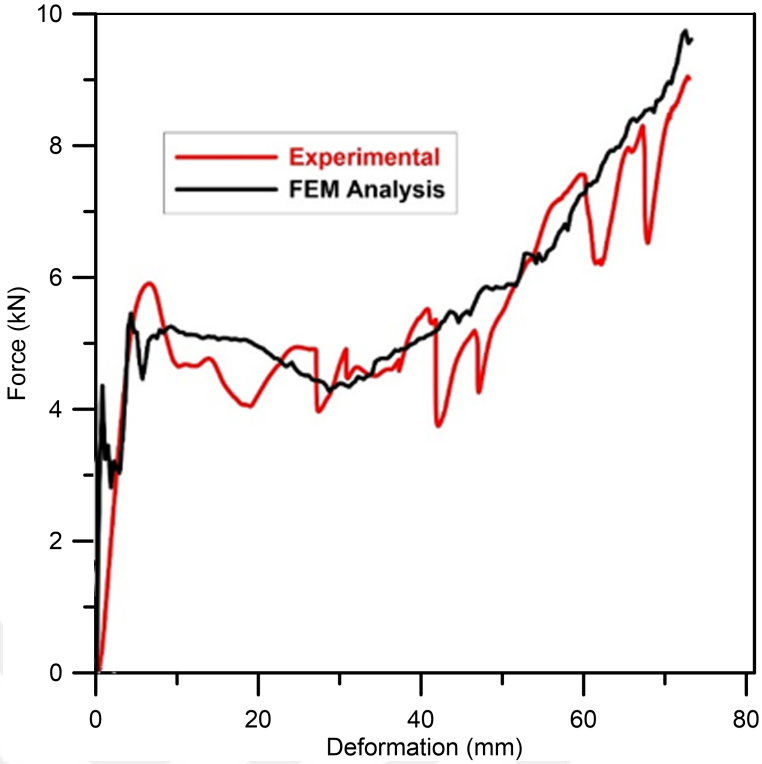

Figure 3.26 : The comparison of the experimental and FEM results for validation.

3.7.2 Results

After validation study, same variables were used to measure crushing performance of hexachiral (chiral), tetrachiral, anti-tetrachiral, trichiral, anti-trichiral and regular honeycomb lattices (Figure 3.27). They were all crushed quasi-statically with 10 mm/min using ABAQUS Explicit analysis. To measure the crushing performance of auxetic lattices specific energy absorption (SEA) and crushing force efficiency index (CFE) were used which are given in Section 3.5. The outline dimension of hexachiral (chiral), tetrachiral, anti-tetrachiral, trichiral, anti-trichiral andregular honeycomb were 147x63, 118x50, 117x50, 147x63, 140x60, and 136x50 mm, respectively. The extrusion length for all type of lattices was 10 mm, and the ligament thicknesses were kept in same dimensions for all topologies to compare them in a same manner.

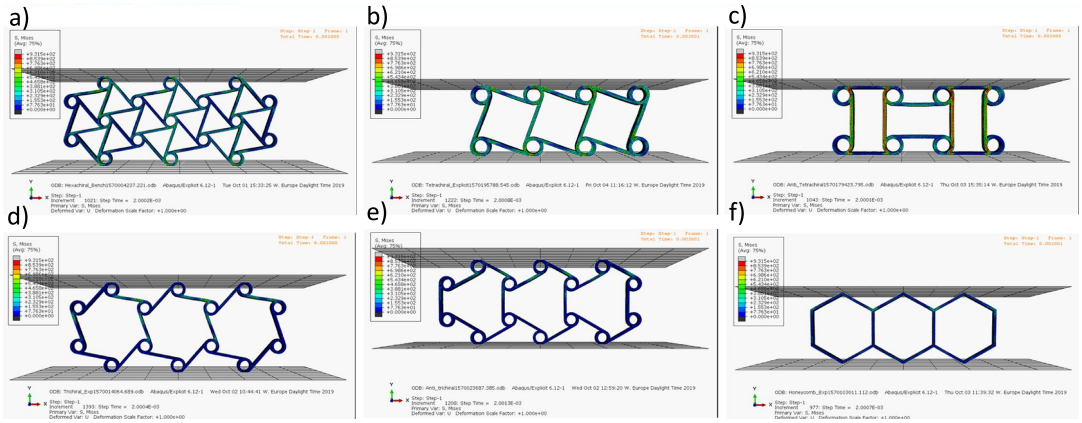

Figure 3.27 : a) hexachiral (chiral) b) tetrachiral c) anti-tetrachiral d) trichiral e) anti-trichiral f) regular honeycomb

The SEA and CFE values for anti-tetrachiral, re-entrant, chiral circular and chiral hexagonal auxetic lattices are given below Table 3.4.

Table 3.4 : CFE and SEA values of a)hexachiral (chiral) b)tetrachiral c) anti-tetrachiral d) trichiral e) anti-trichiral f) regular honeycomb.

	a	b	c	d	e	f
CFE	0.92	0.58	0.26	0.70	0.53	0.61
SEA(kj/kg)	3.73	1.59	3.12	1.90	2.25	2.37

To measure edgewise crush performance of five different auxetic lattice structures having chiral deformation and regular honeycomb lattice structures, quasi-static experimental tests and FEM analysis were conducted. A validation study was also conducted for chiral auxetic lattices to validate the FEM results, and a good correlation was captured. Same parameters were used to analyse the crushing performance of anti-tetrachiral, re-entrant, chiral and chiral hexagonal auxetic lattices. As a result, chiral auxetic lattice structures have the highest energy absorption capability comparing with trichiral, anti-trichiral, anti-tetrachiral, tetrachiral, anti-tetrachiral and regular honeycomb lattice. The crush force efficiency values of chiral hexagonal auxetic lattices was also better than other compared lattice structures. SEA value of the tetrachiral, anti-trichiral and regular honeycomb is nearly the same under quasi-static load with the velocity of 10 mm/min.

3.8 Overview and Discussion

A comparison study on the in-plane quasi-static crushing response of anti-tetrachiral and modified re-entrant lattices have been presented. Anti-tetrachiral lattices

showed better energy absorption per mass capability than modified re-entrant lattices. Deformation modes exhibited similar results at repeated tests. Auxeticity was observed only in elastic deformation for both types of lattice structures. However, modified re-entrant lattices exhibited elastic deformation for a longer duration. Therefore, we can obtain lower reaction forces at modified re-entrant designs. The thick mid-walls are the source of the energy absorption mechanism of the re-entrant design. Anti-tetrachiral lattices could only deform through two types of motions; slanting in several rows and local crushings in ligaments. That type of motion is closely related in-plane strength of lattices thanks to the corner ligaments. And repeated tests showed similar slanting motion. Theoretical prediction of the in-plane stiffness (E_y) through the value of vertical strut's ratio to ligament radius (α_y) was well-matched with the deformation modes of experiments. However, instability after increased deformation causes behaviour which is difficult to predict due to material inhomogeneity, defects, and defects location. Therefore, further parametric and experimental investigation regarding instabilities can benefit the understanding of the theoretical estimation. The numerical crushing study achieved for both geometries and captured the results of experimental tests well. The mass scale method is used to decrease computational costs. Basic modes were captured similar in both experiments and analyses. That gives the opportunity to model new anti-tetrachiral and modified re-entrant cells with new design purposes and without new manufacturing costs. However, it should be pointed out that several fractures observed in the tests require fracture characterization of the struts to observe or take into account possible other effects such as released energy. Additionally, in the crush efficiency comparison of five different auxetic lattice structures having chiral deformation mechanism and regular honeycomb, hexachiral lattice structure showed the best SEA and CFE values.

4. CRUSH BEHAVIOUR OF AUXETIC FILLED TUBES

4.1 Introduction

Crush phenomenon can be encountered in many real-life situations, ranging from automobile accidents, space debris and bird strike in aircraft. Composite materials have extensively used in recent years for energy absorption applications because of their light weight, corrosion resistance and high energy absorption [98]. Numerous studies have been performed to understand the crushing behaviour of composite materials, and especially their failure mechanisms, which heavily depend upon the fiber and matrix properties [99]. A significant number of studies have also appeared in open literature about the effect of the stacking sequence [100–105]. Jacob et al. [98] have suggested that the overall energy absorption increases when fibers parallel to the loading direction were laterally supported, such as in the case of the [0/90/0/90]s layup. Moreover, the triggering mechanisms are quite important to generate a decrease of the peak forces. Siromani et al. [106] have identified optimal triggering mechanisms by obtaining a crush efficiency value equal to one, while providing the highest possible SEA. Tubes with chamfered, inward folding or outward-splaying crush-caps, or combined (chamfered-end and crush-cap) were investigated as designs with potential embedded failure triggering mechanisms. The chamfer failure trigger appeared to be the most effective at lowering the initial peak load and presenting a high value of SEA. Song et al. [107] have also investigated 45_o double chamfered designs as trigger mechanism. The initial peak load was observed to be lower in those double chamfered configurations, compared to specimen with either no trigger or single chamfered design. The tulip trigger can provide a higher steady-state crush load with higher SEA [108] in contrast to hourglass, crown and chamfer triggers [109]. Czaplicki et al. [110] also showed that the tulip triggering mechanism could achieve a better crush efficiency with a higher energy absorption compared to chamfered (bevel) triggering. The ratio of the fiber reinforced polymer (FRP) tube thickness to the outer diameter

(D) is an important parameter to determine the energy absorption and the deformation modes of carbon fiber/PEEK composite tubes [111–113]. Farley [114] showed the presence of a nonlinear variation of the energy absorption versus this ratio. Hamada and Ramakrishna [115] has observed that the highest SEA values could be obtained by using 2-3 mm thickness tubes. Gupta et al. [116] have also demonstrated that by maintaining the D/t ratio between 15 and 40 one can prevent the global buckling and the catastrophic failure of axially crushed composite circular cross section tubes. The crush tube length should also be determined by considering the crash speed: if the crash velocity is too high, the crushing stroke can be insufficient, and a very high peak load can rise. In this case, either the crush tube length is to be extended or a filler material must be used.

In this chapter, it is presented that the experimental evaluation of tubes filled with chiral lattices to potentially increase the crashworthiness performance of composite tubes. The chiral lattices are manufactured in ABS (Acrylonitrile Butadiene Styrene), and by using a 3D printing facility. Commercial CRFP (Carbon fiber Reinforced Plastic) tubes are used in quasi-static compressive tests. The tubes are filament wound and pultruded, with a [0/+-38/-89] stacking sequence which is a commercial product. Chiral lattices, hollow and chiral lattices filled tubes are axially and laterally compressed between two rigid plates during the quasi-static test process. In these tests the crosshead speed is kept at 10 mm/min. The specific energy absorption, peak load, average (mean) crushing load, crushing efficiency and stroke efficiency have been then calculated and compared with the hollow tube cases, to understand whether auxetic structures could be beneficial or not in designing efficient composite crushing tubes.

4.2 Deformation Modes for Composite Tubes

Considering design process of laminated composite material, design complexity is inevitable. Some factors affecting design complexity can be grouped as high number of design parameters and mechanical behaviour specifications. The design parameters include the material configuration and geometry of the constituent. The geometry parameters are the shape of component, its length and the size of cross-sections. Moreover, material parameters are composite laminate layup and stacking sequence, material data such as matrix and fibre materials' mass density or Young's modulus and

the thickness of composite laminates. Mechanical behaviour consists of deformation modes, stiffness and structural interaction of the system. Most importantly, stiffness and failure modes determine the crash performance of the structure and also its deformation resistance [116, 117].

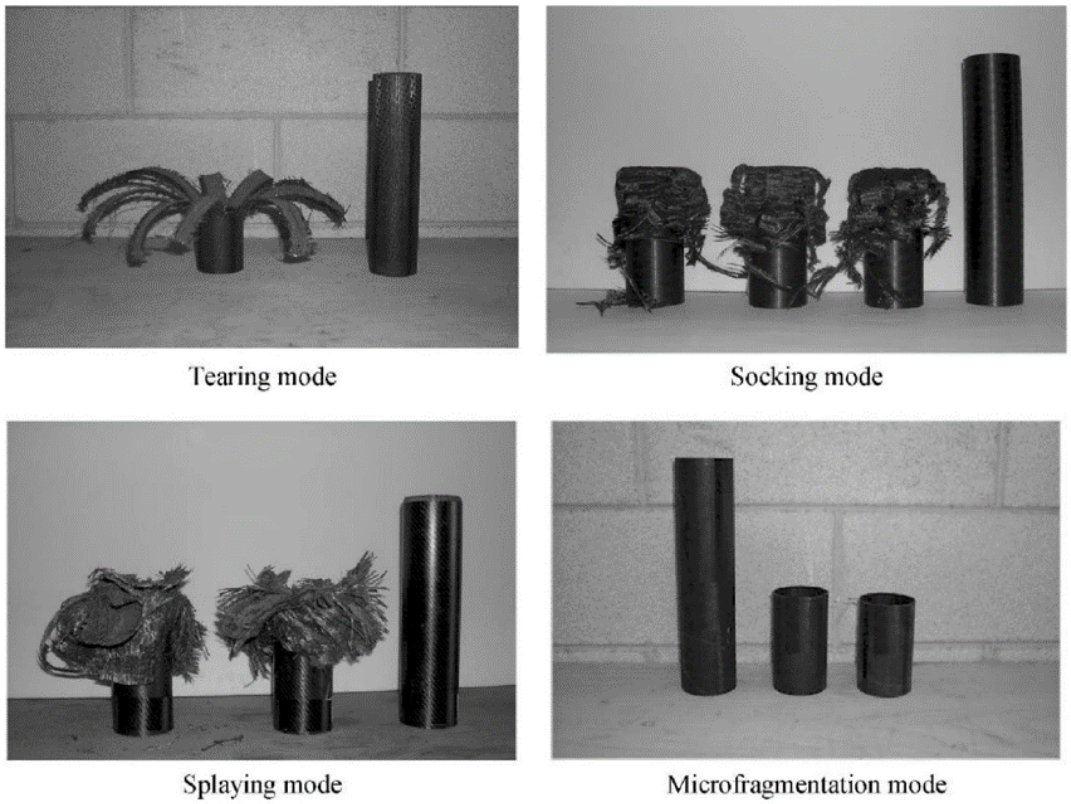

Figure 4.1 : Collapse Modes [120].

Consequently, laminated composites have more distinctive failure modes comparing with metals [22, 118, 119]. Considering crush of the carbon fibre composite tubes with epoxy matrix in general, the collapse modes can be grouped as tearing mode, socking mode, splaying mode and micro fragmentation mode in macro-scales [120]. In the tearing mode, a small part of the tube wall folds inward and at the same time the outside part of the wall folds outward nearly getting any damage. As seen from the Figure 4.1, final deformation is similar to flower petals. In the socking mode, the outside of the tube wall separates and bends outward with being together and it is also pushed back. The term of socking mode, as it comes from to the similarity of the away a sock goes down over the foot. The splaying mode includes delaminations and parallel cracks to the fibres. The last one is 'micro fragmentation mode' and in this mode the crushed part is reduced to pulverised material. The collapse modes under crushing

load depends on the type of matrix, the volume fraction of fibres and the orientation of the plies [121].

4.3 FEM Material Models

The change of relatively small variation in design parameters can result in large differences in structural response in the collapse modes of composite materials, when compared to metallic structures. This causes an increase in the complexity of designing CFRP components and determining its crush behaviour. To determine crush behaviour of a CFRP structures, experimental methods cannot always be used because of time and high cost issues so simulation methods are needed. Nonlinear transient dynamic analysis methods are generally used for simulating a crush event especially FEM explicit [122]. LS-Dyna and ABAQUS are mostly used for simulating crush event of composite materials and some material models were improved to use in these commercial. Furthermore, most of the composite materials reinforcement materials such as carbon fibre and glass fibre are very brittle materials so a failure criteria is needed for modelling to approach close results of experimental tests. In addition, for better results in the numerical simulations for composites, needed material specifications must be provided in precise manner, and more material data is needed for failure criteria. Especially, for the commercial end product composite materials in the different shape likewise in the form of cylinder and pipe which is not providing to cut out coupons to have material properties.

4.3.1 Hashin's failure criteria for composites

Hashin's Failure criteria [123] were originally developed for unidirectional polymeric composites however it can be used for other type of laminates and non-polymeric composites. Hashin criteria is implemented in two-dimensional (shell element) classical lamination approach for point stress calculations. Furthermore, ply discounting utilized as the material degradation model. Failure indices for Hashin criteria are related to fibre and matrix failures and involve four failure modes. The criteria can be extended to three dimensional problems where the maximum stress criteria are used for transverse normal stress component. The failure modes included in Hashin's criteria are as follows.

1. Tensile fibre failure for $\sigma_{11} \geq 0$

$$\left(\frac{\sigma_{11}}{X_T}\right)^2 + \frac{\sigma_{11}^2 + \sigma_{13}^2}{S_{12}^2} = \begin{cases} \geq 1\, failure \\ \leq 1\, no failure \end{cases} \tag{4.1}$$

2. Compressive fibre failure for $\sigma_{11} \leq 0$

$$\left(\frac{\sigma_{11}}{X_C}\right)^2 = \begin{cases} \geq 1\, failure \\ \leq 1\, no failure \end{cases} \tag{4.2}$$

3. Tensile matrix failure for $\sigma_{11} \leq 0$

$$\frac{(\sigma_{22} + \sigma_{33})^2}{Y_T^2} + \frac{\sigma_{23}^2 - \sigma_{22}\sigma_{33}}{S_{23}^2} + \frac{\sigma_{12}^2 + \sigma_{13}^2}{S_{12}^2} = \begin{cases} \geq 1\, failure \\ \leq 1\, no failure \end{cases} \tag{4.3}$$

4. Tensile matrix failure for $\sigma_{11} \leq 0$

$$\left[\left(\frac{Y_C}{2S_{23}}\right) - 1\right]\left(\frac{\sigma_{22} + \sigma_{33}}{Y_C}\right) + \frac{(\sigma_{22} + \sigma_{33})^2}{4S_{23}^2} + \frac{\sigma_{23}^2 - \sigma_{22}\sigma_{33}}{S_{23}^2} + \frac{\sigma_{12}^2 + \sigma_{13}^2}{S_{12}^2} = \begin{cases} \geq 1\, failure \\ \leq 1\, no failure \end{cases} \tag{4.4}$$

5. Interlaminar tensile failure for $\sigma_{33} \geq 0$

$$\left(\frac{\sigma_{33}}{Z_T}\right)^2 = \begin{cases} \geq 1\, failure \\ \leq 1\, no failure \end{cases} \tag{4.5}$$

6. Interlaminar compression failure for $\sigma_{33} \leq 0$

$$\left(\frac{\sigma_{33}}{Z_C}\right)^2 = \begin{cases} \geq 1\, failure \\ \leq 1\, no failure \end{cases} \tag{4.6}$$

where, σ_{ij} denote the stress components and the tensile and compressive allowable strengths for lamina are denoted by subscripts T and C, respectively. X_T, Y_T, Z_T denotes the allowable tensile strengths in three respective material directions. Similarly, X_C, Y_C, Z_C denotes the allowable compression strengths in three respective material directions. Further, S_{12}, S_{13} and S_{23} denote allowable shear strengths in the respective principal material directions.

4.4 Material

The produced chiral structure consisted of 10 unit cells. The production and the out-of-plane geometry cell parameters of the chiral lattice is illustrated in Figure 4.2. The ratio of R to r_0 is equal to 2.40. The outer diameter, r_0, is 4.39 mm, the inner diameter, r_i, is 2.63 mm, and the angle of the ligament, θ, is 30°. The height of the chiral structure is 100 mm, and its mass is 54.61 gr.

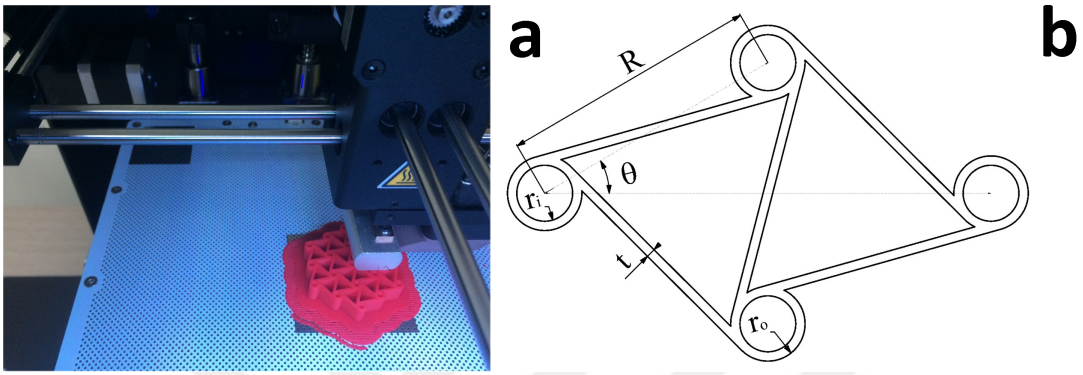

Figure 4.2 : Chiral axuetic lattice a) production stage b) topology parameters.

CRFP tubes used in the experiments are filament wound and pultruded composite tubes with a thermoset resin, stacking sequence [0/±38/-89] and 100 mm of length. The mass of each tube was 39.46 gr. The outer diameter is 50 mm and the wall thickness 2 mm. The ends of the tubes were cut out to ensure that the tubes are free from burrs or uneven edges (Figure 4.3). Also, no trigger mechanism is used in the tests, with both ends of the tubes being flat.

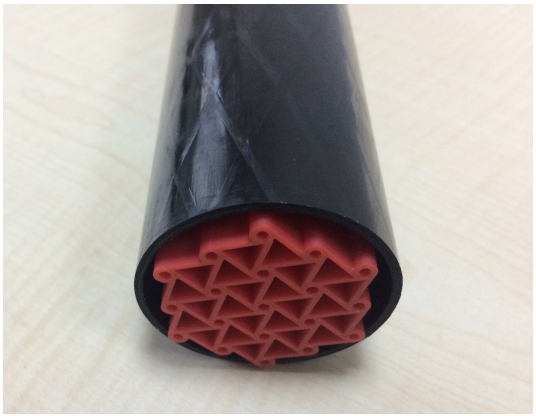

Figure 4.3 : Chiral structure filled composite tube.

4.5 Experiments and Results

Chiral lattices, hollow and chiral lattices filled tubes are axially and laterally compressed between two rigid plates by using a quasi-static loading with crosshead speed kept at 10 mm/min. The compression tests are performed using an Instron Universal Testing Machine model 5890 with 100 kN loading capacity. The undeformed and deformed chiral lattice structures can be seen in Figure 4.4.

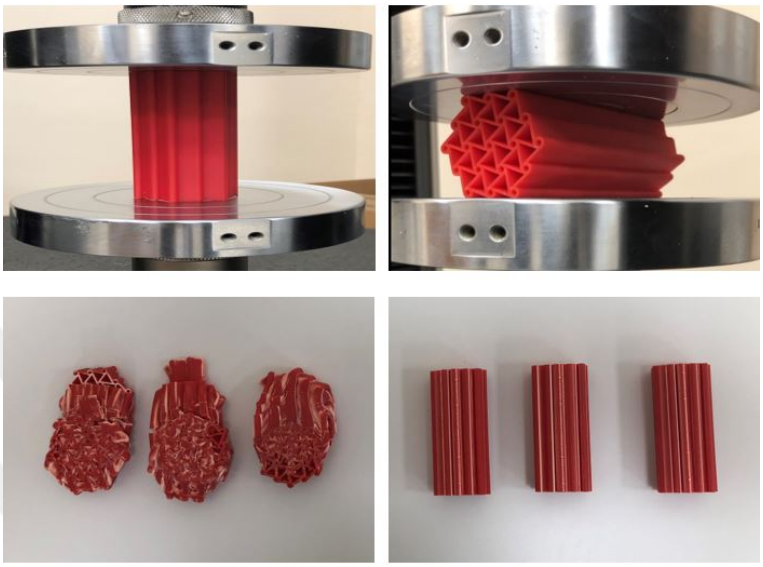

Figure 4.4 : Produced chiral lattice and its uniaxial and lateral crush of chiral auxetic lattices.

The SEA values for out-of-plane crush of chiral lattices was found to be 3.86 kJ/gr and for in-plane SEA value is 10.55 kJ/gr. The in-plane and out-of-plane load-displacement curves of chiral lattices could be seen in Figure 4.5 and Figure 4.6.

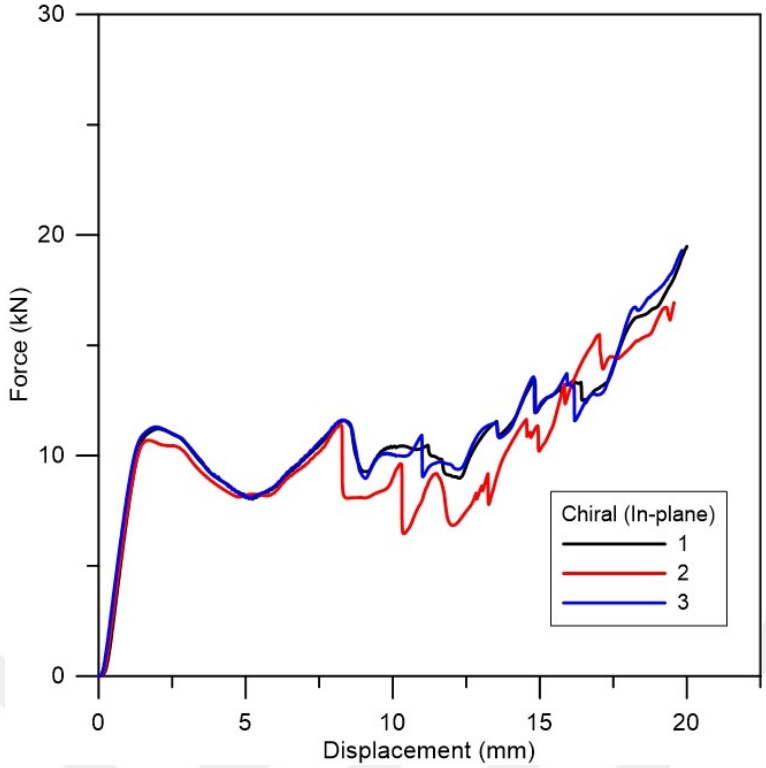

Figure 4.5 : Force – displacement curves related to the in-plane crush of chiral lattices.

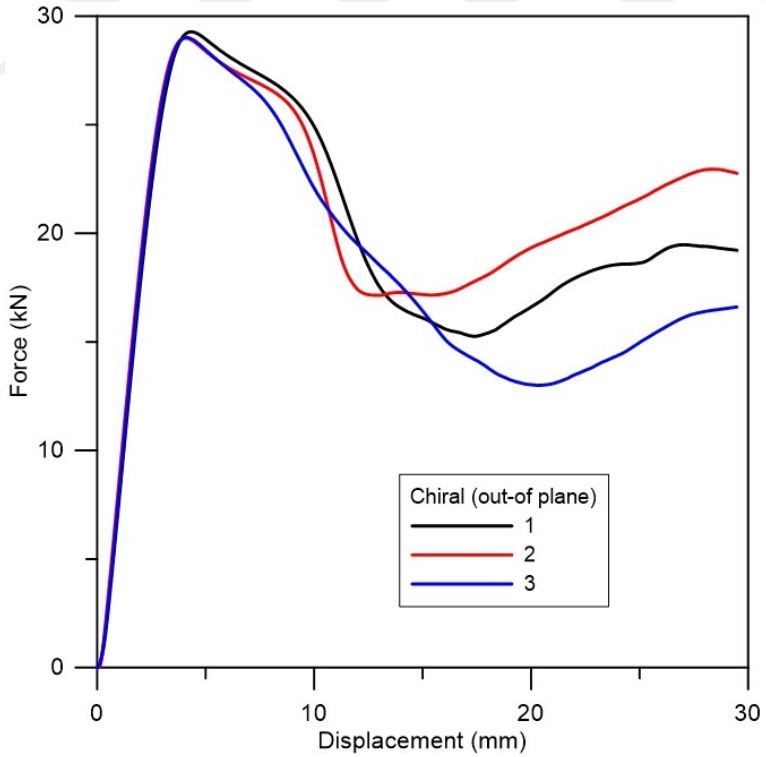

Figure 4.6 : Force – displacement curves related to the out-of-plane crush of chiral lattices.

The axial crush test stages for the hollow and chiral lattices filled composite tubes can be observed in Figure 4.7. The representative experimental results of the compression tests for hollow composite tubes are shown in Figure 4.9. Global buckling and catastrophic failure have not been observed, and the general deformation behaviour was more alike a progressive failure, which is indeed the type of desired failure mechanism [124]. An ideal progressive failure can be easily appreciated.

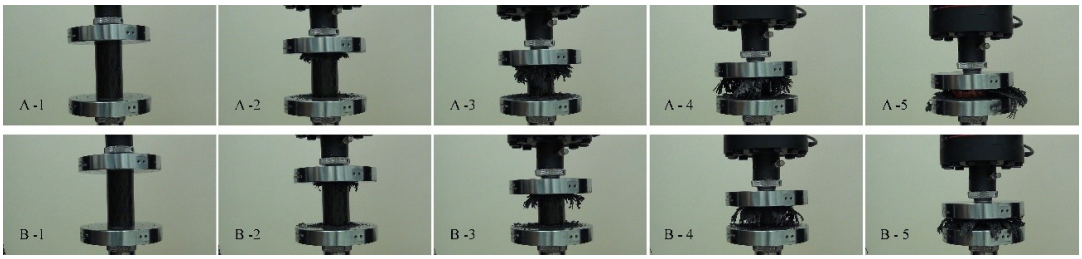

Figure 4.7 : Crushing stages of hollow (A) and chiral lattices filled (B) tubes.

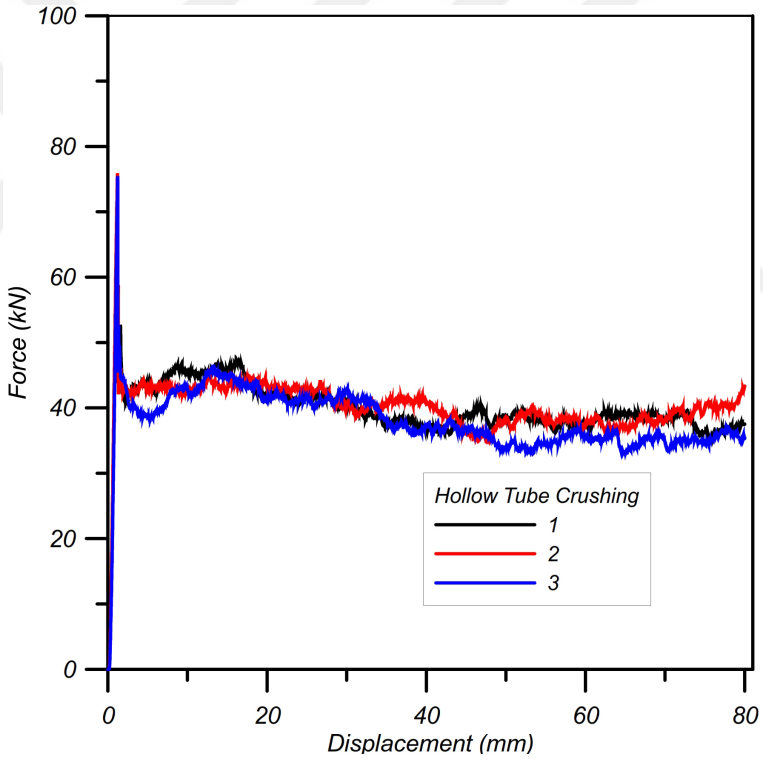

Figure 4.8 : Force – displacement curves related to the hollow composite tubes.

The presence of a tearing mode and micro-fragmentation have been also observed (Figure 4.9) and these failure mechanisms are also presented in Bisagni's work [120]. The existence of similar failure modes could also be observed in the chiral lattices filled composite tubes, until a specific compression stroke which is 80 mm. Beyond that critical value, the chiral lattices expanded laterally and forced the wall of the composite tubes to move radially, which caused a catastrophic failure. That is the main reason

that all the composite tube material surrounding the chiral lattices are deformed and split, and some undeformed large pieces of the composite parts are left at the end of the tests.

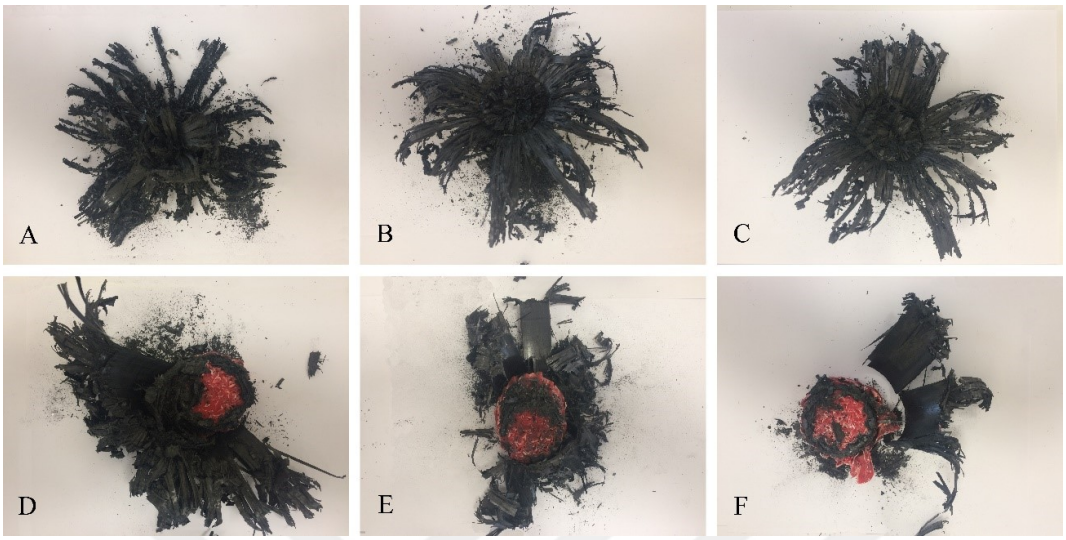

Figure 4.9 : Deformed (A, B, C) hollow and chiral (D, E, F) lattices filled composite tubes.

The load–displacement curves for the chiral lattices filled composite tubes are presented in Figure 4.10. The densification starts at about 55 mm of compression (55% of stroke length), and two different peak loads can be observed. The first peak is correlated to the failure of the composite tube; the second one is related to the collapse of the chiral lattices.

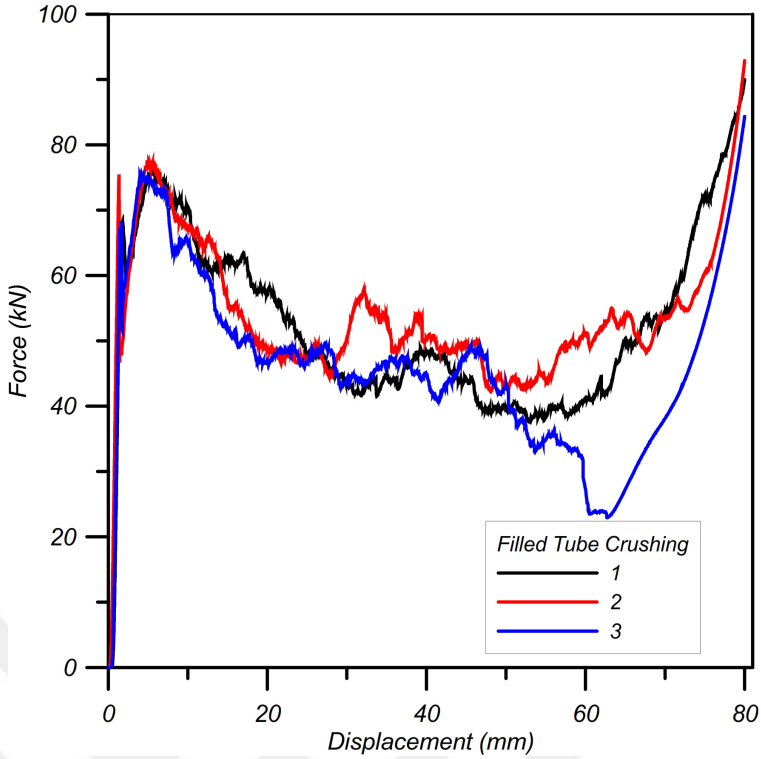

Figure 4.10 : Axial force – displacement diagram for the chiral lattices filled composite tubes.

In the case of the lateral (radial) compression, two different energy absorbing processes occur when the load is applied. One of them is related to the flattening of the tubes cross sections curvature, while the other one is about the presence of hinge lines as seen in Figure 4.11. The two energy absorption processes could be observed for both the hollow and the chiral lattices filled tubes.

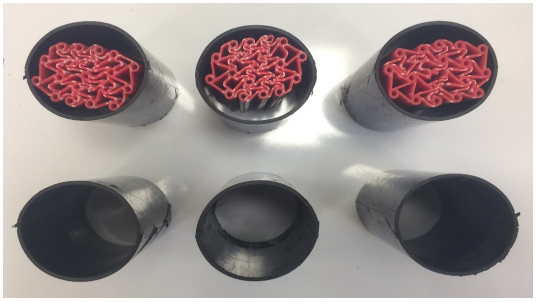

Figure 4.11 : Deformed hollow and chiral lattices filled composite tubes under lateral loading.

During the lateral compression both elastic and plastic deformations occur. After the load is removed at the end of the test, it was noticeable how the tubes wall returned to its original shape. The final dimensions of the deformed tubes (hollow and chiral lattices-filled) are almost the same. In contrast to the axial compression case, a

significant in-plane deformation of the chiral lattices auxetic behaviour was observed, and the chiral honeycomb does not expand under lateral loads as seen form Figure 4.14. From the observation of Figure 4.12, although the compression of the hollow composite tubes gives a fairly regular and smooth characteristic stress- strain curve, the shape of the same force-displacement diagram is more irregular in the case of the hexachiral-filled tubes due to the progressive deformation of the cells in the chiral structures as seen in Figure 4.13.

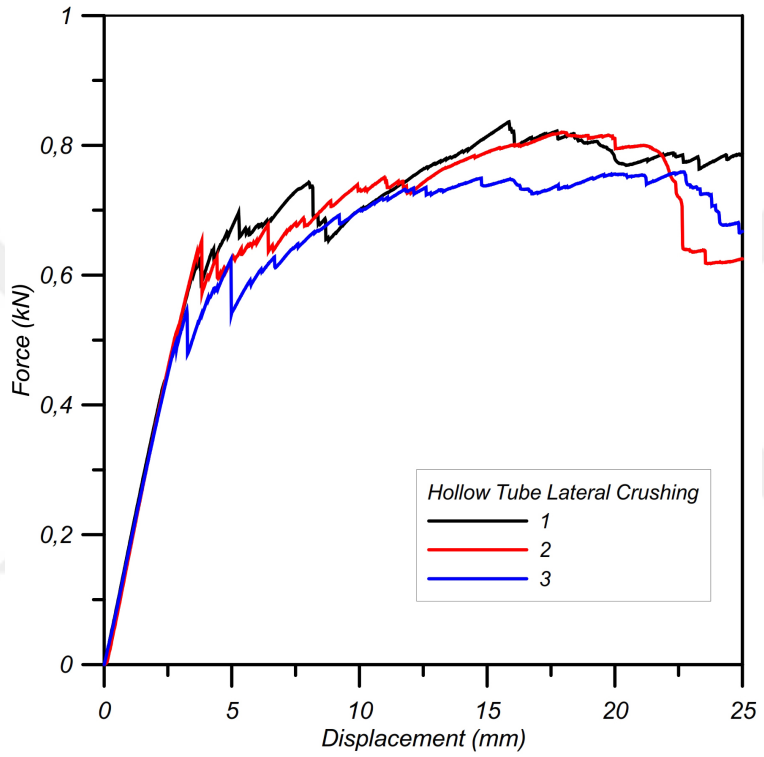

Figure 4.12 : Lateral force – displacement curves for the hollow composite tubes.

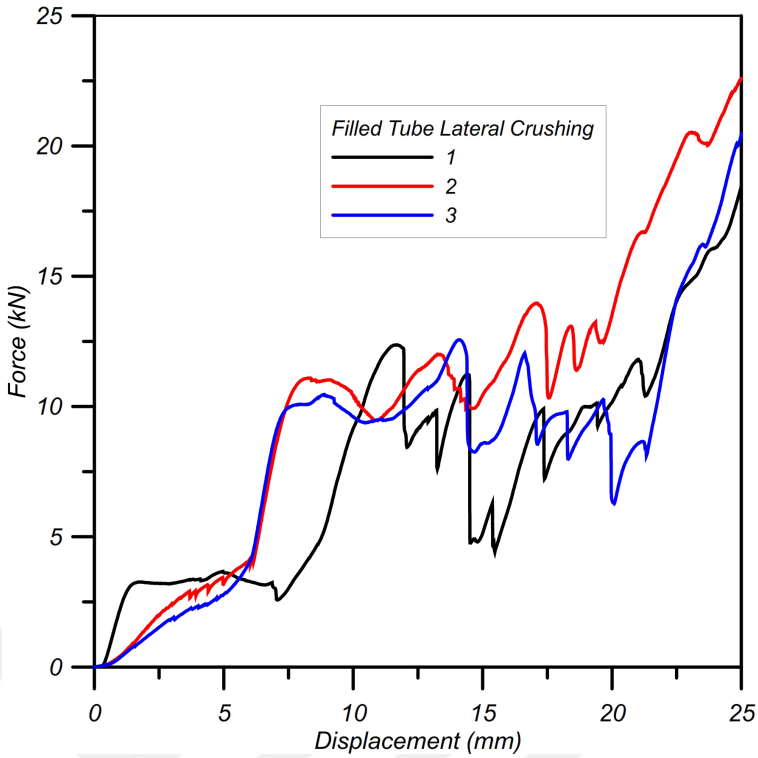

Figure 4.13 : Lateral force – displacement curves for the chiral-filled composite tubes.

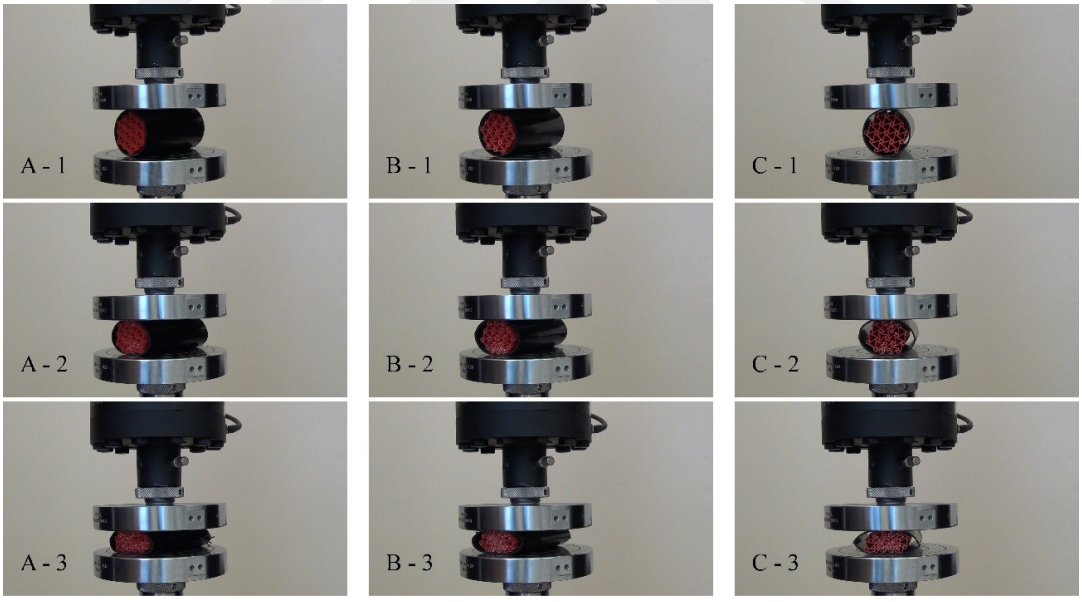

Figure 4.14 : Three different (A, B, C) lateral crushing processes of the chiral lattices filled composite tubes.

It is shown in Table 4.1 that the peak crushing force magnitude is almost same during all the tests (chiral-filled and hollow), and therefore the filling material does not appear to affect the peak crushing force. That means out-of-plane deformation of the chiral structure does not change the peak crushing force, however it affects the mean crushing

force, with a 10% increase. The same behaviour is observed indirectly in crushing force efficiency.

Table 4.1 : Crush properties of hollow and filled composite tubes under axial crush.

	Hollow Tubes			Chiral Filled Tubes		
	1	2	3	1	2	3
PCF (kN)	65.16	75.87	75.45	75.38	77.48	75.32
MCF (kN)	39.90	40.22	38.10	52.47	53.99	46.59
CFE	0.61	0.53	0.51	0.70	0.70	0.62
SEA (J/gr)	80.89	81.55	77.24	44.63	45.91	39.73

In terms of CFE, it is evident how the filling with the chiral lattices contributes to enhance the mechanical performance of the tubes. The absorbed total energy within 80 mm deflection increased about 30% with the use of the hexachiral structures; the specific absorption, which is one of the most important indexes for critical assessments, decreased however by 45%.

Table 4.2 : Properties of the hollow and filled composite tubes under lateral crush.

	Hollow Tubes			Chiral Filled Tubes		
	1	2	3	1	2	3
PCF (kN)	0.84	0.81	0.76	12.37	22.60	20.47
MCF (kN)	0.69	0.67	0.64	7.77	10.37	8.47
CFE	0.82	0.83	0.84	0.63	0.46	0.41
SEA (J/gr)	0.44	0.43	0.41	2.07	2.76	2.25

Table 4.2 illustrates the values of the peak crushing forces and SAE, while also providing the peak and mean crushing forces. The peak forces for the filled tubes are very high compared to the ones of the hollow tubes. The peak force and SAE values of the hollow and filled tubes do however differ, and this is due to the way the chiral structure contacts internally the inner part of the tube. Whenever chiral structure contacts the tube at only one point, the peak crushing force reaches 20 kN; in adverse condition, it decreases to a value of 12.4 kN where the rigid palate touches the inner part of the tube along two points. The SAE values were highly significant, and it is almost five times higher in comparison with the hollow tubes case. This is a clear indication of the negative Poisson's ratio effect of the hexachiral structures, which creates large equivalent densification and stiffening effects during the transverse compression loading, with only a limited amount of effective mass provided by the filling of the tube.

4.6 Overview and Discussion

Tensile and crushing tests have been performed on a series of composite CFRP tubes with hollow sections, and filled with an auxetic (negative Poisson's ratio) lattice built using a 3D printing technique. The specific energy absorption, peak load, average (mean) crushing load, crushing efficiency and stroke efficiency were calculated for the different configurations and assessed to understand whether auxetic structures could be needed for designing composite crushing tubes or not. Adding a chiral lattice filler did not increase the SEA capability of the tubes in the case of the axial quasi-static crushing; a significant decrease of the specific energy absorption was instead observed. Significantly, in the case of the lateral quasi-static crushing the SEA of the filled tubes increase by 450%, and this due to the auxetic mechanism triggered during the lateral compression. The peak forces do not increase under axial compression by using chiral filling materials. The use of these materials appears to increase the duration of the crushing force and the total absorbed energy values. The crushing force efficiency of the composite filled crushing tubes under axial compression increases when compared to the hollow tubes case. However, the high deformation present when the chiral lattices bottoms out could cause some significant lateral outward deformation that pushes against the composite tube walls. The chiral filling material placed in the composite tube increases significantly the peak forces and the SAE values during lateral compression. The use of chiral structures in their prismatic configuration allows to make use of the negative Poisson's ratio effect and therefore contribute to the artificial stiffening and densification effect that increases the SEA for these composite structures.

5. EBM TECHNOLOGY FOR CHIRAL LATTICE PRODUCTION AND COMPRESSION ANALYSES

5.1 Electron Beam Melting

Electron Beam Melting is a layer by layer fabrication method consists of sequential cycles to produce imported CAD drawings. Each solid layer is formed by metallic powder distribution and selectively melting. To maintain a clean and controlled build environment during the fabrication high vacuum environment is provided in the build chamber differently from other metallic AM methods. EBM produced Ti6Al4V parts are more ductile comparing to SLM and wrought produced parts because the unvacuumed environment in SLM and wrought production methods can cause gas bubbles being trapped in the molten region [125]. The metal powder is melted under vacuum conditions by an electron beam gun which has an ability to accelerate the free electrons to a velocity in between 0.1-0.4 times the speed of light that pulled off from a heated tungsten filament using an extreme voltage of 60kV [126]. The melting process of metal powders can be explained by the hitting of electrons to metal powder particles and transmitting the kinetic energy of the electrons to metal powder particles, and most of the kinetic energy is converted into the thermal energy, with this thermal energy, particles are melt and fused to each other regarding to electron beam energy and build layer thickness. However, layerwise production systems cause anisotropic material behaviour. Moreover, the process includes preheating the build chamber to a certain temperature and sintering every layer before melting which provides availability to produce floating parts in the powder bed, seen in Figure 5.1. The heat rate during preheating can be varied from the bottom to the top of the produced parts. This situation may cause different microstructure formation through the part height, thus local mechanical properties may form [127]. This is the reason why parts with less height are better produced using EBM technology, and one of the reasons to produce chiral cells parallel to the powder deposition direction.

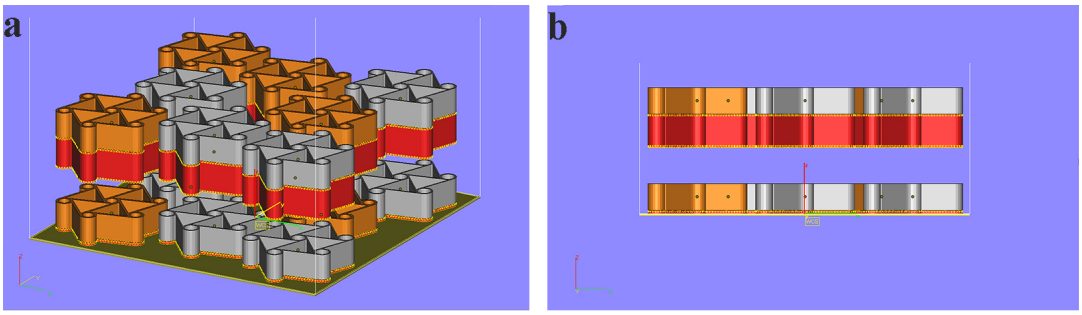

Figure 5.1 : Floating parts production in EBM: (a)iso view and (b) front view.

The beam in EBM is regulated by magnetic coils which concentrate and adjust the diameter and position of the beam and prevent astigmatism, and special algorithms are used to tune them. A building theme software is used to apply manufacturing parameters to control fabrication in order to produce low surface roughness and low porosity with improved mechanical properties and net-shaped parts. The main build parameters that can be controlled by the algorithms can be listed as beam current level, scan velocity, spot size, layer thickness, hatch distance, sintering path and rotation angle between consecutive hatches [128]. In the productions of this study, a particular build theme, which is given in Appendix A.1, and a layer thickness of 50 μm are employed.

EBM printed parts can be used as-built components, without any thermal treatment to obtain low residual stresses and reasonable ductility, unlike other known metal 3D printing technologies like laser engineered net shaping (LENS) or SLM. The high ambient temperature in the build chamber prevents the formation of α' martensitic brittle phase, and the slow cooling rates in EBM technology alleviates the large proportion of the residual stress [129]. However, the surface of the EBM printed parts can have high roughness which is caused by the powder sintering during the printing process. High roughness of the EBM printed parts may cause engineering stress calculation mistakes because the cross-section area cannot be the real effective area that supports the load. Moreover, the surface finish is an important parameter considering the mechanical performance of the EBM printed parts. Polished specimens exhibit better strain at break values comparing to asbuilt parts. The explanation for this phenomenon can be described by eliminating crucial porosities on the sample surface or regions very close to the sample surface. These types of defects can cause crack initiations, and therefore stress concentration and premature failure [130]. Also, in the

case of using produced parts as as-built parts without polishing process, loose leftover powder particles can take place on the surface, and they should be removed to take sensitive dimensional measurements.

Ti6Al4V metallic powder is the most common material for EBM due to its conductivity and superb mechanical specifications of high corrosion resistance, high specific strength, castability, plastic workability, weldability, and excellent biocompatibility; therefore titanium alloys are important materials for the fields of biotechnology and aerospace [131]. In this study, ARCAM A2 EBM system (Appendix A.2 for specifications) and ARCAM Ti6Al4V ELI has been used is a gas atomized prealloyed powder having particles in a size range of 45-100μm [132]. The material properties of EBM printed ARCAM Ti6Al4V ELI is provided by the supplier; Young's modulus, yield stress, ultimate tensile strength, and elongation were given as 120 GPa, 930 MPa, 970 MPa and 16%, respectively [132]. The chemical content of the ARCAM Ti6Al4V ELI can be seen in Table 5.1.

Table 5.1 : Chemical specifications of Arcam Ti6Al4V ELI.

Al	V	C	Fe	O	Ni	H	Ti
6.0%	4.0%	0.03%	0.10%	0.10%	0.01%	<0.003%	Balance

ELI stands for extra low interstitial which means a reduced level of oxygen, nitrogen, carbon, and iron. Especially, oxygen content plays an important role in the mechanical performance of the EBM printed Ti6Al4V parts. The oxygen content of the powder should not exceed the maximum value of 0.2% required for Ti6Al4V. The case of higher oxygen content can be associated with the stocking, handling and recycling of the powder [133]. In addition, after completion of production in EBM, powder cake is extracted the out of the build chamber and replaced to the powder recovery station. The same type of powder is thrown with sandblasting gun to remove the powder around the produced parts, and removed powders are accumulated in the hopper to use them in sandblasting and in new production. These leftover powder can be reused after the sieving process.

5.2 Material Classification and Tests

The thermal gradient is one of the important variables for the metallic additive manufacturing due to high production temperatures. The thermal gradient can differ

according to the point of the building chamber. So for understanding the effect of production zone in the building chamber, it is divided into two regions and two levels (Figure 5.2), and specimens from those parts were tested and compared according to ASTM E8E8M - 16a. Furthermore, it is known that EBM productions show anisotropic behaviour so three different production orientation (0, 45, 90) were selected as build orientations. All the variables for the EBM printing subjected to this study can be seen in Table 5.2. 0^o is defined as an axis which is perpendicular to the building chamber ground in other words perpendicular to the direction of powder distribution plane. It must be noted that the surface of the tensile specimens was polished to remove loose powder particles and discontinuity on the surface as seen in the images of the fractured specimens in Figure 5.6-5.11.

Table 5.2 : EBM production variables.

Regions	Level	Orientation
Top and Bottom	1 and 2	0^o, 45^o and 45^o

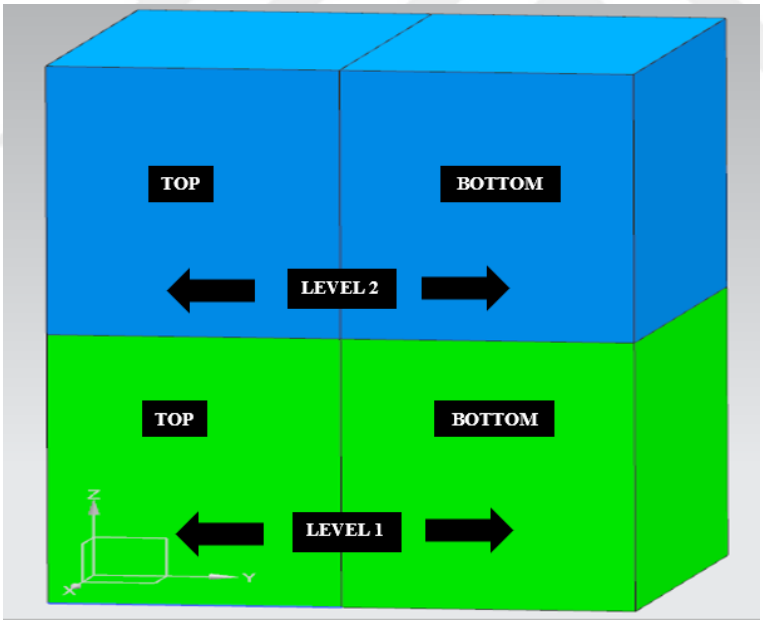

Figure 5.2 : EBM building chamber zones.

In the tests, MTS 810 Material Test System (250 max payload) is used with MTS 647 Hydraulic Wedge Grip, and MTS 634.31F-24 extensometer was used in the tensile tests as seen in Figure 5.3.

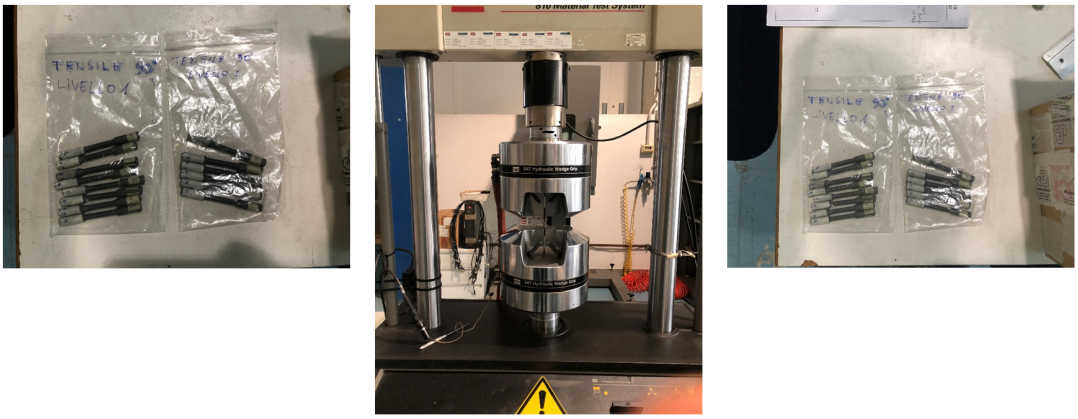

Figure 5.3 : Tensile specimens and MTS 810 material test system.

As a result of tensile tests, it is understood that level and chamber location do not affect the mechanical specifications of tensile specimens significantly. However, the build orientation has a crucial effect, especially considering breaking strain (strain at break). Young's modulus, yield stress, ultimate tensile stress, fracture stress and breaking strain in comparison with different three production orientations are given in Figure 5.4. It is concluded that from Figure 5.4 different production orientations do not make considerable effects in the elastic region, however, in the plastic region, production direction is a dominating factor.

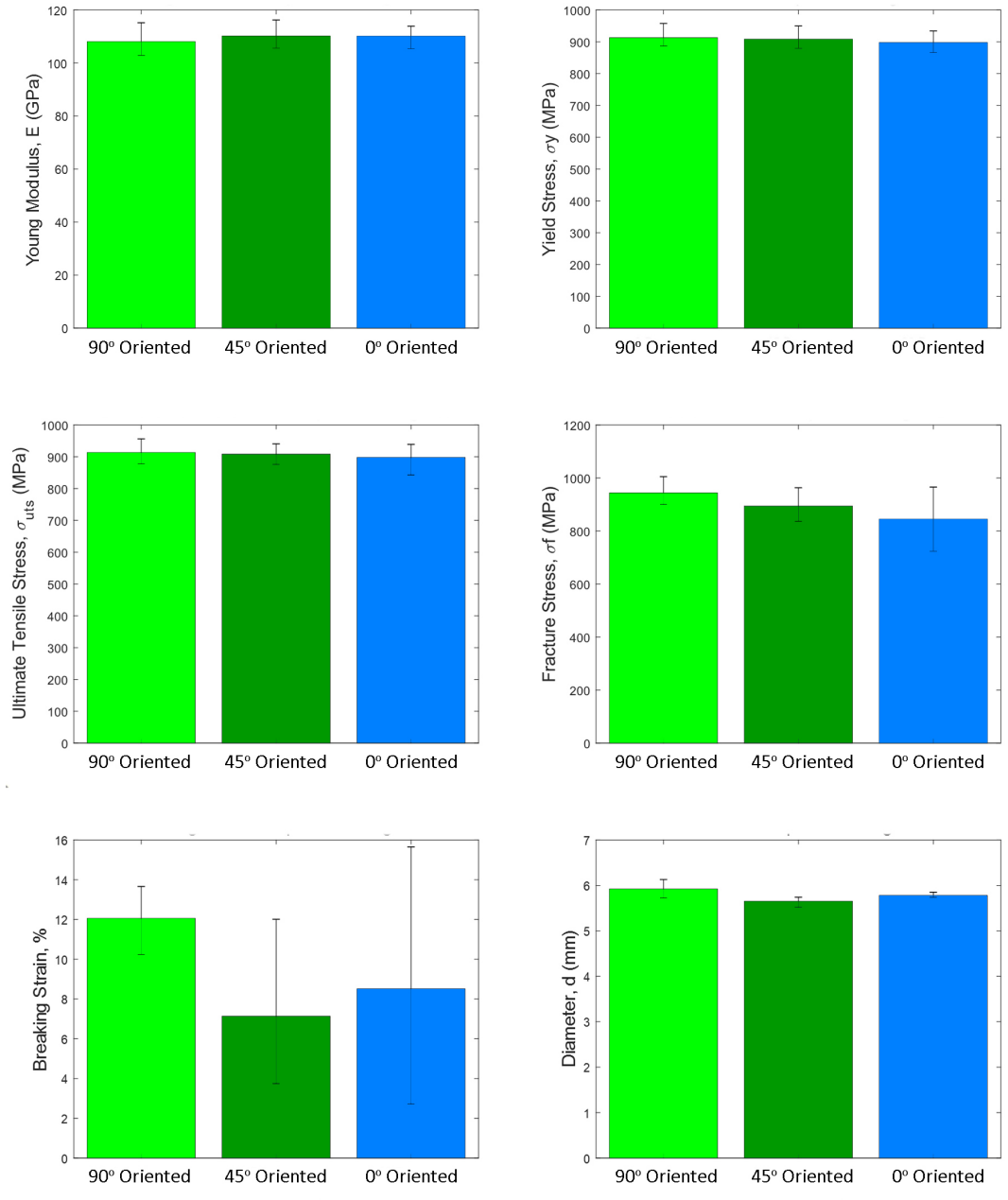

Figure 5.4 : Mechanical specifications versus production angles.

Totally 48 tensile tests were conducted for investigating the effect of build orientation on the mechanical performance. 17 of the specimens were produced and tested for every 90-degree orientation and 16 specimens for 45-degree orientation and 14 specimens for 0-degree orientation. The stress-strain graphs are given in Figure 5.5 for 0, 45 and 90-degree production orientations, and as seen in the graphs, 0 and 45 production degrees can cause catastrophic failures with inconsistent breaking strain values, however in the 90-direction production stress-strain curves are consistent. Besides, SEM is used to understand the inconsistent behaviour and low breaking strain,

For investigating the failure zones and mechanical specifications of the highest and lowest breaking strain experiencing specimens, their SEM images of failure zones, failed parts, mechanical specifications, variance values and stress-strain curves are given in Figure 5.8-5.11.

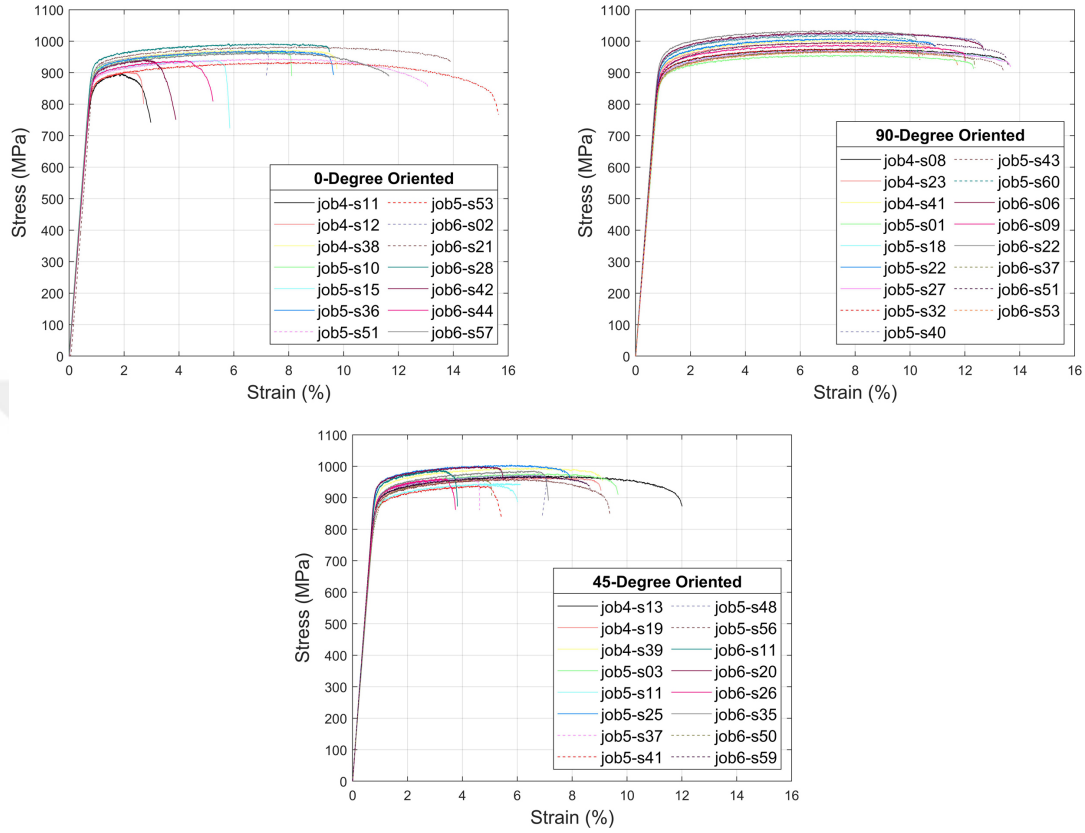

Figure 5.5 : Stress – Strain graphs for 0, 45 and 90 production degrees.

After the investigation of two SEM images in Figure 5.6 and 5.7, it was observed that there are some discontinuous regions in the second Figure 5.7 which showed the highest breaking strain in the 90-degree oriented specimens. These discontinuities can be seen as black speckles which are distributed in the cross-section of specimen. However, in the first Figure 5.6 which showed the least breaking strain among 90-degree oriented specimens, unmelted complete powder particles close to edges can be observed in the cross-section. The variance for both specimens in the breaking strain is almost close and has opposite values. Moreover, the difference in Young's modulus, yield stress and ultimate stress are in the negligible range. The difference in the fracture stress is also bound with the breaking strain, and the difference in breaking strain is 32%. The vast important case that is needed to be considered is the support structure leftovers on the surface of the 90^{o} oriented specimens in a shape of the line

and degraded surface patterns caused by removal process of support structures. These cases can be the reason of surface discontinuity, and therefore stress concentrations can be provoked in these regions due to loading. So it is hard to come through the direct result without diminishing their effect. Furthermore, these support structures are almost compulsory to abstain from the production defects like wrapping syndrome which is caused by the high thermal gradients. Using support structures in the EBM production is unlike the SLM process; in SLM process support structures are needed to prevent collapse during the production and preventing high heat gradients. However, as it is mentioned before, floating parts can be produced in the EBM methods so support structures are to be used to distribute the heat and restrain the high thermal gradients. Additionally, it is seen that the deformed tensile specimens lateral images show that geometrical accuracy problems in Figure 5.6 and 5.7 which are caused by the production orientation. Due to the gravity, melt pools have a tendency to flow in the perpendicular direction to power distribution direction if enough support structures are not exploited to consolidate parts itself. In this case, enough support structures covering the below surface of the tensile specimens was not used. Therefore, the roundness was degraded during the production. This problem also can be seen in 45^{o} oriented specimens as a slight roundness degradation problem, however, 90^{o} showed best geometrical accuracy and clear-cut roundness.

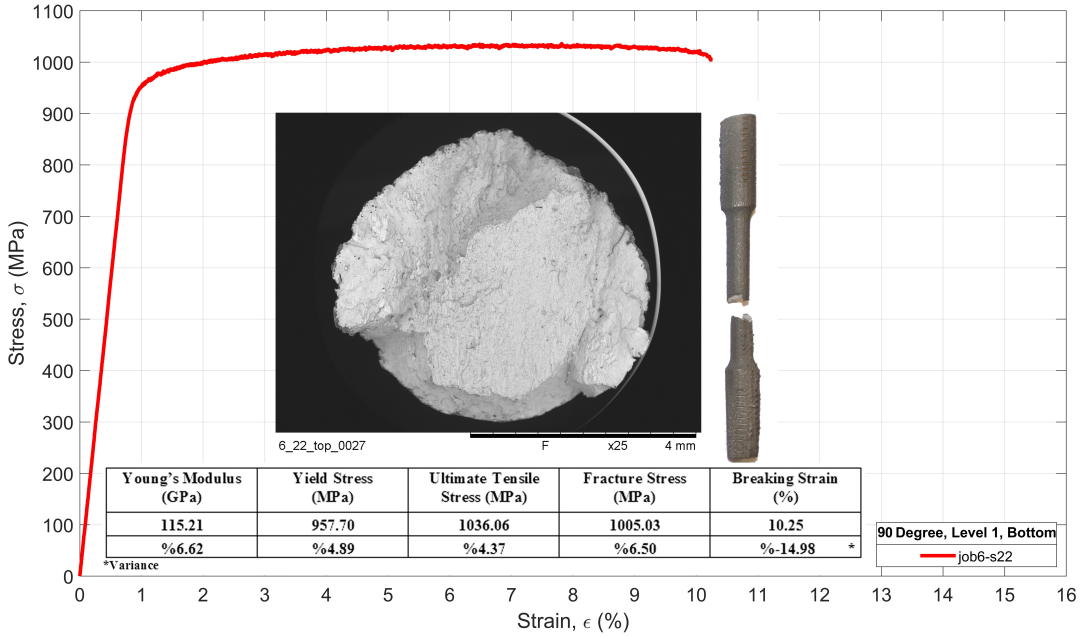

Figure 5.6 : 90-degree production with lowest breaking strain.

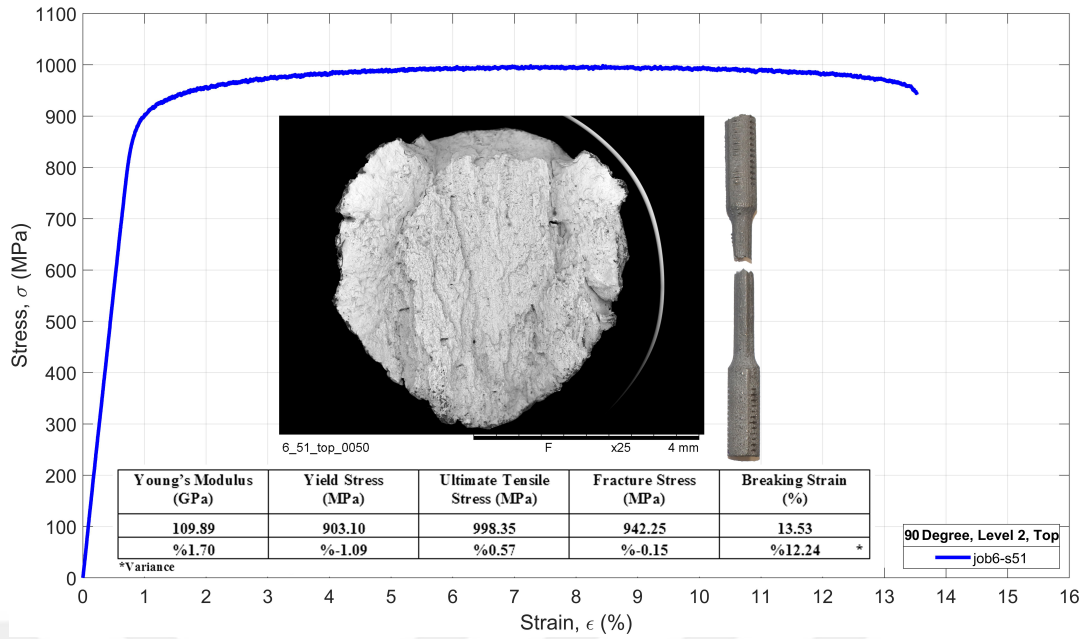

Figure 5.7 : 90-degree production with highest breaking strain.

After the investigation of two SEM images in Figure 5.8 and 5.9, it was observed that there are some relatively small shiny regions in the middle of cross-section so-called lack of fusion in Figure 5.9. The specimen in Figure 5.9 which shows the highest breaking strain, all mechanical specifications seems close to mean values. However, breaking strain values is rather diverse with a 68.46% difference than the mean value. Moreover, premature failure is observed in Figure 5.8 with breaking strain value of 3.75%. It is seen that there are a completely unfused bundle of accumulated powder particles exist in the middle of the cross-section and semi-fused regions are prevalent. This large portion of discontinuities is the cause for premature failure. The mechanical specifications of Young's modulus, yield stress and ultimate stress of both specimens are in the close range with mean values.

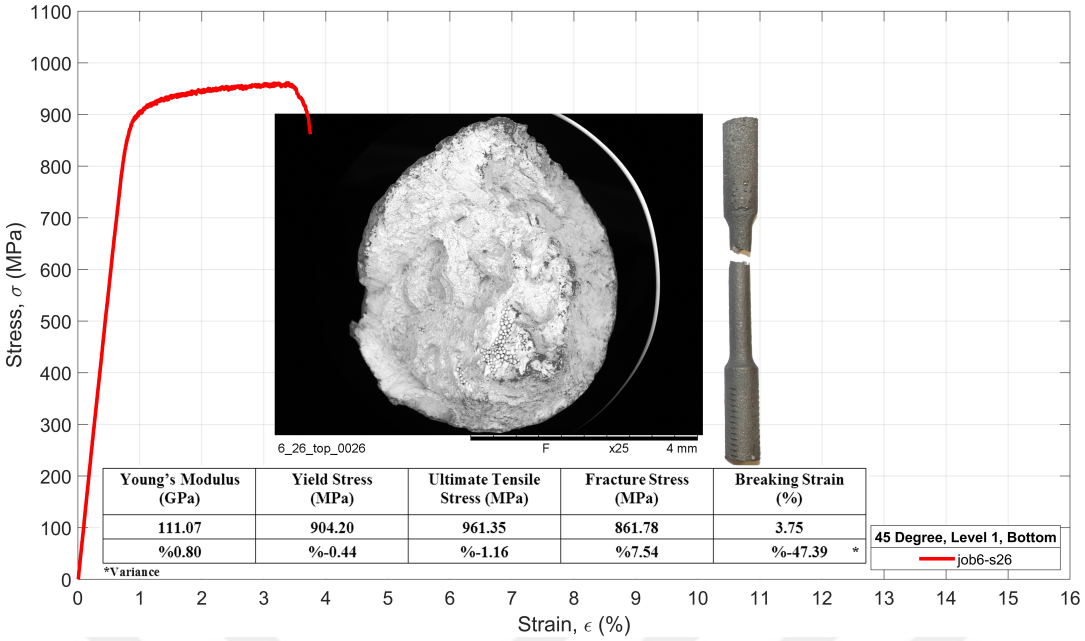

Figure 5.8 : 45-degree production with lowest breaking strain.

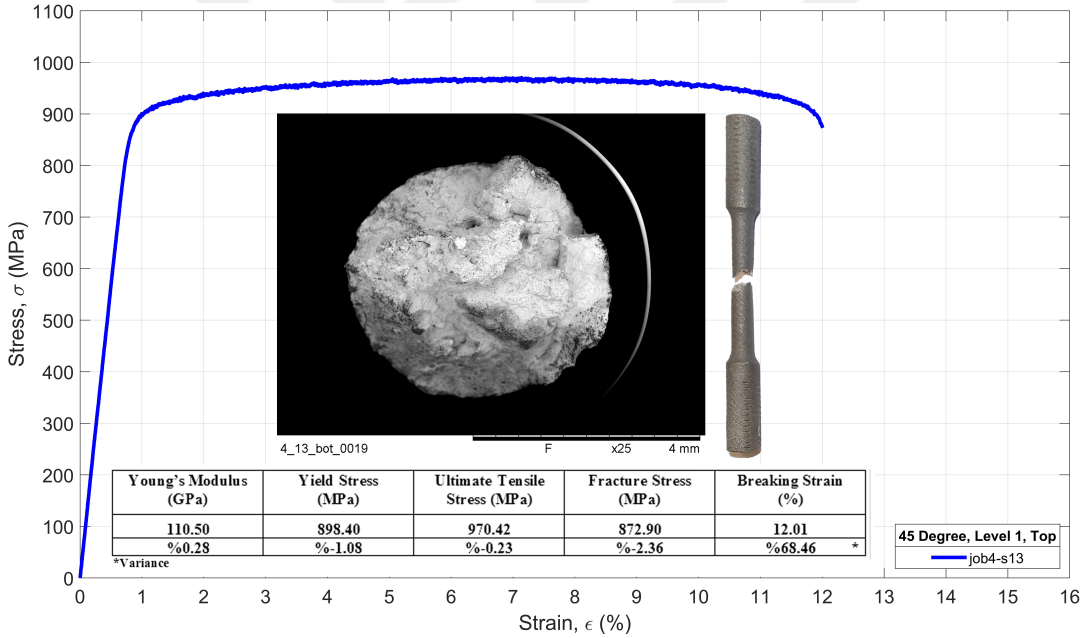

Figure 5.9 : 45-degree production with highest breaking strain.

After the investigation of two SEM images in Figure 5.10 and 5.11, where the specimens were produced perpendicular to the powder distribution direction, it was observed that premature failure exists in Figure 5.10. It can be seen semi-fused regions and unfused powder particles are accumulated in the centre of the cross-section with a large portion nearly covering 1/3 of image. However, excluding breaking strain, other mechanical specification values seem in the feasible range. Breaking strain was

68.14% different from the mean value. However, as can be seen in Figure 5.11, lower amount of black speckles and lack of fusion defects can be observed.

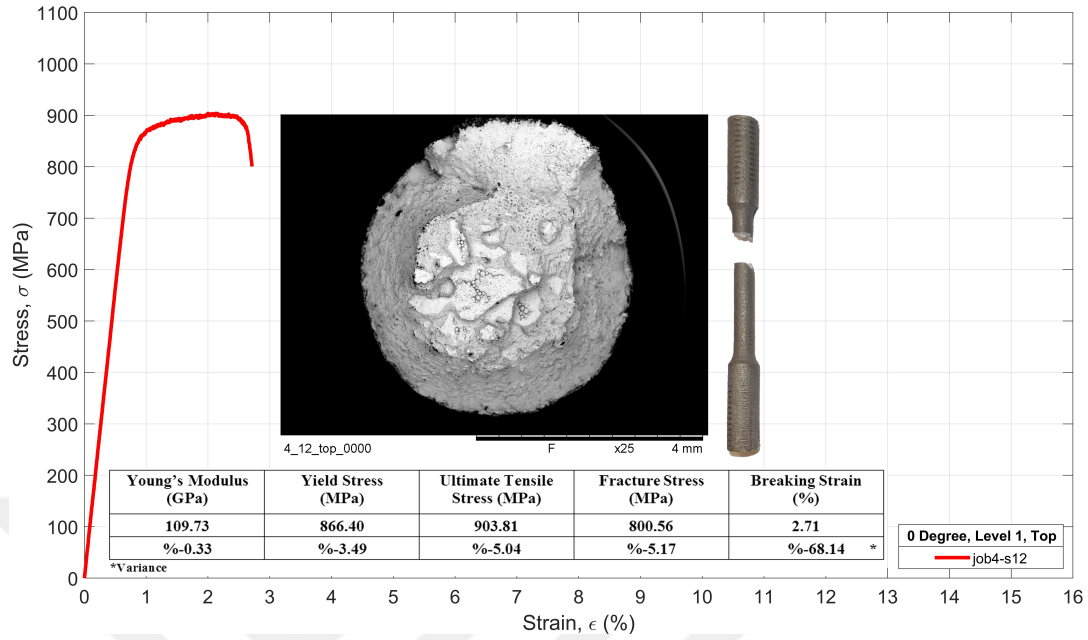

Figure 5.10 : 0-degree production with lowest breaking strain.

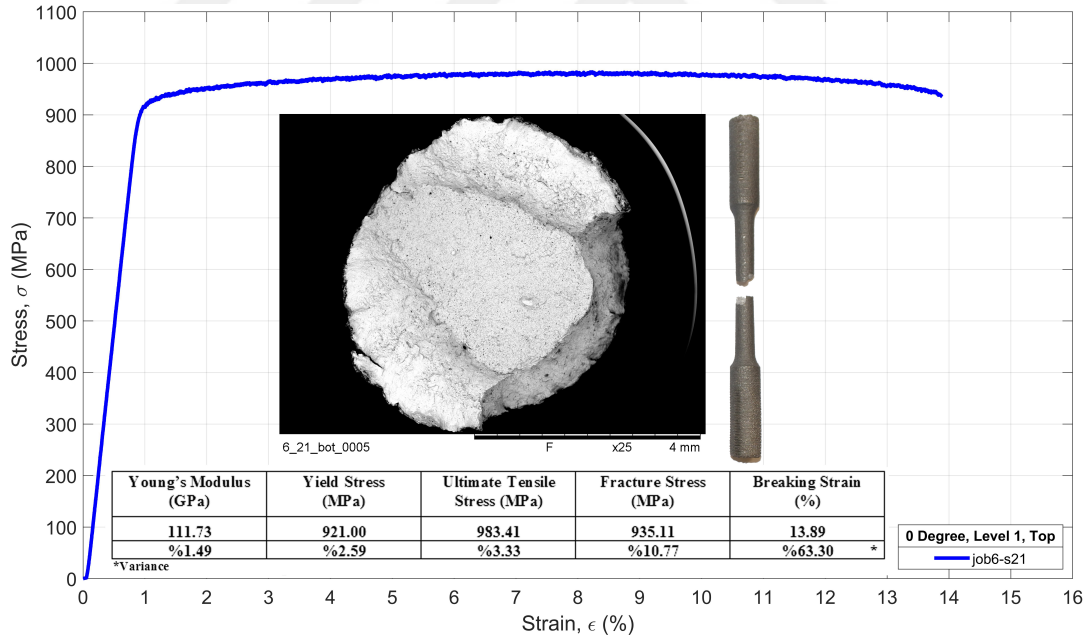

Figure 5.11 : 0-degree production with highest breaking strain.

After the investigation all of the SEM images and stress-strain graphs for highest and lowest breaking strain experienced 0,45 and 90^{o} oriented production test results, it was observed that there are some bundle of completely unfused accumulated Ti6Al4V particles, black speckles and semi-melted regions which affect the breaking strain of specimens. As an important output of this section, it is seen that the 0^{o}, 45^{o} and

90^o oriented produced specimens having highest breaking strain have an insignificant amount of defects, and these specimens experienced similar and consistent mechanical performance. Thus, it can be said that anisotropic material behaviour for EBM printed Ti6Al4V ELI is caused dominantly by the defects. Additionally, a well-rounded explanation about defects is given in Section 5.2.1.

5.2.1 Lack of Fusion

Regardless of the fact that additive manufacturing is a mature technology for metal printing, this manufacturing technology still has chronic production problems are needed to be overcome. The integrity and robustness of the additively manufactured parts are based on the fusion bonding of the consecutive hatches and layers [134, 135]. Excluding dimensional accuracy, the most important point that must be considered according to the quality of the produced parts is the existence of internal defects [136]. These defects are the key factors for implementing additive manufacturing methods with fewer problems. The major problem can be mentioned as the limited control of discontinuities or porosities in the produced components, and these problems can be the reason of the produced part rejection depending on the internal defect severity. It is known that the porosities can create vital problems in the produced part when the component undergoes large deformation and repetitive mechanical loads.

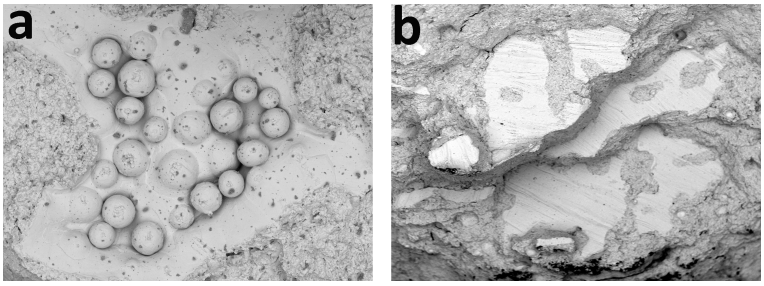

Figure 5.12 : Lack of fusion a) unfused complete powder particles b)semi-fused zones.

There are several sorts of porosity creating mechanisms that arises during the production and can be listed as gas pores, lack of fusion, balling and cracking [136, 137]. However, lack of fusion (LOF) is the most significant one among them that impacts majorly the mechanical properties of final part due to incomplete weld of the current melt to the surrounding part. In other words, the exact definition of the lack of fusion can be put forward as the incompletely fused spots; it can be

observed as complete powder particles (Figure 5.12a) or semi-fused powder (Figure 5.12b). Moreover, in fracture surfaces both complete powder particles in one side and semi-fused zone in other side can be observed as seen in Figure 5.13. The main reason why LOF is to be considered as an important production problem is the size and irregular shape of porosities which can act as a crack initiator [39, 138]. The porosities that are caused by the entrapped gas pores (keyhole effect) in the additively manufactured parts can be 9.9 μm for EBM and 5-20 μm for SLM, however, pores formed by LOF can be in the range of 50 to 500 μm [139, 140]. Moreover, the location of the porosity is also another important issue which can even cause premature failures. Consequently, for obtaining better mechanical performance for additively manufactured components it is essential to have limited internal discontinuities [141].

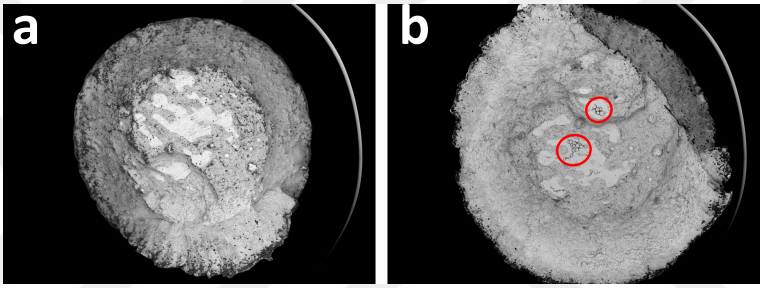

Figure 5.13 : Failure surface of a) below part (fixed) and b) above part (pulled).

LOF is primarily dominated by the insufficient melting of the powder, and it is directly relevant with the production parameter of spot diameter and energy density. The spot diameter in EBM is regulated by magnetic coils which concentrate and adjust the diameter and position of the beam and prevent astigmatism, and special algorithms are used to tune them. The problem in the focus of the beam can cause negative and positive defocus problems. The negative defocus can be descried as the laser focus point on the previously produced layers which causes keyhole effect problems, and positive defocus is the focus of beam above the intended point is the one of the cause of LOF [142]. As for energy density(E), it is controlled by the laser power (P), scanning velocity (v), hatch spacing (w) and layer thickness (h). The equation of energy density is given in Equation 5.1.

$$E = \frac{p}{vwh} \tag{5.1}$$

The keyhole effect is caused by the high energy density (high power and low speed), and LOF happens at lower energy density (less power and high speed) [143]. However, there is no certain methods that direct engineers to totally eliminate defects. Because build themes are differentiated for different AM methods, layer thickness, powder material and scanning strategy. In addition, another important issue which has not generally drawn enough attention, is that the scanning strategy must be taken into account for LOF. In the scanning strategy, a laser or beam tracks a particular pattern in every layer to weld each layer to previous layer and tracks to adjacent tracks. During this welding process, a track must be overlapped properly with the next track to avoid LOF.

As it is known, it is very hard to avoid internal defects, and after production some tests is to be performed to check the severity of defects. For defect detection non-destructive inspection techniques can be utilized in some cases to define the defects and quantity. The commonly used easy NDI post-process technique is based on the Archimedes principles (Archimedes balance) to be employed in the measurement of the density of produced parts, and by comparing the density of the base material the amount of porosities can be determined. Furthermore, sophisticated technique, CT scanning of the parts can be useful to detect the severity of defects by defining their shape and position in some cases [136]. The disadvantage of these techniques can be listed as increased lead times and additional costs. Furthermore, density measurement techniques is not sensitive to detect the location of porosities and most importantly is not sensitive to the low number of porosities which can be in large-scales. Regarding CT scans, they are very costly NDI techniques and limited in the part size. Additionally, the resolution of the CT scan is directly relevant with the defect [144].

5.2.1.1 Effect of lack of fusion on mechanical performance

It is important to notice that the severity of internal defects and surface discontinuities influence the mechanical specification of additively manufactured parts according to the loading direction. Furthermore, lack of fusion problems are significant problems that is hard to abstain from them. So that effect of the lack of fusion to the mechanical specification must be understood well to define build orientation according to it [145].

In the previous section, black speckles were observed in the breakage cross-section of the 45° and 90° oriented specimens. These black speckles are the gaps in the material which are caused by the lack of fusion. Research have shown that additively produced part having lack of fusion problems in the 0° direction (Figure 5.14-a) , unfused powder particles and semifused regions can be seen, however, if same defects are seen in the 90° direction (Figure 5.14-b), these defects can be seen as black speckles (inner gaps). In the 45° direction, it is prevalent to see both of them. While performing a tensile test in the direction of 90°, lack of fusion defects tend to close with the increasing load (Figure 5.14-d), however, in the 0° direction gaps due to lack of fusion problems tend to opens (Figure 5.14-c) and acts like a stress concentration points and crack initiators which cause a early failure of component.

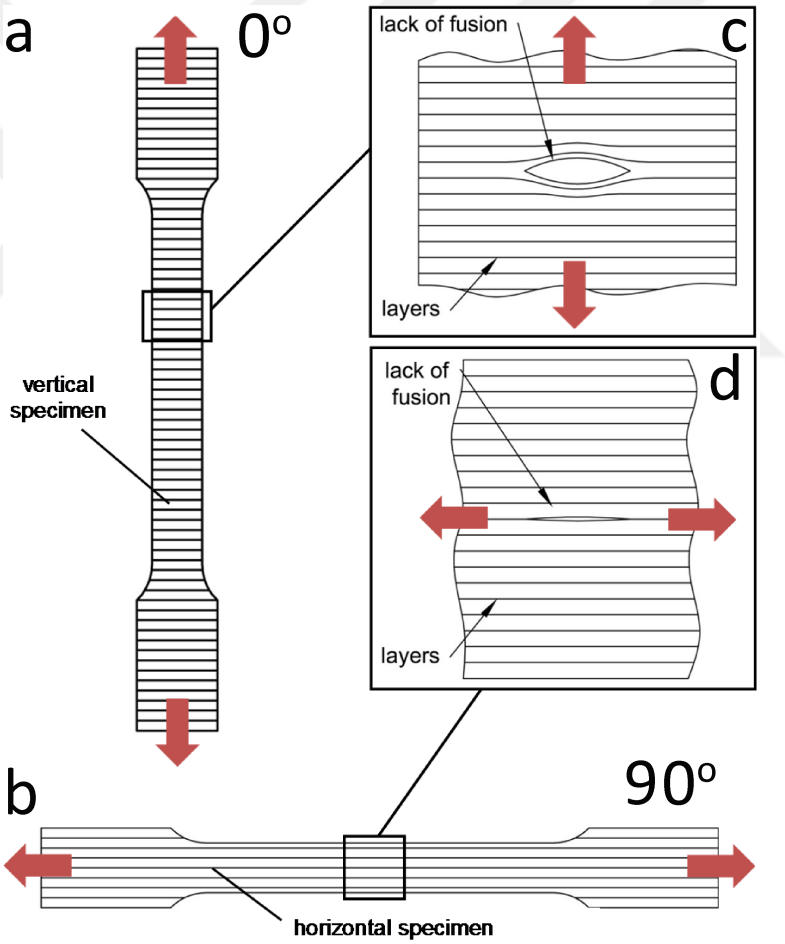

Figure 5.14 : Influence of the direction of loading on the severity of a lack of fusion [145].

5.3 Effects of LOF Area to Mechanical Performance

Especially, LOF sections can be clearly seen in the 0^o oriented specimens as it is mentioned in the previous section. In this section, the LOF area of the 0^o oriented specimens are given in the relation with Young's modulus, yield stress, ultimate stress, fracture stress and breaking strain. Instead of defect area as a comparison variable, the ratio of defect area to total cross-section area is used because of the different cross-section areas of the different tensile specimens. The aim is determining the effect of LOF areas to the mechanical performance. In Figure 5.15, the effect of defect area ratio to Young's modulus can be seen and in this graph no pattern was captured due to fluctuating behaviour. However, in Figure 5.16, where the effect of defect area ratio to yield stress is presented, the general behaviour of the curve is that the yield stress decreases by increasing the defect area ratio. Furthermore, Figure 5.17 depicts the relationship between the defect area ratio to ultimate strength and fracture strength. In this graph, ultimate strength and fracture strength curves present similar behaviours with a decreasing trend. However, the effect of defect ratio is greater for fracture strength than ultimate tensile strength. As to breaking strain (Figure 5.18), significantly, graphs shows an almost linear trend in increasing defect ratio to breaking strain. It can be said that mechanical performance in terms of Young's modulus, yield stress, ultimate tensile strength and fracture strength respect to defect area ratio shows similar patterns as can be seen in Figure 5.15, 5.16 and 5.17. As the study is narrowed down to the specimens defect patterns, a particular behaviour is seen in Spec_5_53. Even if it has the lowest defect ratio, it experiences low Young's modulus, yield stress, ultimate tensile strength and fracture strength. Also, similar behaviour can be observed for Spec_5_51. The common points of both specimens are having same defect pattern; one large round shaped complete defect close to center of cross-section which caused a premature failure. It can be concluded that this type of defects do not act like a crack initiator but it causes discontinuity region in the cross-section without causing any premature failure. This is also the explanation of the Spec_5_53 and Spec_5_51 experienced less mechanical performance and high breaking strain.

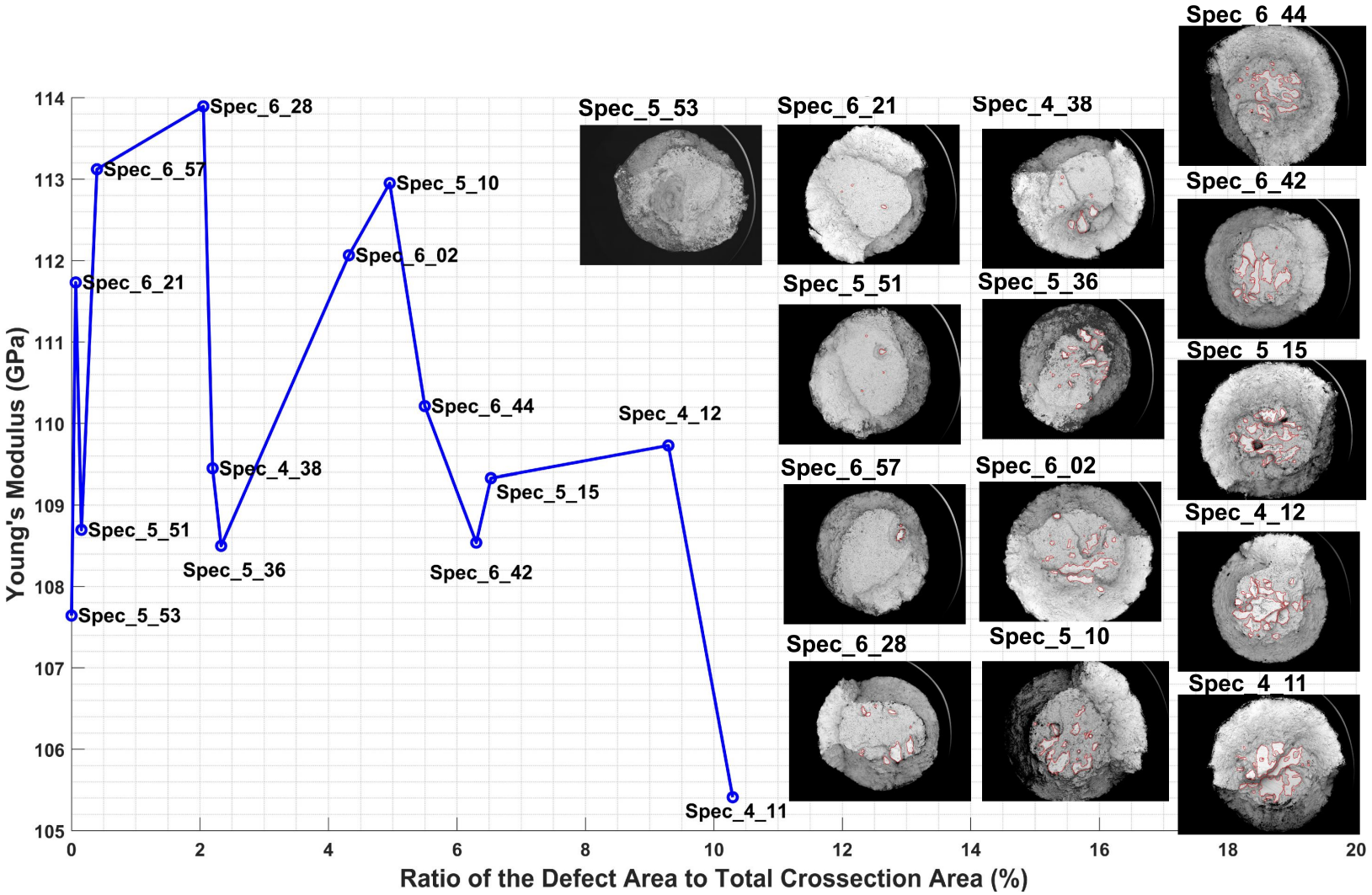

Figure 5.15 : The effect of defect area ratio to Young's modulus.

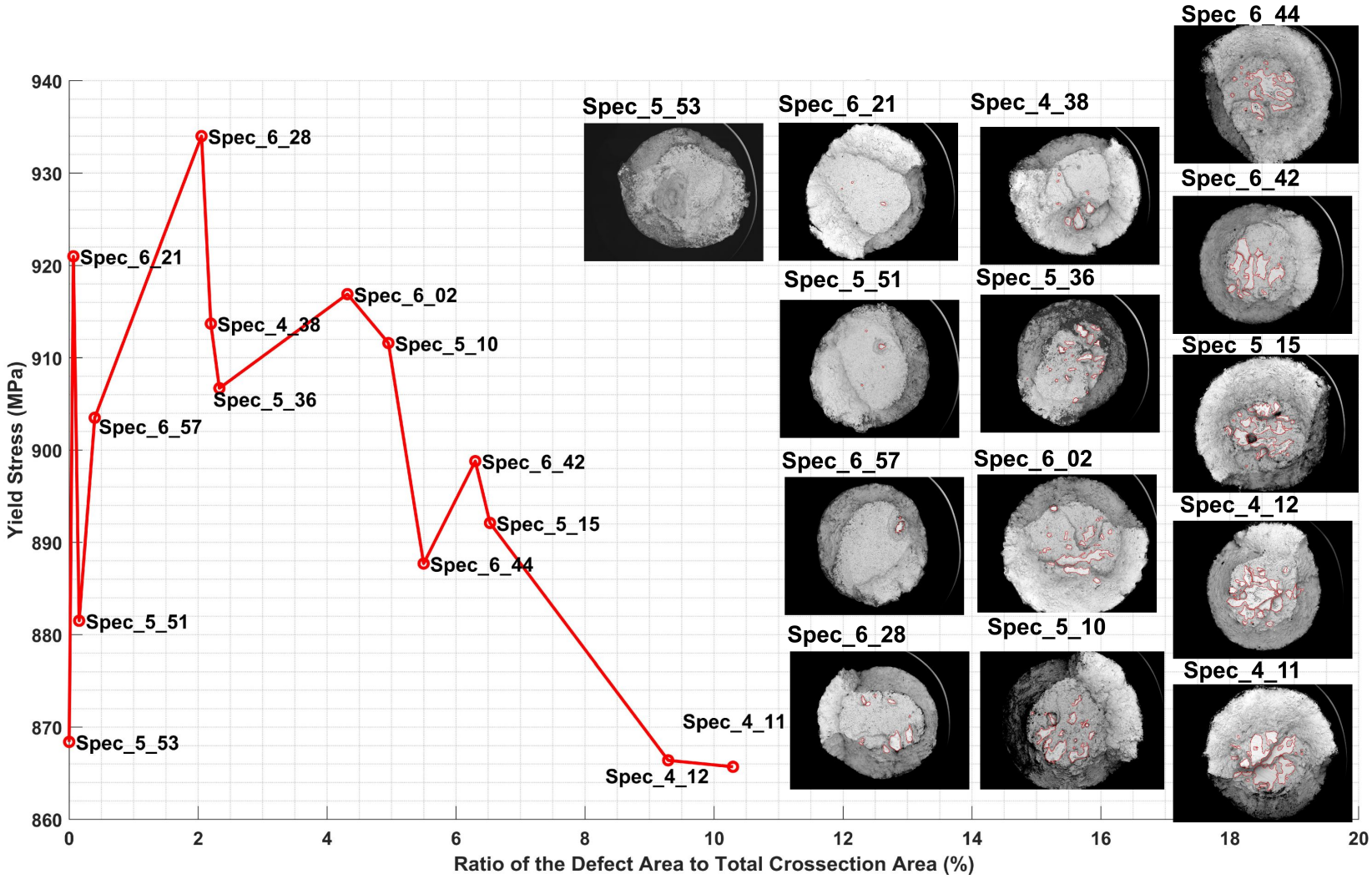

Figure 5.16 : The effect of defect area ratio to yield stress.

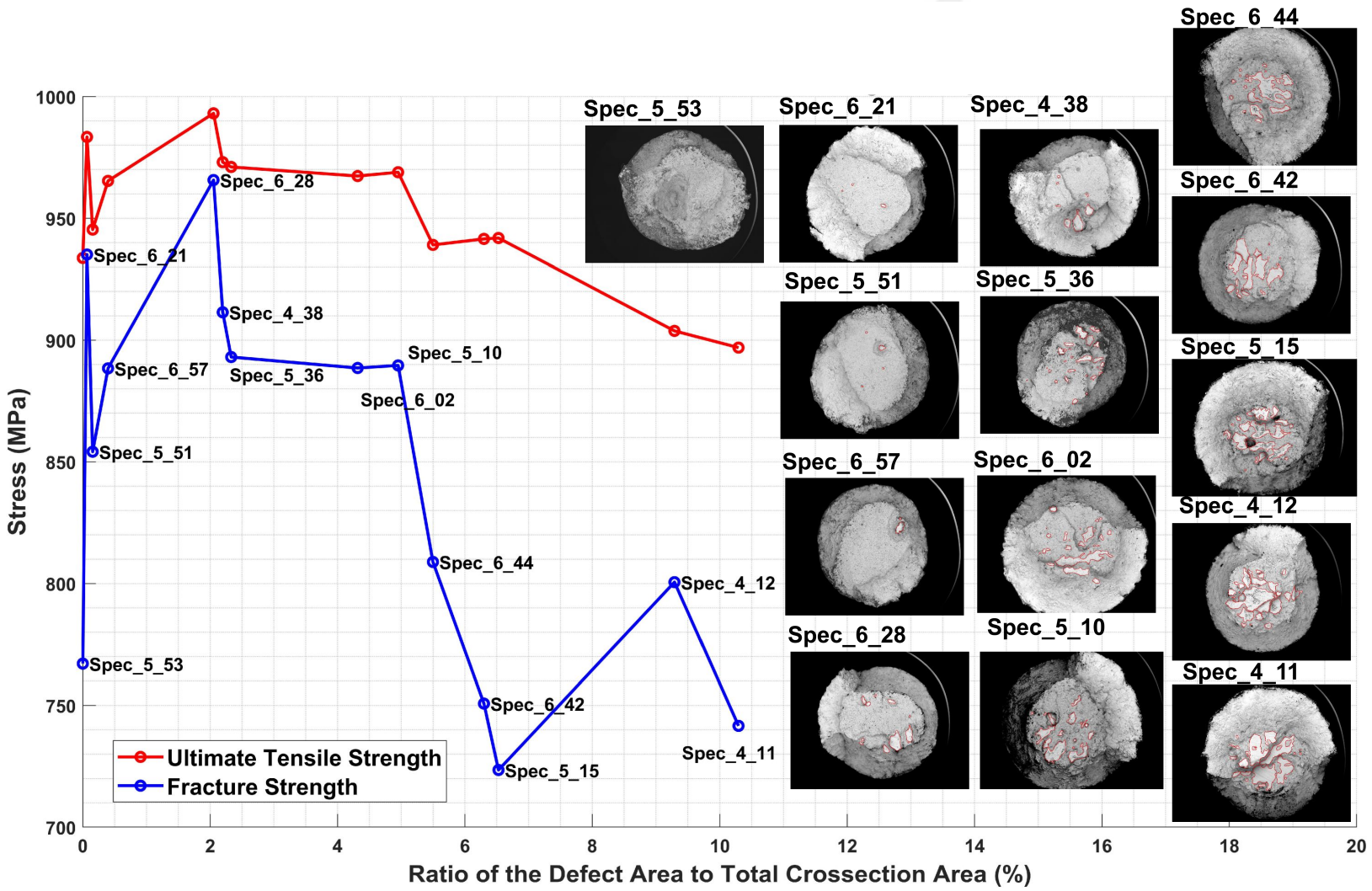

Figure 5.17 : The effect of defect area ratio to ultimate strength and fracture strength.

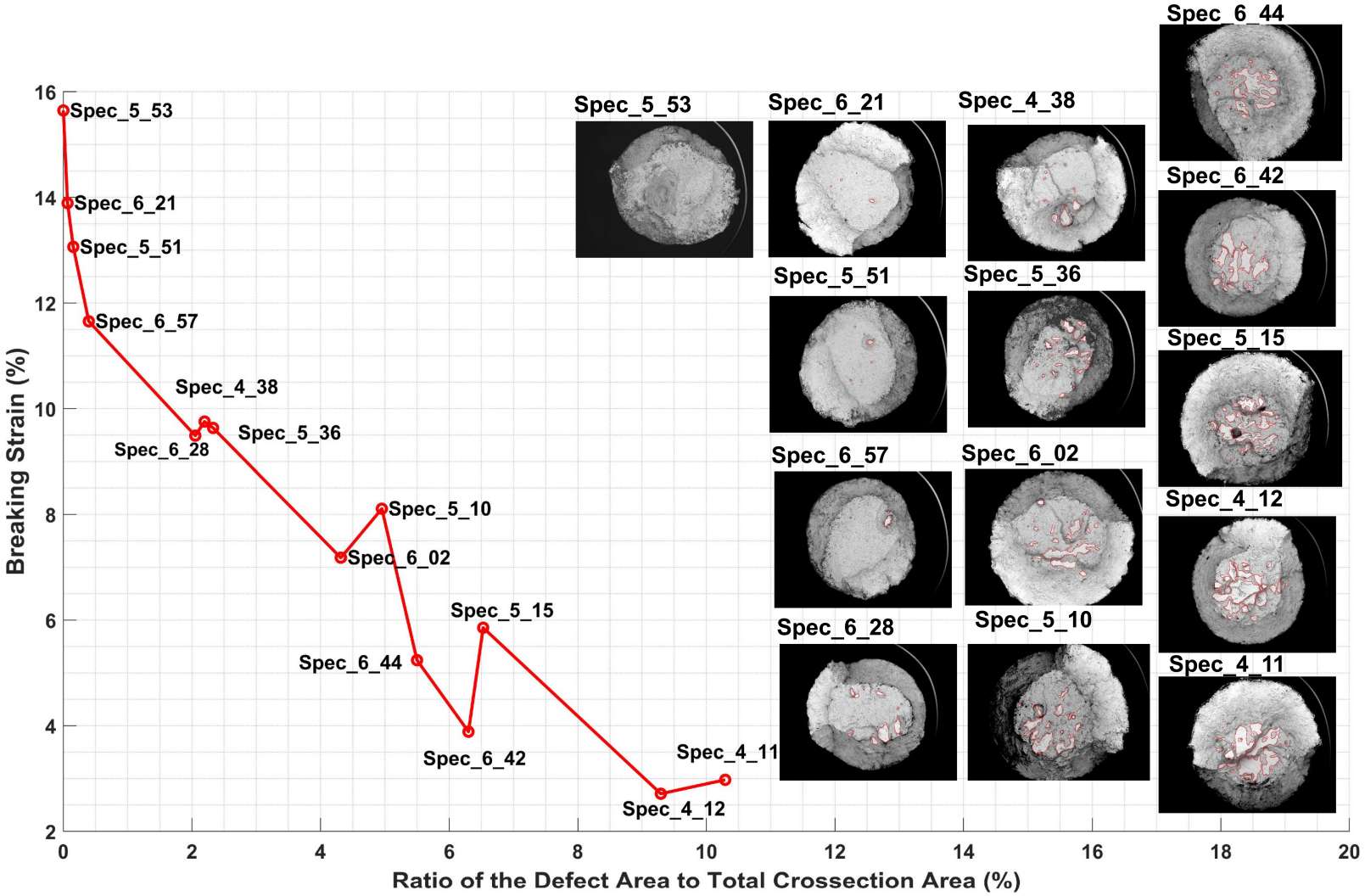

Figure 5.18 : The effect of defect area ratio to breaking strain.

5.3.1 Constitutive equation

As a result of tensile tests in different orientations to understand the material behaviour, a material model is to be selected to simulate the material behaviour in FEM analysis. Linear elasticity and classical plasticity material models are described in this section to cover the material behaviour in these models in conjunction with the test results. A linear elasticity material model is a legitimate material model for the models that shows small elastic strains are normally less than 5%. In this model, isotropic, orthotropic or anisotropic material behaviours can be captured. True stress and strain values are used in this model. In other words, it can be briefly expressed that Cauchy stress and logarithmic strain are employed in finite-strain problems. The elastic properties for the constitutive equation in this model can be totally expressed using Young's modulus (E) and Poisson's ratio (ν). Shear modulus is also needed, and it can be calculated using G=E/2(1+ν). Another important criterion that must be considered is the stability criterion. According to this criterion, E and G must greater than zero, and Poisson's ratio can be in the range of -1 to 0.5. This also means it is allowed that the NPR base material can be elastically modelled with this model. Poisson's ratio values that approaches 0.5 results in almost incompressible material behaviour. In this case, hybrid elements are suggested. This material model can be employed in implicit and explicit analysis with any elements that have displacement degrees of freedom.

For the simulation of the plastic behaviour classical metal plasticity material model can be used in conjunction with linear elasticity material model. Classical metal plasticity model is used in order to simulate the material behaviour for general collapse studies, metal forming and crash analysis. This model includes several material behaviour cases like isotropic yield (Misses criterion), anisotropic yield (Hill's yield surface), perfect plasticity, isotropic hardening, rate dependency, progressive damage and failure, and shear failure. Progressive damage and failure models can be employed using different damage evolution laws and damage initiation criteria which are based on the degradation of the stiffness matrix and removal of the elements. It is a mesh dependent failure method which removes the mesh elements according to the degradation. Mises yield surface can be defined using a uniaxial yield stress value because it is a function of uniaxial equivalent plastic strain, however, Hill

yield surface needs uniaxial yield stress and its ratio to other yield stresses in other directions. Furthermore, hardening can be defined using isotropic hardening. In the case of no hardening is considered perfect plasticity is employed where it is a constant stress in the circumstances of changing strain value. Furthermore, isotropic hardening can be defined by the uniform change of yield stress locus; it can increase or decrease according to material behaviour. In ABAQUS, isotropic hardening is utilized as a tubular function of stress and plastic strain. Also, associated plastic flow is used for elastoplastic material behaviour simulation. In the plastic flow, Poisson's ratio is considered as 0.5 which means incompressible material (no volume change) deformation rate in the direction where it is normal to the yield surface. As another aspect, rate dependency is an important issue due to the increase in the rate dependency causes an increase in the yield stress for most of the materials. Classical metal plasticity is alike linear elasticity model for element selection, any elements having displacement degrees of freedom can be used with this model.

EBM printed Ti6Al4V ELI components shows isotropic elasticity and isotropic yield stress so linear elastic behaviour model and classical material plasticity model can be deployed for this material to simulate its behaviour during monotonic or low cycle loading. However, strain at break values for EBM printed Ti6Al4V ELI material varies according to the building direction. This can be explained by the effect of LOF. So that damage laws can be included in the simulation to have better results. Extended finite element method (XFEM) can be used for modelling discontinuities like LOF if the location of discontinuities is well known. However, XFEM can be used only for the ABAQUS/Implicit, and it has some difficulties for convergence issues. For ABAQUS explicit, ductile damage modelling can be used for element deletion and modelling discontinuities. However, if the uniaxial loading direction is known before the production, production orientation can be adjusted on the direction of 90^{o}, and 90^{o} oriented specimen tensile results can be used for the constitutive equation. As a result, according to the tensile test results, a constitutive equation is selected, calibrated and adapted in a tubular form to represent the behaviour of the material.

5.4 Chiral Auxetic Cell Production, Tests and Analyses

5.4.1 Introduction

The structural chiral auxetic honeycomb concept was initially proposed by Prall and Lakes, and the Poisson's ratio value of -1 was proven in a theoretical way based on standard beam theory in their study [146]. Due to its non-centrosymmetric topology, chiral cellular solids exhibit anisotropic behaviour, and auxeticity occurs in the direction of edgewise (in-plane), the literature review can be divided into two classes which are edgewise and flat (out-of-plane) studies. Spadoni et al. [147] investigated global linear buckling behaviour numerically on the flatwise direction, FEM model was used in this study with classical theoretical equations for buckling of shells and thin plates considering the possible formation of localized plasticity. Lorato et al. [55] developed analytical and FEM models to calculate flatwise Young 's modulus and shear stiffness of trichiral, tetrachiral and hexachiral lattice configurations, and the models are validated with the experimental results. A flatwise compression study was conducted by Airoldi et al. [148] to investigate buckling and post-buckling behaviour, and a specific technology was used to produce composite chiral unit structures to obtain specific energy absorption level of chamfered chiral structures. Also, some edgewise studies have been conducted, one of which involves a mathematical model using dynamic shape functions to explain dynamic behaviour over a broad frequency range [149], and additionally several studies conducted on wave propagation characterization of chiral structures [150–152]. Chiral structures can maintain their auxeticity under large overall displacement within the elastic deformation limits, however, when they are subjected to large deformation causing plastic deformation, the auxeticity of chiral structure disappears. Zhu et al. [153] used wavy ligaments in their study to increase the auxeticity limit of chiral cells for large elastoplastic deformation, and as a result, the new structure experienced better performance. Another auxeticity study was conducted by Alderson et al. [36] to explain the elastic properties and auxetic behaviour of different chiral cells having 3, 4 and 6 ligaments connected to one node. Also, homogenization studies were conducted for chiral lattices to obtain computationally low-cost models [37, 154, 155], and alternatively, chiral lattice cells were suggested as

filling material for morphing structures because of their potential to endure significant actual displacements [147, 156–159].

EBM AM technology is utilized in this study to produce three-point flexural and tensile samples and unit lattice cells of the chiral auxetic structures. EBM is deployed to consider the mechanical properties impact of the production method. All bending and tensile specimens were produced in two different thickness of 0.8 and 1.6 mm and orientations of parallel (90^o) and perpendicular (0^o) to the building plate of the EBM machine. Chiral lattice unit cells are manufactured where their flat-sided surface is parallel to the plane of powder deposition to achieve higher mechanical efficiency and avoid the use of internal support structures. Two different thicknesses are employed for chiral structures to characterize the effect of thickness of chiral cell to auxeticity and stiffness. Also, the compressive load profile is applied to chiral structures to monitor their Poisson's ratio variation under different deformation limits. Additionally, chiral unit cells was crushed to investigate their energy absorption. As a consequence, a low cyclic compressive displacement and crush load are adopted to the chiral unit cells, and ABAQUS/Standard is used to conduct validation studies for low cyclic chiral structure deformation and bending tests.

5.4.2 Material and processing

Whenever produced parts are extracted from the powder cake and cleaned, loose leftover powder particles can take place on the surface, and they should be removed to take sensitive dimensional measurements. To reduce surface roughness and remove the loose particles sandblasting is applied in this study. Sandblasting is applied 5 seconds each surface of the specimens, and surface roughness are measured before and after sandblasting. The powder cake, as-built and sandblasted chiral structures and tensile specimens are seen in Figure 5.19, sandblasted parts are in dull colour. Additionally, to define the effective cross-section area of the tensile and bending specimens where the load is supported is defined using Hitachi Tabletop Microscope TM3000. To define the effective area of EBM printed Ti6Al4V parts tensile specimens are cut from the gauge area and polished using mechanical polisher with a 1200 grit sandpaper.

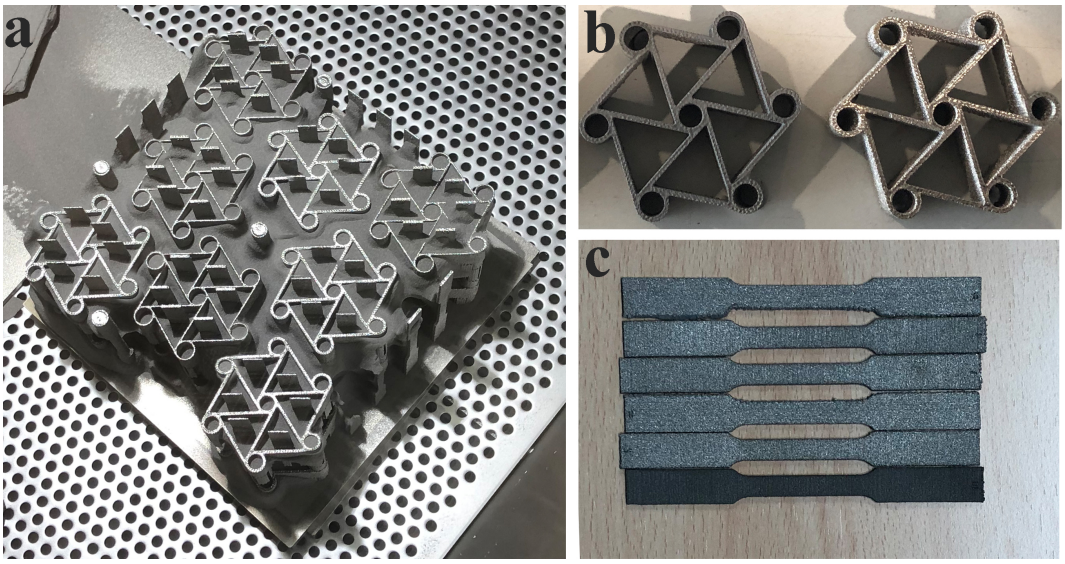

Figure 5.19 : EBM printed parts: (a) printed parts in powder cake (b) as-built and sandblasted chiral parts (c)as-built and sandblasted tensile specimens.

The powder used in this study was a mixture of 50% new powder and 50% leftover powder from previous build.

5.4.3 Chiral cellular structures

The chiral auxetic solid network can be described by the nodes and ligaments interconnected structures, each end of the ligaments is tangentially linked to the nodes. Repeated smallest parts of the network can be defined as a unit cell, and the network's mechanical behaviour can be closely deduced by unit cells' mechanical behaviour by avoiding high costs. The number of ligaments linked to one node identifies the chiral lattice structures type as trichiral, tetrachiral, and hexachiral structures including 3, 4, and 6 tangential ligaments connected to one node, respectively. The anti prefix for chiral auxetic structures is meant to define the spatial relationships among chiral network nodes and ligaments; chiral lattice auxetic structures with cylindrical nodes on the opposite direction of the ligament tips are called chiral network systems, while cylinders on the same direction of the ligament are called antichiral systems. Nevertheless, all chiral network systems do not exhibit negative Poisson's ratio; 4 and 6 ligaments linked systems and short ligament-limited anti-trichiral network systems just reveal the auxeticity [54]. Chiral system deformation begins with node rotation, and ligament flexing and bending as a result of node rotation. During the deformation of chiral lattice cells, two different ligament deformations can be seen according

to the type of chiral network system. The full wave-shaped ligament deformations can occur in the chiral systems and half-wave shaped ligament deformations in the anti chiral network systems. The full-wave shaped ligaments absorb more energy in crashworthiness and compression applications [36]. The chiral hexagonal auxetic lattice structure is selected for this study, which exhibits full-wave shaped ligament deformation. The chiral hexagonal unit cell and unit cell topology parameters are shown in Figure 5.20. The structure consists of equal-sized cylinders or nodes linked by the ribs, walls, or ligaments of the same length L. The extrusion length of the chiral cells is indicated by e. The nodes outer radius are referred by r, and the negative Poisson's ratio is generated by the bending of the ligaments around the nodes.

The angle of θ and β are the topology parameters, and their relationships between other parameters are given in Equation 5.2.

$$sin\,\beta = \frac{2r}{R},\ cos\,\beta = \frac{L}{R},\ tan\,\beta = \frac{2r}{L},\ sin\,\theta = \frac{R/2}{R} = 0.5;\ \theta = 30 \tag{5.2}$$

Equation 5.2 defines topology layout and ligament orientations regards to the imaginary line between the nodes center [146, 147]. Among the parameters, cos β has a special place by dominating the chiral geometry significantly, and according to the study of Spadoni et al. [160] on chiral structure filled truss-core aerofoils, L/R mainly affects the mechanical performance of the chiral structure. In the study of Prall and Lakes, -1 Poisson's ratio of the chiral structure is shown theoretically with rigid node assumption. According to this study, the elastic modulus of the chiral structure is given in Equation 2 [146]. E_s is Young's modulus of lattice cell material. To obtain stiffer chiral cells the thickness of the chiral cells can be increased, and ligament length and radius of nodes can be decreased. Two different chiral lattice cells with different thicknesses of 0.8 mm and 1.6 mm, called C1 and C2 hereafter, respectively, are subjected to this study to investigate the effect of thickness.

$$E = E_s\sqrt{3}\,\frac{t^3}{L\,r^2} \tag{5.3}$$

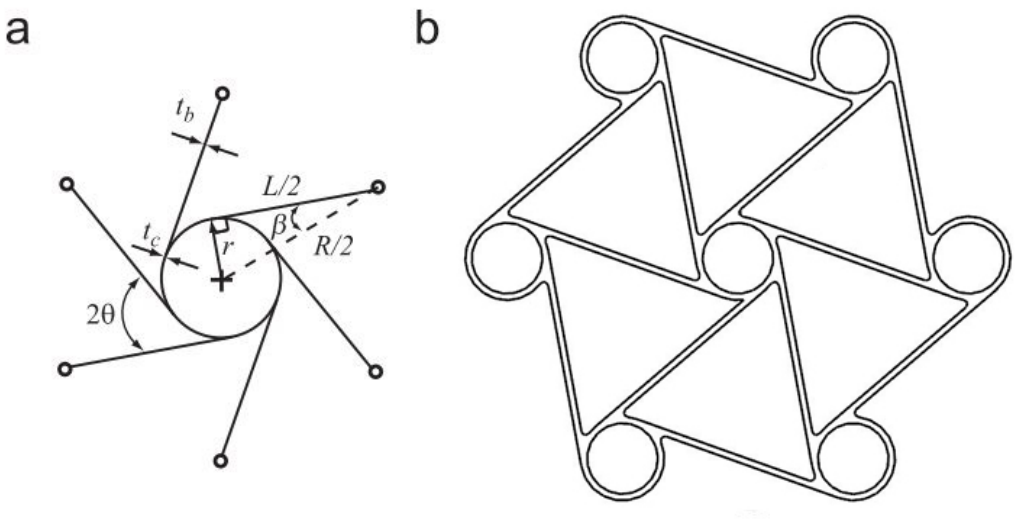

Figure 5.20 : Hexagonal chiral unit lattice: (a) geometrical parameters and (b) unit cel.

Figure 5.20 shows that there are two parameters of thickness; one of them is for node thickness, t_c and another is for ligament thickness, t_b. The key explanation for this disparity is the manufacturing process, as readily available honeycomb lattice structures are continuously made out of an aluminium sheet by slicing and folding aluminium rolls and welding or bonding of the processed parts [49]. However, using AM it is possible to achieve the equal thicknesses of ligaments and nodes. t is, therefore, implemented in this analysis instead of t_c and t_b. Due to the production limitations of the EBM 3D printer, the proportions of the chiral unit cells were determined.

Table 5.3 : Dimensions of the unit chiral cells.

$\sin\beta$	$\cos\beta$	$\sin\theta$	L (mm)
0.36	0.93	0.5	26.81

5.4.4 Mechanical characterization and tests

EBM printed parts show anisotropic behaviour due to the layerwise production method. To understand the mechanical behaviour and characterize EBM printed parts tensile tests are conducted according to ASTM E8M with a velocity of 0.45 mm/min. For the three-point bending test, a testing jig (Figure 5.21) with a span length of 15 mm and a pin radius of 1.5 mm is used. The test rate for bending is defined as 1.47 mm/min according to having the same strain rate of the tensile test. Each tensile and bending

test specimens are produced in two different directions, 0^o and 90^o due to characteristic anisotropic behaviour of EBM printed parts. Chiral lattice cells are produced laterally on the flatwise direction to prevent the difficulty of the supports removal process and obtain higher mechanical performance in the edgewise direction according to tensile results.

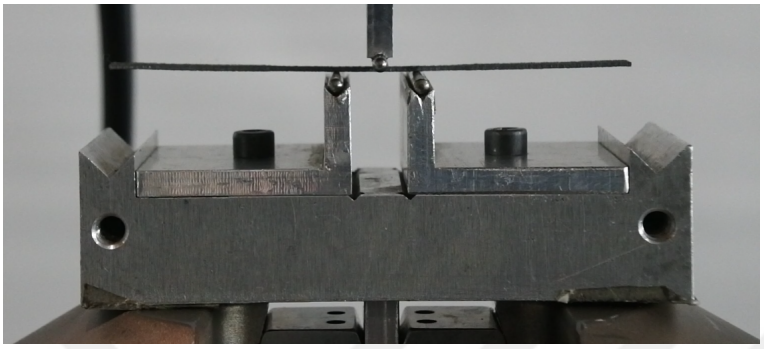

Figure 5.21 : Flexural test fixture.

In all tests, MTS 810 Material Test System (250 max payload) was used with MTS 647 Hydraulic Wedge Grip, and MTS 634.31F-24 extensometer was deployed in the tensile tests. In addition, for the chiral lattice compression tests, an additional fixture is designed and produced Appendix A.1. Furthermore, two pins and bearings are used to connect the chiral unit structure to the fixture. Two upper and lower nodes of chiral unit cell are assisted with two cylindrical pins and bearings to allow the lateral motion and rotation of the nodes, as seen in Figure 5.22.

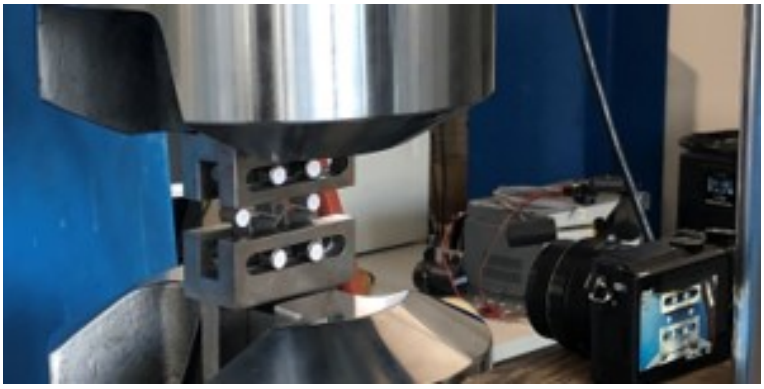

Figure 5.22 : Fixture for chiral lattice compressionl.

The test velocity was defined as 1 mm/min for both cyclic and crush tests. For crush tests two rigid plates were adopted to compress unit cells, and plates were lubricated well to reduce friction between samples and plate surfaces in terms of enabling the auxeticity with free movement of nodes touching to the plates. The test setup and EBM

manufactured Ti6Al4V ELI chiral cells can be seen in Figure 5.23. According to study of Ladani et al. [161], it is found that, under three specific strain rate level of 0.0005, 0.001 and 0.01, the strain rate sensitivity in the lateral direction production does not have considerable effect in certain limits. So, results can be deduced for different strain rate deformations from low strain rate deformations. Moreover, transverse strains were measured to calculate Poisson's ratio (Figure 5.24).

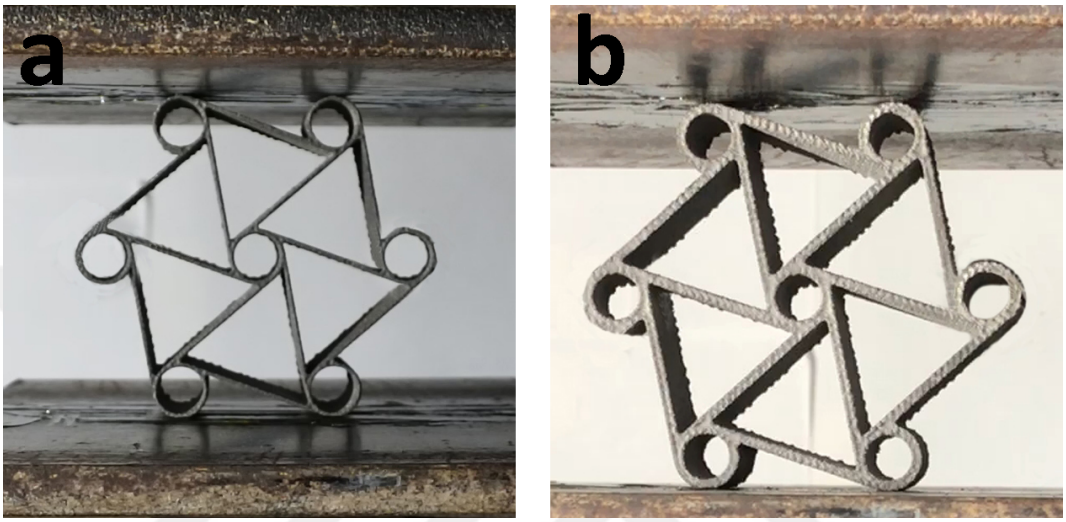

Figure 5.23 : Crush test setup and specimens of a) 0.8 mm b) 1.6 mm ligament thicknessed chiral unit cells.

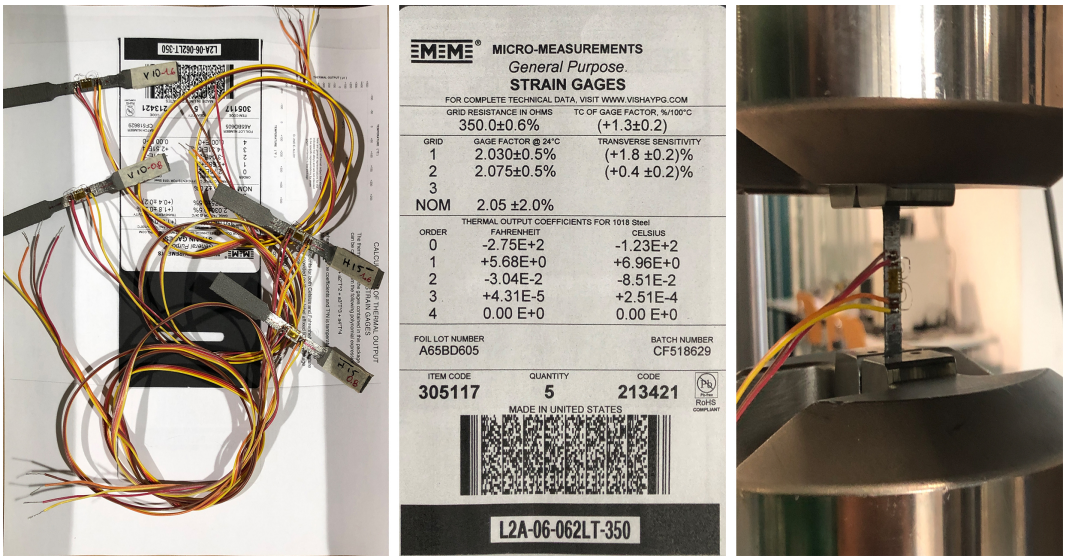

Figure 5.24 : Specimens, strain gauge properties and test setup.

For measurement of lateral deformation, all tests were recorded with a high definition camera as seen on Figure 5.22, and speckled papers placed on the nodes to track their movements.

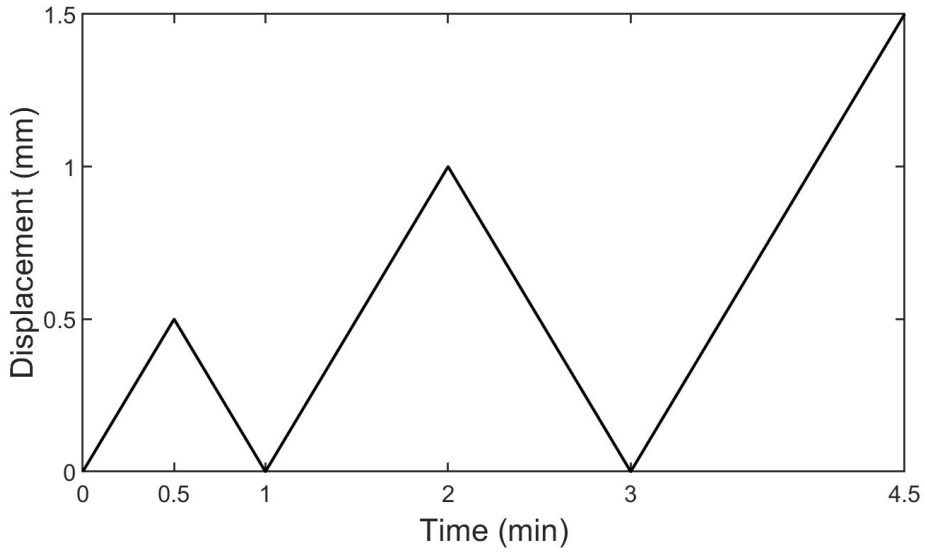

Figure 5.25 : Compressive load profile for chiral lattices.

Furthermore, chiral lattice cells with different thicknesses of 0.8 mm and 1.6 mm was tested with a compressive load profile to investigate its displacement limit by applying large displacements without experiencing permanent deformations, degradation or failures. The compressive load profile is depicted in Figure 5.25. To apply compressive load profile special fixtures having two components are used. Upper component of fixture was moving, and lower component was fixed. The lower and upper component of fixture was connected with the chiral cells through the nodes by the help of two pins, and the upper component is applying compression and tensile through two pins. In the tensile phase, tensile process continues until the load reaches zero, and then compression starts and proceeds until to the defined displacement limits.

5.4.5 Numerical Analysis

For numerical analysis of the three steps cyclic compression of C1 and C2 implicit finite element models are established using ABAQUS 2018. In the analyses, quadratic brick element (C3D20R) having 2x2x2 integration points (reduced integration) was used. Because of the complex shape and curved edges, in the meshing processes, maximum deviation factor was kept under the value of 0.1, and maximum aspect ratio is defined as 3. The choice of element type and size plays an vital role to obtain close results to exact experimental results while minimising the computational cost. So that quadratic elements is selected, and convergence studies was conducted. As a result, approximately 47628 continuum elements for C1 and 114976 for C2 were

created. The simulation of the finite element was performed on a computer with 16 cores and 24 GB of RAM, and the time of the wall clock for C1 simulation is 22 hours and 102 hours for C2. The elastic and plastic deformation under cyclic load of C1 and C2 structures were assessed using non-linear analysis. Also, non-linear material was used with geometric stiffening and finite strain elements. For solving the global equation Newton-Raphson method was used with a fixed step of 1.661e-3. The material was perceived to be linearly elastic and also the beginning of plastic deformation is stated with the commencement of yield stress of Ti6Al4V ELI. Self contact interaction with penalty algorithm was used. To simulate the free rotation of the nodes by the means of rigid pins and bearings continuum distributing couplings were utilized in the analyses. For the distributing couplings single element nodes are created in the middle of centre line of the cylindrical chiral nodes, and element nodes attached to the inner surface of the cylindrical chiral nodes to make the surface rigid. Boundary conditions of the cylindrical nodes are applied directly to the element nodes. In addition, one element node was created to attach the upper element nodes of the chiral nodes by equation constraint to measure the displacement and reaction forces. From the experimental observations, the boundary conditions are adapted to the element nodes. As to boundary conditions, upper and lower cylindrical chiral nodes can freely rotate in the flatwise direction axis (Z), and all the nodes can move in the X and Y directions except lower chiral nodes as seen in Figure 5.26. Moreover, a subroutine (see Appendix A.4) is deployed to define the load and displacement control at the same time for the compressive load profile. As for the numerical analysis of the crush of C1 and C2, explicit finite element models were established using ABAQUS. In the analyses, C3D8I eight-node linear brick element, which is improved by incompatible modes to enhance the capturing of bending behavior, were used. Same maximum deviation factor, maximum aspect ratio and the number of elements were deployed as it is in the cyclic compression analysis. In addition to linear elasticity material model, for the simulation of the plastic behaviour and failure, classical metal plasticity material was used in conjunction with ductile damage initiation criterion and progressive damage evolution law for ductile metals. General contact interaction with penalty algorithm was utilized.

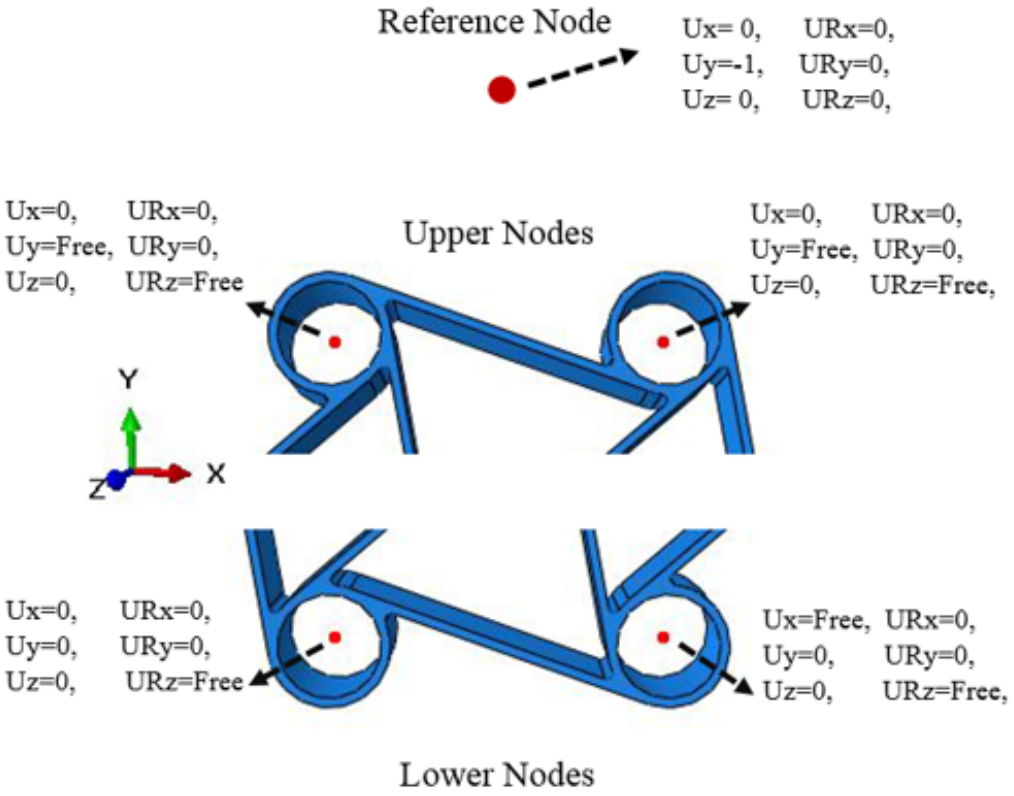

Figure 5.26 : Unit cell boundary conditions.

5.5 Results

The sandblasting process was applied to all parts to remove loose particles and decrease the surface roughness. Arithmetical mean deviation (R_a) of the assessed profiles were found 20.325 μm with a decrease of 5% after the sandblasting process. After that, regarding the determination of the effective area, cross-sections from the middle of the gauge area of tensile specimens were cut out and investigated under a microscope.

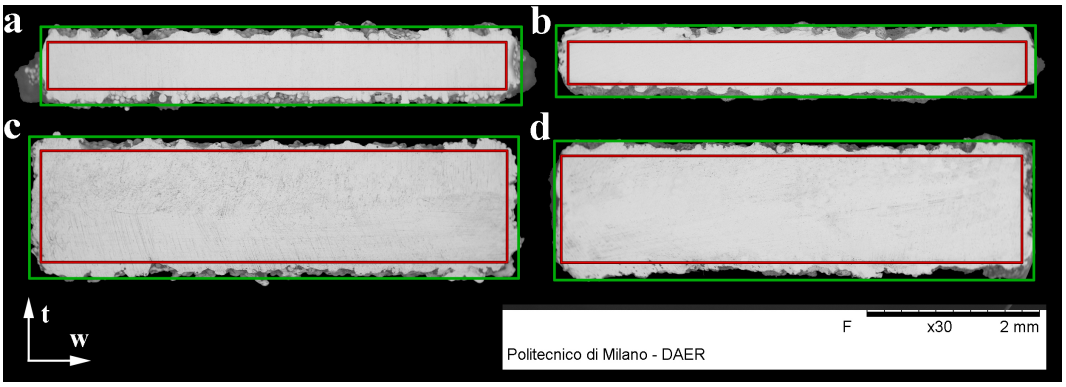

Figure 5.27 : Cross-sections for a) 90-degree, 0.8 mm thickness b) 0-degree, 0.8 mm thicknessa) c) 90-degree, 1.6 mm thickness d) 0-degree, 1.6 mm thickness.

The green and red rectangular areas show the measured area and effective are, respectively, seen in Figure 5.27. The area between red and green area can be assessed as mechanically inefficient area, owing to the irregular amount of material that does not carry the load along with the tensile specimen. It is found that the inefficient load carrying region in the thickness (t) direction is not variable according to the thickness of produced parts. For asbuilt parts, the inefficient layer thickness is 0.175 mm, and 0.165 mm for sandblasted parts. Also, the inefficient layer thickness in the width direction shows a similar pattern, and it is 0.130 mm and 0.120 mm for asbuilt and sandblasted parts, respectively. As a result, the effective area (A_e) can be calculated according to Equation 5.4 for sandblasted parts.

$$A_e = (t - 0.165) * (w - 0.120) \tag{5.4}$$

Ti6Al4V tensile test specimens were produced according to ASTM E8M in two different directions of horizontal and vertical. Five specimens were produced and tested for each direction. Due to high surface roughness of EBM printed parts, tensile parts were sandblasted in the same manner before the testings to reduce the surface roughness. In addition, Poisson's ratio of horizontal test specimens with different thickness of 0.8 mm and 1.6 mm were found 0.3 and for verticals were 0.31.

The tensile test results are calculated with the measured cross-section area values are given as as-received results, and re-calculated results according to Equation 5.4 are labelled as corrected results. As a consequence of the investigation of the corrected tensile results, Young's moduli that measured have no considerable variation according to building direction and specimen thickness with a value of 110±8 GPa for 1.6

mm thickness and 110±10 GPa for 0.8 mm thickness specimens. The yield stress and ultimate tensile strength values are 847±5 MPa and 901±9 MPa for 0-degree orientation production, and 989±12 MPa and 1040±12 MPa for 90-degree orientation builds regarding 0.8 mm thickness specimens, respectively. For the 1.6 mm thickness specimens, the yield stress and ultimate strength values can be listed as 855±3 MPa and 903±1 MPa for 0-degree orientation production, and 934±11 MPa and 1005±3 MPa for 90-degree production. The results show that the direction of production and the thickness of the sample were not dominant factors for Young's modulus, but better yields stress and ultimate tensile strength values are experienced in the 90^o building orientations. However, very low strain at break values was obtained for 0.8 mm thickness specimens; 0^o build exhibits 2.42±0.21% and 90 degree shows 1.99±0.07%. The strain at break values for 1.6 mm thickness specimens was more significant and better when compared to the 0.8mm thickness specimens with a value of 4.93±0.41% and 4.50±0.19% for 0^o and 90^o build orientations, respectively. The early mentioned company specified mechanical properties in Section 5.1 are higher than the experimental test results. This circumstance can be clarified by the lack of fusion, oxidation, high surface roughness, and leftover parts and surface deformation stem from the support removal process due to EBM production method and material in-homogeneity. The reason for the difference in the strain at break values for 0.8 mm and 1.6 mm thicknesses can be explained by the effect of local deformation due to high surface roughness. The effective load supporting area is greater for 1.6 mm thickness specimens which can endure more under the effect of high local deformations. Moreover, better mechanical performance in the 90^o build orientation can be explained by the same direction of loading with the layers.

Table 5.4 : Dimensions of C1 and C2 as design, asbuilt and sandblasted (*D - design, A - asbuilt, S - sandblasted).

	h (mm)	d_o (mm)	d_i (mm)	t (mm)	e (mm)
C1 D	60.27	10.44	8.84	0.8	16
C1 A	60.26±0.12	10.49±0.12	8.30±0.11	1.04±0.03	16.31±0.17
C1 S	60.13±0.13	10.44±0.01	8.29±0.13	0.97±0.04	16.23±0.11
C2 D	60.27	10.44	7.24	1.6	16
C2 A	60.37±0.07	10.49±0.07	6.83±0.10	1.79±0.04	16.49±0.05
C2 S	60.26±0.12	10.35±0.04	6.82±0.10	1.71±0.03	16.43±0.05

As a result of the tensile study outputs, it is found that EBM printed Ti4Al6V parts with a particular build theme show isotropic elastic and plastic anisotropic behaviour. However, due to the variations in the strain at break, 90^{o} production demonstrates consistent mechanical performance in comparison to the 0^{o} production orientation, this is also the explanation for the production of chiral unit cells where their flat surface is parallel to the building plate surface. Additionally, net shaping is an important phenomenon for production systems, and thus, the dimensions of both C1 and C2 were measured to check dimensional accuracy, and results can be seen in the Table 5.4. Considering sandblasted part dimensions, the height and nodes outer radius of both C1 and C2 are in the tolerance of 1%, however, extrusion length of cells are in the tolerance of 3% after sandblasting. The thickness of the ligaments for C1 is 0.97 with a difference of 21%, and 1.71 for C2 with a difference of 12%. Moreover, the inner radius of nodes for C1 and C2 are 6% lesser than design dimensions. As to asbuilt parts dimensional accuracy check, their dimensions differ from the sandblasted parts is nearly 0.10 mm except inner diameter of nodes. Sandblasting cannot be applied perpendicularly to the node surfaces due to narrow space. According to measured dimensions and Equation 5.3, C1 and C2 redesigned and used in FEM analysis with the new dimensions.

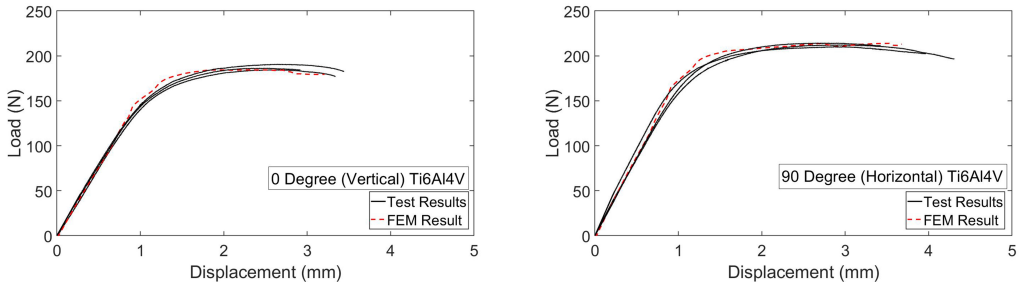

Figure 5.28 : Load-deflection curves for 0-degree and 90-degree build orientation specimens for bending test.

Consequently, parameters for the constitutive equation are acquired, adjusted and imported into FEM codes as a consequence of experimental studies to constitute the material's behaviour. In the FEM analysis, isotropic elasticity and plasticity were used to validate flexural test results and to measure the deformation limit of the chiral unit cell without experiencing permanent deformations, degradation or failures. As seen in Figure 5.28, close correlations were monitored between flexural test and numeric

analysis results. Furthermore, as a result of the chiral compressive load tests and FEM analysis, Figure 5.29 is obtained.

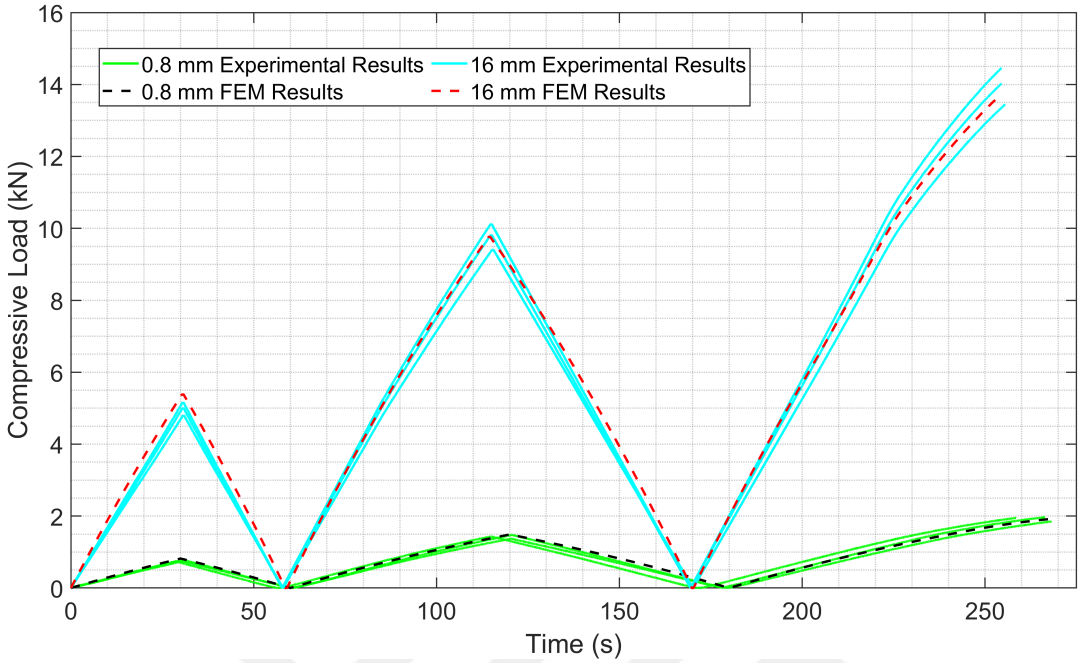

Figure 5.29 : Compressive load profile experimental and FEM results for chiral unit cells of a) 0.8 mm thickness b) 1.6 mm thickness.

In the first two cycles which have 0.5 and 1 mm displacement limits, permanent contractions were 0.15% and 0.3%, respectively, in the height was observed for C1. Poisson's ratio was measured as -0.64 in the first cycle, -0.40 in the second cycle, and -0.32 in the third cycle. The decreasing change in the in Poisson's ratio is the nonlinear deformation of the chiral cell and microplastic deformation. However, no lateral deformation was observed, and, consequently, negative or positive Poisson's ratio was not monitored in C2. The permanent contractions of 0.1% in the first cycle, and 0.17% in the second cycle were observed. The ligaments of the structure were too rigid to be run the wrapping mechanism of the chiral cell. The calculated stiffness value of C2 is 11 kN/mm, and 1.45 kN/mm for C1, which validates Equation 5.3. As a result of compressive load profile, the unit chiral lattice cells have yield stress limit under the compressive loads greater than 1790 N in the last cycle of load profile with a displacement of 1.312 mm for C1, and 10.94 kN in the last cycle of load profile with a displacement of 1.051 mm for C2. In addition, as for crush performance of C1 and C2, Figure 5.29 shows four C1 and C2 and FEM results of unit cell load-deflection curves.

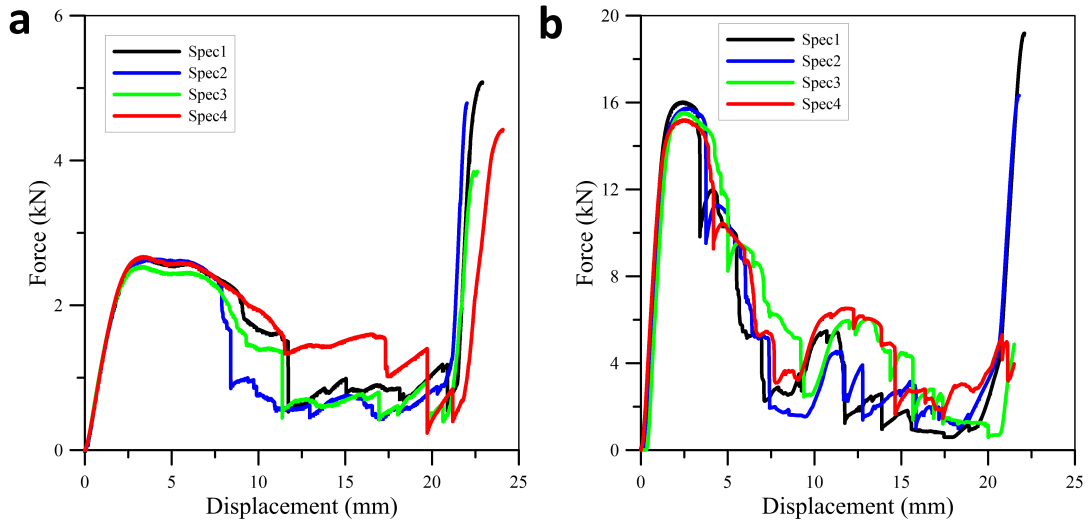

Figure 5.30 : Compressive load and deflection graph chiral unit cell with a ligament thickness of a) 0.8 mm b) 1.6 mm.

In the first phases where bending of the ligaments happen in between 2.50 and 2.70 N for C1, and it is followed by the collapse of the cell which experiences acceptable plateau phase. In the almost half of the plateau phase, the peak force is kept and a slight reduction is observed which directly affects the CFE value. The densification phase, where structure acts as a bulk material, starts in between 20 and 22.5 mm strokes. As for C2 specimens, they experience better consistency in their response to crush load, however, the collapse of the cell starts prematurely which cause low CFE value. The peak value C2 specimens reaches almost 6 to 7 times which is already expected from Equation 5.3. Moreover, the plateau phase of the C2 unit cell is not in an acceptable range. The crushing indexes of both structures can be seen in Table 5.5. According to the table, it can be said that even if the SEA value of C2 is better than C1, CFE of C2 is not in a feasible range. However, both structures experience similar densification displacements.

Table 5.5 : Crush indexes for C1 and C2.

	C1				C2			
	1	2	3	4	1	2	3	4
PCF (kN)	2.65	2.64	2.53	2.67	16.01	15.73	15.53	15.20
MCF (kN)	1.51	1.28	1.35	1.69	5.21	5.40	6.17	7.01
CFE	0.57	0.48	0.53	0.63	0.32	0.34	0.39	0.46
SEA (kJ/gr)	1.14	0.94	1.01	1.31	1.94	1.97	2.46	2.35

In Figure 5.31, the crush results of C1 and C2 for experimental tests and FEM analysis are presented. The correlation between numerical and experimental results are seen

in the acceptable range so the numerical models can be used for simulating the crush scenario of chiral auxetic structures. In the first region in which only elastic deformation occurs, close correlation can be seen, however, in the plateau region where rotation and sliding of the chiral cells, plastic deformation and failures took place besides elastic deformation, results of FEM and experiments are differing. In the plateau region, for experimental results, fluctuating behaviour is more common than the FEM results. This situation can be explained by the high surface roughness and discontinuity on the surface of the chiral cells which caused jamming and instantaneous lateral movement of the chiral cells under crush loads which cannot be observed in the FEM analysis. In regard to the investigation of the onset of densification, it can be said that similar behaviour can be captured in the approximate points.

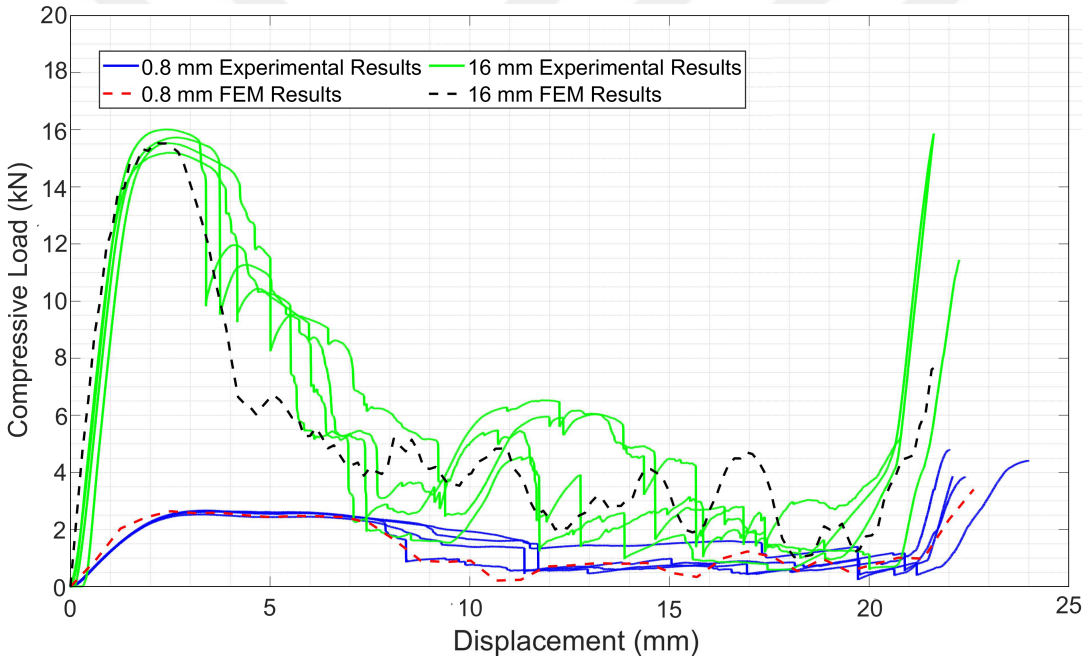

Figure 5.31 : FEM and experimental results for the crush of chiral unitcells of a) 0.8 mm thickness b) 1.6 mm thickness.

To have a better explanation about the compressive load-displacement curves, deformation of chiral cells is to be investigated systematically. Comparison of the experimentally and numerically deformed cells can be seen with 5 mm deflection intervals in Figure 5.32. The ligaments and nodes are designated with the letters and numbers for better explaining the deformation mode of the C1 and C2 chiral cells which can be seen in the numerical model in the no deflection stage of C1 in Figure 5.32. Ligaments of C1 experienced s-shape deformation which is very useful for better

energy absorption, however, L8 and L5 performed a lower rate of bending. In C2, s-shaped deformation cannot be observed due to high ligament thickness, and instead, failures occurred in the upper tips of the L1, L2 and L3, and lower tips of the L10, L11 and L12. So it can be concluded that the higher stress emerges above-mentioned points which gives an idea about the points and regions which must be improved for better energy absorption. Additionally, deformation modes of the cells in the experiments and numerical analysis are quite similar. Under 10 mm displacement, the deformation mode is analogous with the deformation under 5 mm displacement for both C1 and C2, however, in C2, N1 becomes a separate part after losing the connection with the all ligaments. Also, mesh element deletion can be seen in C1 which is the sign of fracture starts. In the 15 mm displacement, the upper tip of the L1 and the lower tip of the L11 failed in C1. In C2, the cell lost its structural integrity and it starts to collapse. In addition, the lateral contradiction of the C1 and C2 can be monitored in 5 and 10 mm deflections. However, after the failure of the ligaments start, lateral expansion or no lateral change can be seen. This also clarifies that the failures prevent auxetic behaviour. Lastly, under 20 mm displacement where densification starts or approaches to the onset of densification point, N1, N4 and N7 locate in the same vertical line and begins to touch each other. This deformation mode causes the high crush load which can be seen in Figure 5.31 as the densification load. As a result, using linear elasticity and classical plasticity models in conjunction with damage initiation for ductile metals, damage evolution and element removal for ductile metals [91] specifications, failure of the C1 and C2 auxetic cells under crush load can be obtained and close correlation can be captured.

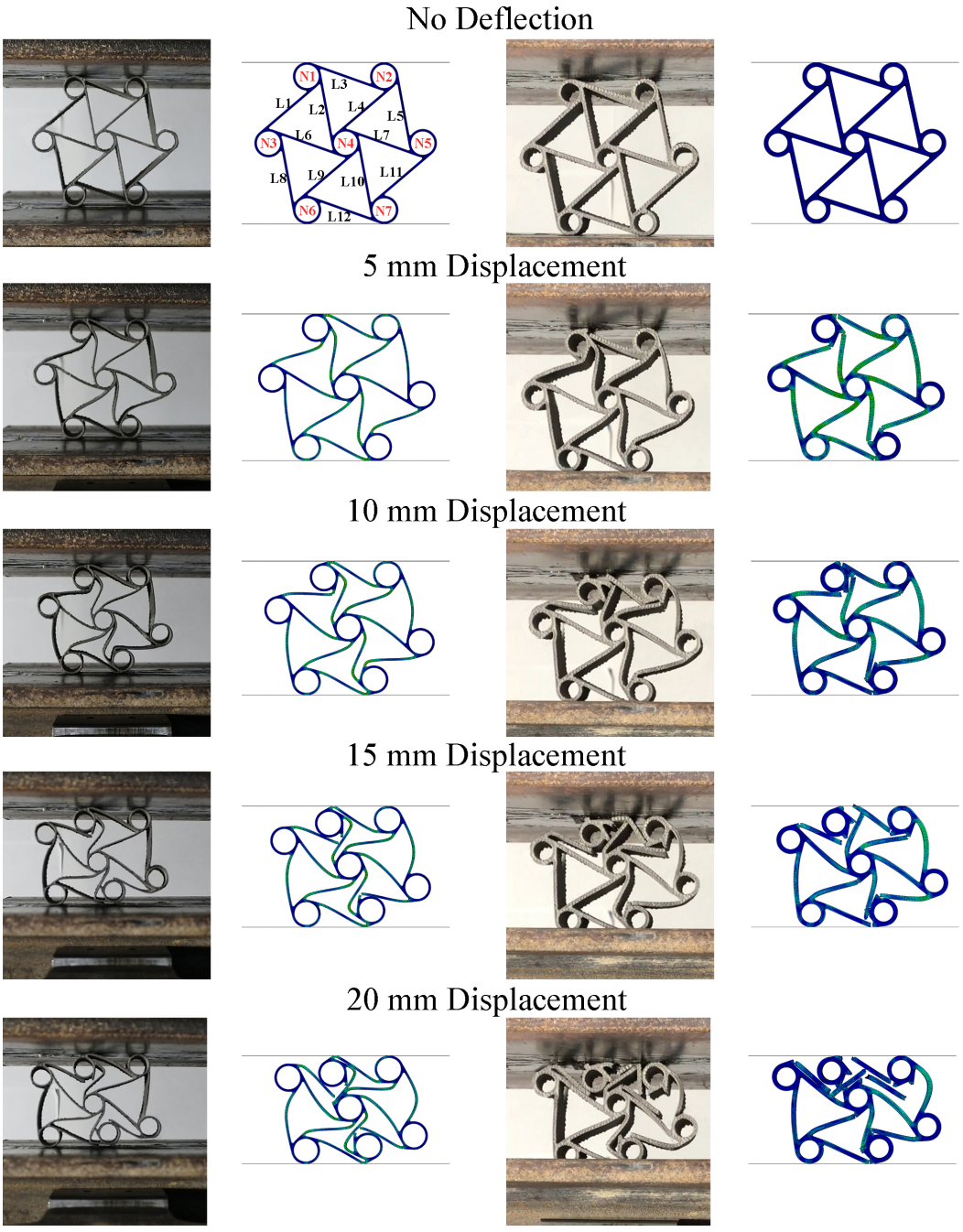

Figure 5.32 : Comparison of FEM and experimental deformation stages for the crush of chiral unitcells of a) 0.8 mm thickness b) 1.6 mm thickness.

5.6 Overview and Discussion

The result of the material characterization of EBM printed Ti6Al4V can be summarized as isotropic elasticity and anisotropic plasticity. In 0^o and 90^o building

orientation, 0^o build showed the consistent and better results with the average 4.93% strain at break value, and 90^o showed lower strain at break which is not preferable for compression applications. According to tensile results, a constitutive equation was obtained, and used in three-point flexural FEM simulation to validate the constitutive equation regarding experimental results of three-point flexural tests. The equation was validated and also used for compressive load profile analysis. As a consequence of the compressive load profile test, the results of plastic deformations were defined in every step, and stiffness of two different chiral cells were calculated and compared. Consequently, variation in the thickness was changed the stiffness of the chiral cells by the third power of thickness ratio. Additionally, change in ligament thickness can change the auxetic characteristics of the chiral cell, and its deformation pattern. The lateral deformation was not observed in the 1.6 mm thickness chiral cell. Also, the onset of the nonlinear deformation and onset of the yield stress were defined and validated with experimental results. As to crush test, 0.8 mm chiral unit cell experiences better CFE value which is very important for whiplash issues during the accidents, however, 1.6 mm chiral unit cell experiences better SEA value.

6. CONCLUSIONS AND RECOMMENDATIONS

The main objective of this thesis is the production of auxetic lattice cells using two different additive manufacturing technology and two different materials to find better energy absorbing 2D lattice cell, using better energy absorbing cell for a special application and understanding both additive manufacturing technology characteristics and material behaviour, and obtaining constitutive equations for FEM simulation. In this context, the production problems of fused deposition modelling are elaborated and attention is drawn on material quality, the importance of printing parameters, and room and ground where the device is located to avoid bad printings. In conjunction with this flaw study, the effect of the layer thickness of FDM printed ABS is investigated, and it is found that the minimum layer thickness (0.09mm) showed the best specific tensile stress and Young's modulus.

As for the conclusion of EBM printed Ti6Al4V ELI, the effect of production region in building chamber on the mechanical performance of the produced components, and it can be said that region has no considerable effect on mechanical performance if it is not affected by high heat gradients. However, the production orientation is a major effective parameter for mechanical characteristics of produced parts; it affects the EBM produced Ti6Al4V components of plastic behaviour. The Young's modulus, yield stress, ultimate stress for 0^o, 45^o and 90^o oriented specimens experience almost similar average values, however, strain at break values are quite inconsistent. The reason which is laid behind is the orientation based influence of lack of fusion problems. Due to characteristics of layerwise production method, lack of fusion problems behaves differently according to the loading direction. They can be seen as black speckles in the powder distribution direction (90^o), and same lack of fusion defects can be observed as unfused or semi-fused regions in the perpendicular direction (0^o) to the powder distribution direction. Thus, lack of fusion defects tend to become wider under the loading in the 0^o direction, however in the loading of 90^o direction, on the contrary, they have a tendency to close the defect openness. As a consequence, it can

be said that the reason for anisotropic plasticity behaviour of EBM printed Ti6Al4V is caused by the defects. In this manner, it is suggested that the usage of linear elasticity material model in conjunction with classical metal plasticity material model in the large deformation FEM analysis acceptable results can be captured if the constitutive equation is obtained from a tensile result of 90^{o} oriented specimens, and the load is applied in the same direction. Otherwise, it is expected to model defects in FEM analysis to have better results for crush analysis. Additionally, as a consequence of measuring the defect areas from SEM images of failure zones, a close linear correlation is captured in relation with defect area and strain at break.

In terms of auxetic lattice cells, 2D auxetic lattice cell auxeticity mechanisms are compared to find feasible geometry for energy absorption under crush loads in the edgewise direction where auxeticity is experienced, and rotating rigid 2D auxeticity mechanism is excluded due to its improper crashworthiness specification. In comparison to re-entrant and anti-tetrachiral auxetic lattice cells, the anti-tetrachiral structure shows overmuch energy-absorbing ability over the re-entrant structure, and the topology of the re-entrant structure is modified for new comparison study. For the new re-entrant and anti-tetrachiral structures, energy absorption ability study is conducted step by step experimentally and numerically in terms of deformation modes. Consequently, anti-tetrachiral auxetic lattices present better energy absorption capability which stems from its wrapping chiral mechanism. Thus, a benchmark study is performed to find better energy absorbing topology among wrapping mechanism having typologies which are hexachiral (chiral), tetrachiral, anti-tetrachiral, trichiral, and anti-trichiral. Also, the regular honeycomb lattice structure is added for better comparison, and as a result, hexachiral (chiral) structure is selected for further studies for its unique crush performance. Moreover, FDM printed ABS chiral auxetic lattice is used filling material for composite tubes, and it experiencee, a significant increase of 450% SEA value in the lateral crush. Lastly, EBM printed Ti6Al4V chiral unit lattice structures with different wall thicknesses of 0.8 and 1.6 mm are tested with a compressive load profile at very low velocity (1 mm/min) to investigate its displacement limit by applying large displacements without experiencing permanent deformations, degradation or failures for determining the limitation of auxeticity of a chiral cell, and energy absorption behaviour under crush loads is investigated. The

chiral auxetic unit cell with 1.6 mm thickness does not experience auxeticity due to its thick ligaments; thick ligaments cannot wrap on chiral nodes under deformation. Moreover, the chiral auxetic unit cell with 1.6 mm thickness shows better SEA value however its CFE is not within an acceptable range. For simulating the crush scenario of auxetic cells, damage and failure criteria for ductile metals are used. Thus, quite close correlations are captured and the failure regions and behaviours are detected to enable the improvement of the current chiral configurations.

As a recommendation context, it can be suggested that the modification in chiral tpologies can take its energy absorption capabilities forward. Moreover, some special structures like foam or auxetic foams can be used as filling material for gaps in the chiral cells. As for the analysis part, internal defects of additively manufactured parts can be modelled in FEM using XFEM or ductile damage modelling to have better results and obtain the fracture deformation pattern.

6.1 Practical Application of This Study

Energy absorption is an important phenomenon for human lives and structural integrity. Energy-absorbing materials are of broad interest for protection from impacts and shock waves in applications ranging from helmets to vehicles and sporting gear. The outputs of this study can be used for special applications such as helicopter landing gears, automotive crashbox systems, filling lattices for spacecraft cells. As an output of this thesis, an international patent application about a novel automobile crashbox design was performed.

REFERENCES

[1] **Organization, W.H.** (2002). A graphical overview of the global burden of injuries, *The Injury Chart Book*, *29*.

[2] **Evans, A.G.**, **Hutchinson, J.W.**, **Fleck, N.A.**, **Ashby, M. and Wadley, H.** (2001). The topological design of multifunctional cellular metals, *Progress in Materials Science*, *46*(3-4), 309–327.

[3] **Lu, G. and Yu, T.** (2003). *Energy absorption of structures and materials*, Elsevier.

[4] **Hou, W.**, **Zhu, F.**, **Lu, G. and Fang, D.N.** (2010). Ballistic impact experiments of metallic sandwich panels with aluminium foam core, *International journal of impact engineering*, *37*(10), 1045–1055.

[5] **Rizov, V.**, **Shipsha, A. and Zenkert, D.** (2005). Indentation study of foam core sandwich composite panels, *Composite structures*, *69*(1), 95–102.

[6] **Liu, H.**, **Liu, H. and Yang, J.** (2017). Clamped sandwich beams with thick weak cores from central impact: A theoretical study, *Composite Structures*, *169*, 21–28.

[7] **Zhu, F.**, **Zhao, L.**, **Lu, G. and Gad, E.** (2009). A numerical simulation of the blast impact of square metallic sandwich panels, *International Journal of Impact Engineering*, *36*(5), 687–699.

[8] **Zhu, F.**, **Wang, Z.**, **Lu, G. and Nurick, G.** (2010). Some theoretical considerations on the dynamic response of sandwich structures under impulsive loading, *International Journal of Impact Engineering*, *37*(6), 625–637.

[9] **Wang, D.** (2009). Impact behavior and energy absorption of paper honeycomb sandwich panels, *International Journal of Impact Engineering*, *36*(1), 110–114.

[10] **Grassi, M.**, **Zhang, X. and Meo, M.** (2002). Prediction of stiffness and stresses in z-fibre reinforced composite laminates, *Composites Part A: applied science and manufacturing*, *33*(12), 1653–1664.

[11] **Meo, M.**, **Vignjevic, R. and Marengo, G.** (2005). The response of honeycomb sandwich panels under low-velocity impact loading, *International journal of mechanical sciences*, *47*(9), 1301–1325.

[12] **Liu, H.**, **Liu, H.**, **Yang, J. and Zhao, S.** (2013). Cantilever sandwich beams with pyramidal truss cores subjected to tip impact, *Science China Technological Sciences*, *56*(1), 181–187.

[13] **Wicks, N. and Hutchinson, J.W.** (2004). Performance of sandwich plates with truss cores, *Mechanics of Materials*, *36*(8), 739–751.

[14] **Schaedler, T.A. and Carter, W.B.** (2016). Architected cellular materials, *Annual Review of Materials Research*, *46*, 187–210.

[15] **Smith, M.**, **Guan, Z. and Cantwell, W.** (2013). Finite element modelling of the compressive response of lattice structures manufactured using the selective laser melting technique, *International Journal of Mechanical Sciences*, *67*, 28–41.

[16] **Ziemian, C.**, **Sharma, M. and Ziemian, S.** (2012). Anisotropic mechanical properties of ABS parts fabricated by fused deposition modelling, *Mechanical engineering*, *23*.

[17] **Huang, J.**, **Zhang, Q.**, **Scarpa, F.**, **Liu, Y. and Leng, J.** (2017). In-plane elasticity of a novel auxetic honeycomb design, *Composites Part B: Engineering*, *110*, 72–82.

[18] **Chen, Y.**, **Scarpa, F.**, **Liu, Y. and Leng, J.** (2013). Elasticity of anti-tetrachiral anisotropic lattices, *International Journal of Solids and Structures*, *50*(6), 996–1004.

[19] **Zhou, H.**, **Attard, T.L.**, **Dhiradhamvit, K.**, **Wang, Y. and Erdman, D.** (2015). Crashworthiness characteristics of a carbon fiber reinforced dual-phase epoxy–polyurea hybrid matrix composite, *Composites Part B: Engineering*, *71*, 17–27.

[20] **Scarpa, F.**, **Ciffo, L. and Yates, J.** (2003). Dynamic properties of high structural integrity auxetic open cell foam, *Smart Materials and Structures*, *13*(1), 49.

[21] **Zhang, X.c.**, **Ding, H.m.**, **An, L.q. and Wang, X.l.** (2015). Numerical investigation on dynamic crushing behavior of auxetic honeycombs with various cell-wall angles, *Advances in Mechanical Engineering*, *7*(2), 679678.

[22] **Ingrole, A.**, **Hao, A. and Liang, R.** (2017). Design and modeling of auxetic and hybrid honeycomb structures for in-plane property enhancement, *Materials & Design*, *117*, 72–83.

[23] **Liu, Y.**, **Schaedler, T.A.**, **Jacobsen, A.J.**, **Lu, W.**, **Qiao, Y. and Chen, X.** (2014). Quasi-static crush behavior of hollow microtruss filled with NMF liquid, *Composite Structures*, *115*, 29–40.

[24] **Liu, J.**, **Pattofatto, S.**, **Fang, D.**, **Lu, F. and Zhao, H.** (2015). Impact strength enhancement of aluminum tetrahedral lattice truss core structures, *International Journal of Impact Engineering*, *79*, 3–13.

[25] **Schultz, J.**, **Griese, D.**, **Ju, J.**, **Shankar, P.**, **Summers, J.D. and Thompson, L.** (2012). Design of honeycomb mesostructures for crushing energy absorption, *Journal of Mechanical Design*, *134*(7).

[26] **Alderson, A. and Alderson, K.** (2007). Auxetic materials, *Proceedings of the Institution of Mechanical Engineers, Part G: Journal of Aerospace Engineering*, *221*(4), 565–575.

[27] **Li, H.**, **Ma, Y.**, **Wen, W.**, **Wu, W.**, **Lei, H. and Fang, D.** (2017). In plane mechanical properties of tetrachiral and antitetrachiral hybrid metastructures, *Journal of Applied Mechanics*, *84*(8).

[28] **Evans, K.E.**, **Nkansah, M.**, **Hutchinson, I. and Rogers, S.** (1991). Molecular network design, *Nature*, *353*(6340), 124–124.

[29] **Wu, W.**, **Hu, W.**, **Qian, G.**, **Liao, H.**, **Xu, X. and Berto, F.** (2019). Mechanical design and multifunctional applications of chiral mechanical metamaterials: A review, *Materials & Design*, 107950.

[30] **Wu, W.**, **Song, X.**, **Liang, J.**, **Xia, R.**, **Qian, G. and Fang, D.** (2018). Mechanical properties of anti-tetrachiral auxetic stents, *Composite Structures*, *185*, 381–392.

[31] **Ruan, X.L.**, **Li, J.J.**, **Song, X.K.**, **Zhou, H.J.**, **Yuan, W.X.**, **Wu, W.W. and Xia, R.** (2018). Mechanical design of antichiral-reentrant hybrid intravascular stent, *Int. J. Appl. Mech*, *10*, 1850105.

[32] **Wu, W.**, **Geng, L.**, **Niu, Y.**, **Qi, D.**, **Cui, X. and Fang, D.** (2018). Compression twist deformation of novel tetrachiral architected cylindrical tube inspired by towel gourd tendrils, *Extreme Mechanics Letters*, *20*, 104–111.

[33] **Ma, C.**, **Lei, H.**, **Liang, J.**, **Wu, W.**, **Wang, T. and Fang, D.** (2018). Macroscopic mechanical response of chiral-type cylindrical metastructures under axial compression loading, *Materials & Design*, *158*, 198–212.

[34] **Yu, H.**, **Wu, W.**, **Zhang, J.**, **Chen, J.**, **Liao, H. and Fang, D.** (2019). Drastic tailorable thermal expansion chiral planar and cylindrical shell structures explored with finite element simulation, *Composite Structures*, *210*, 327–338.

[35] **Lakes, R.** (1987). Foam structures with a negative Poisson's ratio, *Science*, *235*, 1038–1041.

[36] **Alderson, A.**, **Alderson, K.L.**, **Attard, D.**, **Evans, K.E.**, **Gatt, R.**, **Grima, J.N.**, **Miller, W.**, **Ravirala, N.**, **Smith, C. and Zied, K.** (2010). Elastic constants of 3-, 4-and 6-connected chiral and anti-chiral honeycombs subject to uniaxial in-plane loading, *Composites Science and Technology*, *70*(7), 1042–1048.

[37] **Dirrenberger, J.**, **Forest, S. and Jeulin, D.** (2013). Effective elastic properties of auxetic microstructures: anisotropy and structural applications, *International Journal of Mechanics and Materials in Design*, *9*(1), 21–33.

[38] **Grima, J.N.**, **Chetcuti, E.**, **Manicaro, E.**, **Attard, D.**, **Camilleri, M.**, **Gatt, R. and Evans, K.E.** (2012). On the auxetic properties of generic rotating rigid triangles, *Proceedings of the Royal Society A: Mathematical, Physical and Engineering Sciences*, *468*(2139), 810–830.

[39] **Liu, W.**, **Wang, N.**, **Huang, J. and Zhong, H.** (2014). The effect of irregularity, residual convex units and stresses on the effective mechanical properties of 2D auxetic cellular structure, *Materials Science and Engineering: A*, *609*, 26–33.

[40] **Hou, Y.**, **Neville, R.**, **Scarpa, F.**, **Remillat, C.**, **Gu, B. and Ruzzene, M.** (2014). Graded conventional-auxetic Kirigami sandwich structures: Flatwise compression and edgewise loading, *Composites Part B: Engineering*, *59*, 33–42.

[41] **Liu, Y. and Hu, H.** (2010). A review on auxetic structures and polymeric materials, *Scientific Research and Essays*, *5*(10), 1052–1063.

[42] **Mir, M.**, **Ali, M.N.**, **Sami, J. and Ansari, U.** (2014). Review of mechanics and applications of auxetic structures, *Advances in Materials Science and Engineering*, *2014*.

[43] **Yang, W.**, **Li, Z.M.**, **Shi, W.**, **Xie, B.H. and Yang, M.B.** (2004). Review on auxetic materials, *Journal of materials science*, *39*(10), 3269–3279.

[44] **Duncan, O.**, **Foster, L.**, **Senior, T.**, **Allen, T. and Alderson, A.** (2016). A comparison of novel and conventional fabrication methods for auxetic foams for sports safety applications, *Procedia engineering*, *147*, 384–389.

[45] **Wang, X.T.**, **Li, X.W. and Ma, L.** (2016). Interlocking assembled 3D auxetic cellular structures, *Materials & Design*, *99*, 467–476.

[46] **Li, Y. and Zeng, C.** (2016). On the successful fabrication of auxetic polyurethane foams: Materials requirement, processing strategy and conversion mechanism, *Polymer*, *87*, 98–107.

[47] **Duncan, O.**, **Allen, T.**, **Foster, L.**, **Senior, T. and Alderson, A.** (2017). Fabrication, characterisation and modelling of uniform and gradient auxetic foam sheets, *Acta Materialia*, *126*, 426–437.

[48] **Yuan, S.**, **Shen, F.**, **Bai, J.**, **Chua, C.K.**, **Wei, J. and Zhou, K.** (2017). 3D soft auxetic lattice structures fabricated by selective laser sintering: TPU powder evaluation and process optimization, *Materials & Design*, *120*, 317–327.

[49] **Gibson, L.J. and Ashby, M.F.** (1999). *Cellular solids: structure and properties*, Cambridge university press.

[50] **Nakamoto, H.**, **Adachi, T. and Higuchi, M.** (2013). Approximate analysis of progressive deformation in honeycomb structures subjected to in-plane loading, *Archive of Applied Mechanics*, *83*(3), 379–396.

[51] **Zhou, Z.**, **Zhou, J. and Fan, H.** (2017). Plastic analyses of thin-walled steel honeycombs with re-entrant deformation style, *Materials Science and Engineering: A*, *688*, 123–133.

[52] **Assidi, M. and Ganghoffer, J.F.** (2012). Composites with auxetic inclusions showing both an auxetic behavior and enhancement of their mechanical properties, *Composite Structures*, *94*(8), 2373–2382.

[53] **Gonella, S. and Ruzzene, M.** (2008). Homogenization and equivalent in-plane properties of two-dimensional periodic lattices, *International Journal of Solids and Structures*, *45*(10), 2897–2915.

[54] **Bacigalupo, A. and De Bellis, M.L.** (2015). Auxetic anti-tetrachiral materials: equivalent elastic properties and frequency band-gaps, *Composite Structures*, *131*, 530–544.

[55] **Lorato, A.**, **Innocenti, P.**, **Scarpa, F.**, **Alderson, A.**, **Alderson, K.**, **Zied, K.**, **Ravirala, N.**, **Miller, W.**, **Smith, C. and Evans, K.** (2010). The transverse elastic properties of chiral honeycombs, *Composites Science and Technology*, *70*(7), 1057–1063.

[56] **Lira, C.**, **Scarpa, F.**, **Tai, Y. and Yates, J.** (2011). Transverse shear modulus of SILICOMB cellular structures, *Composites Science and Technology*, *71*(9), 1236–1241.

[57] **Wu, W.**, **Tao, Y.**, **Xia, Y.**, **Chen, J.**, **Lei, H.**, **Sun, L. and Fang, D.** (2017). Mechanical properties of hierarchical anti-tetrachiral metastructures, *Extreme Mechanics Letters*, *16*, 18–32.

[58] **Hu, L.**, **Wu, Z. and Fu, M.** (2018). Mechanical behavior of anti-trichiral honeycombs under lateral crushing, *International Journal of Mechanical Sciences*, *140*, 537–546.

[59] **Hu, L.**, **Luo, Z.**, **Zhang, Z.**, **Lian, M. and Huang, L.** (2019). Mechanical property of re-entrant anti-trichiral honeycombs under large deformation, *Composites Part B: Engineering*, *163*, 107–120.

[60] **Xia, R.**, **Song, X.**, **Sun, L.**, **Wu, W.**, **Li, C.**, **Cheng, T. and Qian, G.** (2018). Mechanical Properties of 3D Isotropic Anti-Tetrachiral Metastructure, *physica status solidi (b)*, *255*(4), 1700343.

[61] **Wu, W.**, **Qi, D.**, **Liao, H.**, **Qian, G.**, **Geng, L.**, **Niu, Y. and Liang, J.** (2018). Deformation mechanism of innovative 3D chiral metamaterials, *Scientific reports*, *8*(1), 1–10.

[62] **Chen, Y. and Fu, M.H.** (2017). A novel three-dimensional auxetic lattice meta-material with enhanced stiffness, *Smart Materials and Structures*, *26*(10), 105029.

[63] **Ren, X.**, **Shen, J.**, **Tran, P.**, **Ngo, T.D. and Xie, Y.M.** (2018). Design and characterisation of a tuneable 3D buckling-induced auxetic metamaterial, *Materials & Design*, *139*, 336–342.

[64] **Dong, Z.**, **Li, Y.**, **Zhao, T.**, **Wu, W.**, **Xiao, D. and Liang, J.** (2019). Experimental and numerical studies on the compressive mechanical properties of the metallic auxetic reentrant honeycomb, *Materials & Design*, *182*, 108036.

[65] **Xiao, D.**, **Dong, Z.**, **Li, Y.**, **Wu, W. and Fang, D.** (2019). Compression behavior of the graded metallic auxetic reentrant honeycomb: experiment and finite element analysis, *Materials Science and Engineering: A*, *758*, 163–171.

[66] **Xiao, D.**, **Kang, X.**, **Li, Y.**, **Wu, W.**, **Lu, J.**, **Zhao, G. and Fang, D.** (2019). Insight into the negative Poisson's ratio effect of metallic auxetic reentrant honeycomb under dynamic compression, *Materials Science and Engineering: A*, *763*, 138151.

[67] **Caulfield, B.**, **McHugh, P.E. and Lohfeld, S.** (2007). Dependence of mechanical properties of polyamide components on build parameters in the SLS process, *Journal of Materials Processing Technology*, *182*(1-3), 477–488.

[68] **Anitha, R.**, **Arunachalam, S. and Radhakrishnan, P.** (2001). Critical parameters influencing the quality of prototypes in fused deposition modelling, *Journal of Materials Processing Technology*, *118*(1-3), 385–388.

[69] **Bourell, D.**, **Leu, M. and Rosen, D.** (2009). Identifying the Future of Freeform Processing 2009, *Rapid Prototyp. J*, *92*.

[70] **Chua, C.**, **Feng, C.**, **Lee, C. and Ang, G.** (2005). Rapid investment casting: direct and indirect approaches via model maker II, *The International Journal of Advanced Manufacturing Technology*, *25*(1-2), 26–32.

[71] **Upcraft, S. and Fletcher, R.** (2003). The rapid prototyping technologies, *Assembly Automation*.

[72] **Wang, T.M.**, **Xi, J.T. and Jin, Y.** (2007). A model research for prototype warp deformation in the FDM process, *The International Journal of Advanced Manufacturing Technology*, *33*(11-12), 1087–1096.

[73] **Chennakesava, P. and Narayan, Y.S.** (2014). Fused deposition modeling-insights, *Proceedings of the International Conference on Advances in Design and Manufacturing ICAD&M*, volume 14, pp.1345–1350.

[74] **Volpato, N.**, **Foggiatto, J.A. and Schwarz, D.C.** (2014). The influence of support base on FDM accuracy in Z, *Rapid prototyping journal*.

[75] **Crump, S.S.** (1991). Fast, precise, safe prototypes with FDM, *ASME, PED*, *50*, 53–60.

[76] **Hsieh, P.**, **Tsai, C.**, **Liu, B.**, **Wei, W.**, **Wang, A. and Luo, R.** (2016). 3D printing of low melting temperature alloys by fused deposition modeling, *2016 IEEE International Conference on Industrial Technology (ICIT)*, IEEE, pp.1138–1142.

[77] **Au, S. and Wright, P.K.** (1993). Comparative study of rapid prototyping technology, *ASME DES ENG DIV PUBL DE, ASME, NEW YORK, NY,(USA), 1993,*, *66*, 73–82.

[78] **Pham, D. and Dimov, S.S.** (2012). *Rapid manufacturing: the technologies and applications of rapid prototyping and rapid tooling*, Springer Science & Business Media.

[79] **Baumann, F. and Roller, D.** (2016). Vision based error detection for 3D printing processes, *MATEC web of conferences*, volume 59, EDP Sciences, p.06003.

[80] **Bochmann, L.**, **Bayley, C.**, **Helu, M.**, **Transchel, R.**, **Wegener, K. and Dornfeld, D.** (2015). Understanding error generation in fused deposition modeling, *Surface Topography: Metrology and Properties*, *3*(1), 014002.

[81] **Ahn, S.H.**, **Montero, M.**, **Odell, D.**, **Roundy, S. and Wright, P.K.** (2002). Anisotropic material properties of fused deposition modeling ABS, *Rapid prototyping journal*.

[82] **Montero, M.**, **Roundy, S.**, **Odell, D.**, **Ahn, S.H. and Wright, P.K.** (2001). Material characterization of fused deposition modeling (FDM) ABS by designed experiments, *Society of Manufacturing Engineers*, *10*(13552540210441166).

[83] **Tymrak, B.**, **Kreiger, M. and Pearce, J.M.** (2014). Mechanical properties of components fabricated with open-source 3-D printers under realistic environmental conditions, *Materials & Design*, *58*, 242–246.

[84] **Dawoud, M.**, **Taha, I. and Ebeid, S.J.** (2016). Mechanical behaviour of ABS: An experimental study using FDM and injection moulding techniques, *Journal of Manufacturing Processes*, *21*, 39–45.

[85] **Zou, R.**, **Xia, Y.**, **Liu, S.**, **Hu, P.**, **Hou, W.**, **Hu, Q. and Shan, C.** (2016). Isotropic and anisotropic elasticity and yielding of 3D printed material, *Composites Part B: Engineering*, *99*, 506–513.

[86] **Kolken, H.M. and Zadpoor, A.** (2017). Auxetic mechanical metamaterials, *RSC advances*, *7*(9), 5111–5129.

[87] **Evans, A.G.**, **He, M.**, **Deshpande, V.S.**, **Hutchinson, J.W.**, **Jacobsen, A.J. and Carter, W.B.** (2010). Concepts for enhanced energy absorption using hollow micro-lattices, *International Journal of Impact Engineering*, *37*(9), 947–959.

[88] **Ajdari, A.**, **Nayeb-Hashemi, H. and Vaziri, A.** (2011). Dynamic crushing and energy absorption of regular, irregular and functionally graded cellular structures, *International Journal of Solids and Structures*, *48*(3-4), 506–516.

[89] **Günaydın, K.**, **Eren, Z.**, **Türkmen, H.S.**, **Kazancı, Z. and Scarpa, F.** (2017). Axial low velocity impact response of anisotropic anti-tetrachiral filling lattices, *7th International Conference on Mechanics and Materials in Design*, June, pp.1053–1060.

[90] (2014). Material Data Sheet: Z-ABS.

[91] (2013). ABAQUS Manual.

[92] **Nieh, T.**, **Higashi, K. and Wadsworth, J.** (2000). Effect of cell morphology on the compressive properties of open-cell aluminum foams, *Materials Science and Engineering: A*, *283*(1-2), 105–110.

[93] **Paul, A. and Ramamurty, U.** (2000). Strain rate sensitivity of a closed-cell aluminum foam, *Materials Science and Engineering: A*, *281*(1-2), 1–7.

[94] **Chan, K. and Xie, L.** (2003). Dependency of densification properties on cell topology of metal foams, *Scripta materialia*, *48*(8), 1147–1152.

[95] **Vural, M. and Ravichandran, G.** (2003). Microstructural aspects and modeling of failure in naturally occurring porous composites, *Mechanics of materials*, *35*(3-6), 523–536.

[96] **Günaydin, K.**, **Eren, Z. and Scarpa, F.** (2017). Experimental investigation of auxetic structures subjected to quasi static axial load, *2017 8th International Conference on Recent Advances in Space Technologies (RAST)*, IEEE, pp.7–10.

[97] **Li, Q.**, **Magkiriadis, I. and Harrigan, J.J.** (2006). Compressive strain at the onset of densification of cellular solids, *Journal of cellular plastics*, *42*(5), 371–392.

[98] **Jacob, G.C.**, **Fellers, J.F.**, **Simunovic, S. and Starbuck, J.M.** (2002). Energy absorption in polymer composites for automotive crashworthiness, *Journal of composite materials*, *36*(7), 813–850.

[99] **Gideon, R.K.**, **Sun, B. and Gu, B.** (2016). Mechanical behaviors of four-step 1×1 braided carbon/epoxy three-dimensional composite tubes under axial compression loading, *Polymer Composites*, *37*(11), 3210–3218.

[100] **Lopes, C.**, **Seresta, O.**, **Coquet, Y.**, **Gürdal, Z.**, **Camanho, P. and Thuis, B.** (2009). Low-velocity impact damage on dispersed stacking sequence laminates. Part I: Experiments, *Composites Science and Technology*, *69*(7-8), 926–936.

[101] **Lopes, C.**, **Camanho, P.**, **Gürdal, Z.**, **Maimí, P. and González, E.** (2009). Low-velocity impact damage on dispersed stacking sequence laminates. Part II: Numerical simulations, *Composites Science and Technology*, *69*(7-8), 937–947.

[102] **Caminero, M.**, **Rodríguez, G. and Muñoz, V.** (2016). Effect of stacking sequence on Charpy impact and flexural damage behavior of composite laminates, *Composite Structures*, *136*, 345–357.

[103] **Asaee, Z. and Taheri, F.** (2016). Experimental and numerical investigation into the influence of stacking sequence on the low-velocity impact response of new 3D FMLs, *Composite Structures*, *140*, 136–146.

[104] **Hongkarnjanakul, N.**, **Bouvet, C. and Rivallant, S.** (2013). Validation of low velocity impact modelling on different stacking sequences of CFRP laminates and influence of fibre failure, *Composite Structures*, *106*, 549–559.

[105] **Riccio, A.**, **Di Felice, G.**, **Saputo, S. and Scaramuzzino, F.** (2014). Stacking sequence effects on damage onset in composite laminate subjected to low velocity impact, *Procedia Eng*, *88*(1), 222–229.

[106] **Siromani, D.**, **Henderson, G.**, **Mikita, D.**, **Mirarchi, K.**, **Park, R.**, **Smolko, J.**, **Awerbuch, J. and Tan, T.M.** (2014). An experimental study on the effect of failure trigger mechanisms on the energy absorption capability of CFRP tubes under axial compression, *Composites Part A: applied science and manufacturing*, *64*, 25–35.

[107] **Song, H.W.**, **Du, X.W. and Zhao, G.F.** (2002). Energy absorption behavior of double-chamfer triggered glass/epoxy circular tubes, *Journal of composite materials*, *36*(18), 2183–2198.

[108] **Garner, D.M. and Adams, D.O.** (2008). Test methods for composites crashworthiness: a review, *Journal of advanced materials*, *40*(4), 5–26.

[109] **Palanivelu, S.**, **Van Paepegem, W.**, **Degrieck, J.**, **Vantomme, J.**, **Kakogiannis, D.**, **Van Ackeren, J.**, **Van Hemelrijck, D. and Wastiels, J.** (2011). Crushing and energy absorption performance of different geometrical shapes of small-scale glass/polyester composite tubes under quasi-static loading conditions, *Composite structures*, *93*(2), 992–1007.

[110] **Czaplicki, M.J.**, **Robertson, R.E. and Thornton, P.H.** (1991). Comparison of bevel and tulip triggered pultruded tubes for energy absorption, *Composites Science and Technology*, *40*(1), 31–46.

[111] **Babbage, J. and Mallick, P.** (2005). Static axial crush performance of unfilled and foam-filled aluminum–composite hybrid tubes, *Composite structures*, *70*(2), 177–184.

[112] **Fairful, A.** (1987). Effects of specimen dimensions on the specific energy absorption of fibre composite tubes, *Proc. of ICCM 6*, 3–36.

[113] **Farley, G.L.** (1986). Effect of fiber and matrix maximum strain on the energy absorption of composite materials, *Journal of composite materials*, *20*(4), 322–334.

[114] **Farley, G.L.** (1986). Effect of specimen geometry on the energy absorption capability of composite materials, *Journal of Composite Materials*, *20*(4), 390–400.

[115] **Hamada, H. and Ramakrishna, S.** (1995). Scaling effects in the energy absorption of carbon-fiber/PEEK composite tubes, *Composites science and technology*, *55*(3), 211–221.

[116] **Gupta, N. and Abbas, H.** (2000). Lateral collapse of composite cylindrical tubes between flat platens, *International Journal of Impact Engineering*, *24*(4), 329–346.

[117] **Ochelski, S.**, **Bogusz, P. and Kiczko, A.** (2012). Static axial crush performance of unfilled and elastomer-filled composite tubes, *Bulletin of the Polish Academy of Sciences: Technical Sciences*, *60*(1), 37–43.

[118] **Jamil, A.**, **Guan, Z. and Cantwell, W.** (2017). The static and dynamic response of CFRP tube reinforced polyurethane, *Composite Structures*, *161*, 85–92.

[119] **Gan, N.**, **Feng, Y.**, **Yin, H.**, **Wen, G.**, **Wang, D. and Huang, X.** (2016). Quasi-static axial crushing experiment study of foam-filled CFRP and aluminum alloy thin-walled structures, *Composite Structures*, *157*, 303–319.

[120] **Bisagni, C.** (2009). Experimental investigation of the collapse modes and energy absorption characteristics of composite tubes, *International journal of crashworthiness*, *14*(4), 365–378.

[121] **Zhu, G.**, **Wang, Z.**, **Huo, X.**, **Cheng, A.**, **Li, G. and Zhou, C.** (2017). Experimental and numerical investigation into axial compressive behaviour of thin-walled structures filled with foams and composite skeleton, *International Journal of Mechanical Sciences*, *122*, 104–119.

[122] **Savona, S.C. and Hogg, P.J.** (2006). Investigation of plate geometry on the crushing of flat composite plates, *Composites Science and Technology*, *66*(11-12), 1639–1650.

[123] **Hashin, Z.** (1980). Failure criteria for unidirectional fiber composites.

[124] **Shin, K.C.**, **Lee, J.J.**, **Kim, K.H.**, **Song, M.C. and Huh, J.S.** (2002). Axial crush and bending collapse of an aluminum/GFRP hybrid square tube and its energy absorption capability, *Composite structures*, *57*(1-4), 279–287.

[125] **Murr, L.**, **Gaytan, S.**, **Medina, F.**, **Martinez, E.**, **Hernandez, D.**, **Martinez, L.**, **Lopez, M.**, **Wicker, R.**, **Collins, S. and Arcam, A.** (2009). Effect of build parameters and build geometries on residual microstructures and mechanical properties of Ti-6Al-4V components built by electron beam melting (EBM), *20th Solid Freeform Fabrication Symposium, Austin, TX, August*, pp.3–5.

[126] **Heinl, P.**, **Rottmair, A.**, **Körner, C. and Singer, R.F.** (2007). Cellular titanium by selective electron beam melting, *Advanced Engineering Materials*, *9*(5), 360–364.

[127] **Hiemenz, J.** (2007). Electron beam melting, *Advanced Materials & Processes*, *165*(3), 45–46.

[128] **Mahale, T.R.** (2009). *Electron beam melting of advanced materials and structures*, North Carolina State University.

[129] **Edwards, P.**, **O'conner, A. and Ramulu, M.** (2013). Electron beam additive manufacturing of titanium components: properties and performance, *Journal of Manufacturing Science and Engineering*, *135*(6), 061016.

[130] **De Formanoir, C.**, **Michotte, S.**, **Rigo, O.**, **Germain, L. and Godet, S.** (2016). Electron beam melted Ti–6Al–4V: Microstructure, texture and mechanical behavior of the as-built and heat-treated material, *Materials Science and Engineering: A*, *652*, 105–119.

[131] **Sieniawski, J.**, **Ziaja, W.**, **Kubiak, K. and Motyka, M.**, (2013). Microstructure and mechanical properties of high strength two-phase titanium alloys, Titanium alloys-advances in properties control, IntechOpen.

[132] Ti6Al4V ELI Titanium Alloy Arcam EBM system, **Technical Report**, www.arcam.com.

[133] **Galarraga, H.**, **Warren, R.J.**, **Lados, D.A.**, **Dehoff, R.R.**, **Kirka, M.M. and Nandwana, P.** (2017). Effects of heat treatments on microstructure and properties of Ti-6Al-4V ELI alloy fabricated by electron beam melting (EBM), *Materials Science and Engineering: A*, *685*, 417–428.

[134] **DebRoy, T.**, **Wei, H.**, **Zuback, J.**, **Mukherjee, T.**, **Elmer, J.**, **Milewski, J.**, **Beese, A.M.**, **Wilson-Heid, A.**, **De, A. and Zhang, W.** (2018). Additive manufacturing of metallic components–process, structure and properties, *Progress in Materials Science*, *92*, 112–224.

[135] **El-Desouky, A.**, **Carter, M.**, **Mahmoudi, M.**, **Elwany, A. and LeBlanc, S.** (2017). Influences of energy density on microstructure and consolidation of selective laser melted bismuth telluride thermoelectric powder, *Journal of Manufacturing Processes*, *25*, 411–417.

[136] **Coeck, S.**, **Bisht, M.**, **Plas, J. and Verbist, F.** (2019). Prediction of lack of fusion porosity in selective laser melting based on melt pool monitoring data, *Additive Manufacturing*, *25*, 347–356.

[137] **Everton, S.K.**, **Hirsch, M.**, **Stravroulakis, P.**, **Leach, R.K. and Clare, A.T.** (2016). Review of in-situ process monitoring and in-situ metrology for metal additive manufacturing, *Materials & Design*, *95*, 431–445.

[138] **Zhang, B.**, **Li, Y. and Bai, Q.** (2017). Defect formation mechanisms in selective laser melting: a review, *Chinese Journal of Mechanical Engineering*, *30*(3), 515–527.

[139] **Thijs, L.**, **Verhaeghe, F.**, **Craeghs, T.**, **Van Humbeeck, J. and Kruth, J.P.** (2010). A study of the microstructural evolution during selective laser melting of Ti–6Al–4V, *Acta materialia*, *58*(9), 3303–3312.

[140] **Tammas-Williams, S.**, **Zhao, H.**, **Léonard, F.**, **Derguti, F.**, **Todd, I. and Prangnell, P.** (2015). XCT analysis of the influence of melt strategies on defect population in Ti–6Al–4V components manufactured by Selective Electron Beam Melting, *Materials Characterization*, *102*, 47–61.

[141] **Tang, M.**, **Pistorius, P.C. and Beuth, J.L.** (2017). Prediction of lack-of-fusion porosity for powder bed fusion, *Additive Manufacturing*, *14*, 39–48.

[142] **Liu, J.**, **Yu, H.**, **Chen, C.**, **Weng, F. and Dai, J.** (2017). Research and development status of laser cladding on magnesium alloys: A review, *Optics and Lasers in Engineering*, *93*, 195–210.

[143] **Darvish, K.**, **Chen, Z. and Pasang, T.** (2016). Reducing lack of fusion during selective laser melting of CoCrMo alloy: Effect of laser power on geometrical features of tracks, *Materials & Design*, *112*, 357–366.

[144] **Du Plessis, A.**, **Yadroitsev, I.**, **Yadroitsava, I. and Le Roux, S.G.** (2018). X-ray microcomputed tomography in additive manufacturing: a review of the current technology and applications, *3D Printing and Additive Manufacturing*, *5*(3), 227–247.

[145] **Ghidini, T. and Bugatti, M.**, (2019), Lecture notes in Additive Manufacturing for Space and Aerospace Applications.

[146] **Prall, D. and Lakes, R.** (1997). Properties of a chiral honeycomb with a Poisson's ratio of -1, *International Journal of Mechanical Sciences*, *39*(3), 305–314.

[147] **Spadoni, A.**, **Ruzzene, M. and Scarpa, F.** (2005). Global and local linear buckling behavior of a chiral cellular structure, *physica status solidi (b)*, *242*(3), 695–709.

[148] **Airoldi, A.**, **Bettini, P.**, **Zazzarini, M. and Scarpa, F.** (2012). Failure and energy absorption of plastic and composite chiral honeycombs, *Structures under Shock and Impact XII*, 101–114.

[149] **Spadoni, A.**, **Ruzzene, M. and Scarpa, F.** (2006). Dynamic response of chiral truss-core assemblies, *Journal of intelligent material systems and structures*, *17*(11), 941–952.

[150] **Tee, K.**, **Spadoni, A.**, **Scarpa, F. and Ruzzene, M.** (2010). Wave propagation in auxetic tetrachiral honeycombs, *Journal of Vibration and Acoustics*, *132*(3), 031007.

[151] **Spadoni, A.**, **Ruzzene, M.**, **Gonella, S. and Scarpa, F.** (2009). Phononic properties of hexagonal chiral lattices, *Wave motion*, *46*(7), 435–450.

[152] **Liu, X.**, **Hu, G.**, **Sun, C. and Huang, G.** (2011). Wave propagation characterization and design of two-dimensional elastic chiral metacomposite, *Journal of Sound and Vibration*, *330*(11), 2536–2553.

[153] **Zhu, Y.**, **Wang, Z.P. and Poh, L.H.** (2018). Auxetic hexachiral structures with wavy ligaments for large elasto-plastic deformation, *Smart Materials and Structures*, *27*(5), 055001.

[154] **Dirrenberger, J.**, **Forest, S. and Jeulin, D.** (2012). Elastoplasticity of auxetic materials, *Computational Materials Science*, *64*, 57–61.

[155] **Bacigalupo, A. and Gambarotta, L.** (2014). Homogenization of periodic hexa-and tetrachiral cellular solids, *Composite Structures*, *116*, 461–476.

[156] **Bettini, P.**, **Airoldi, A.**, **Sala, G.**, **Di Landro, L.**, **Ruzzene, M. and Spadoni, A.** (2010). Composite chiral structures for morphing airfoils: Numerical analyses and development of a manufacturing process, *Composites Part B: Engineering*, *41*(2), 133–147.

[157] **Airoldi, A.**, **Crespi, M.**, **Quaranti, G. and Sala, G.** (2012). Design of a morphing airfoil with composite chiral structure, *Journal of Aircraft*, *49*(4), 1008–1019.

[158] **Airoldi, A.**, **Bettini, P.**, **Panichelli, P.**, **Oktem, M.F. and Sala, G.** (2015). Chiral topologies for composite morphing structures–Part I: Development of a chiral rib for deformable airfoils, *physica status solidi (b)*, *252*(7), 1435–1445.

[159] **Airoldi, A.**, **Bettini, P.**, **Panichelli, P. and Sala, G.** (2015). Chiral topologies for composite morphing structures–Part II: Novel configurations and technological processes, *physica status solidi (b)*, *252*(7), 1446–1454.

[160] **Spadoni, A. and Ruzzene, M.** (2007). Numerical and experimental analysis of the static compliance of chiral truss-core airfoils, *Journal of Mechanics of Materials and Structures*, *2*(5), 965–981.

[161] **Ladani, L.**, **Razmi, J. and Choudhury, S.F.** (2014). Mechanical anisotropy and strain rate dependency behavior of Ti6Al4V produced using E-beam additive fabrication, *Journal of Engineering Materials and Technology*, *136*(3), 031006.

APPENDICES

APPENDIX A.1 : Build Theme for EBM Printed Ti6Al4V ELI
APPENDIX A.2 : Arcam A2 Properties
APPENDIX A.3 : Fixture for chiral cyclic test
APPENDIX A.4 : Subroutine for boundary conditions

APPENDIX A.1: Build Theme for EBM Printed Ti6Al4V ELI

Table A.1 : Build theme for EBM printed Ti6Al4V ELI.

PREHEAT	
Focus offset	70 mA
Heating focus offset	130 mA
Maximum heat time	130 mA
Max adaptive iterations	20

MELT	
Surface temperature	650 C^o

COUNTOURS	
Number of contours	3

Outer (contours)	
Speed	440 mm/s
Current	5 mA
Max Current	5 mA

Multispot	
Speed in square	140000 mm/s

Inner (contours)	
Speed	800 mm/s
Current	10.2 mA
Max Current	10.2 mA
Focus offset	6

Multispot	
Speed in square	100000 mm/s

HATCH	
Hatch type	Square
Line offset	0.2 mm
Hatch depth	0.05 mm

BEAM	
Max current	20 mA
Focus offset	25 mA
Speed function	45

WAFER SUPPORT	
Repetitions	
Minium distance	0.9 mm
Repetitions	2

Multispot	
Speed in square	2

Properties	
Current	5.5 mA
Speed	1600 mm/s
Focus offset	4 mA

APPENDIX A.2: Arcam A2 Properties

Table A.2 : Arcam A2 properties.

Feature	Specification
Build tank volume	250x250x400 mm and 350x350x250 mm (W x D x H)
Maximum build size	200x200x350mm (W x D x H) and 300(diameter)x20mm
Model-to-Part accuracy, long range*	+/- 0.20 mm
Model-to-Part accuracy, short range*	+/- 0.13 mm
Surface finish (vertical & horizontal)**	Ra25/Ra35
Beam power	50-3500 W (continuously variable)
Beam spot size	0.2 mm - 1.0 mm (continuously variable)
EB scan speed	up to 8000 m/s
Build rate**	55/80 cm3 /h (Ti6Al4V)
No. of Beam spots	1-100
Vacuum base pressure	<1*10-4 mBar
Power supply	3 x 400V, 32 A, 7 kW
Size and weight	1850 x 900 x 2200 mm (W x D x H), 1420 kg
Process computer CAD interface	PC
CAD interface	Standard: STL
Network	Ethernet 10/100/1000
Certification	CE

* Long range: 100 mm, short range: 10 mm, measured on Arcam Standard Test Part (ASTP).
** Measured on Arcam Standard Test Part (ASTP) Settings optimized for fine surface quality Settings optimized for high build speed.

APPENDIX A.3: Fixture Design for Chiral Cyclic Test

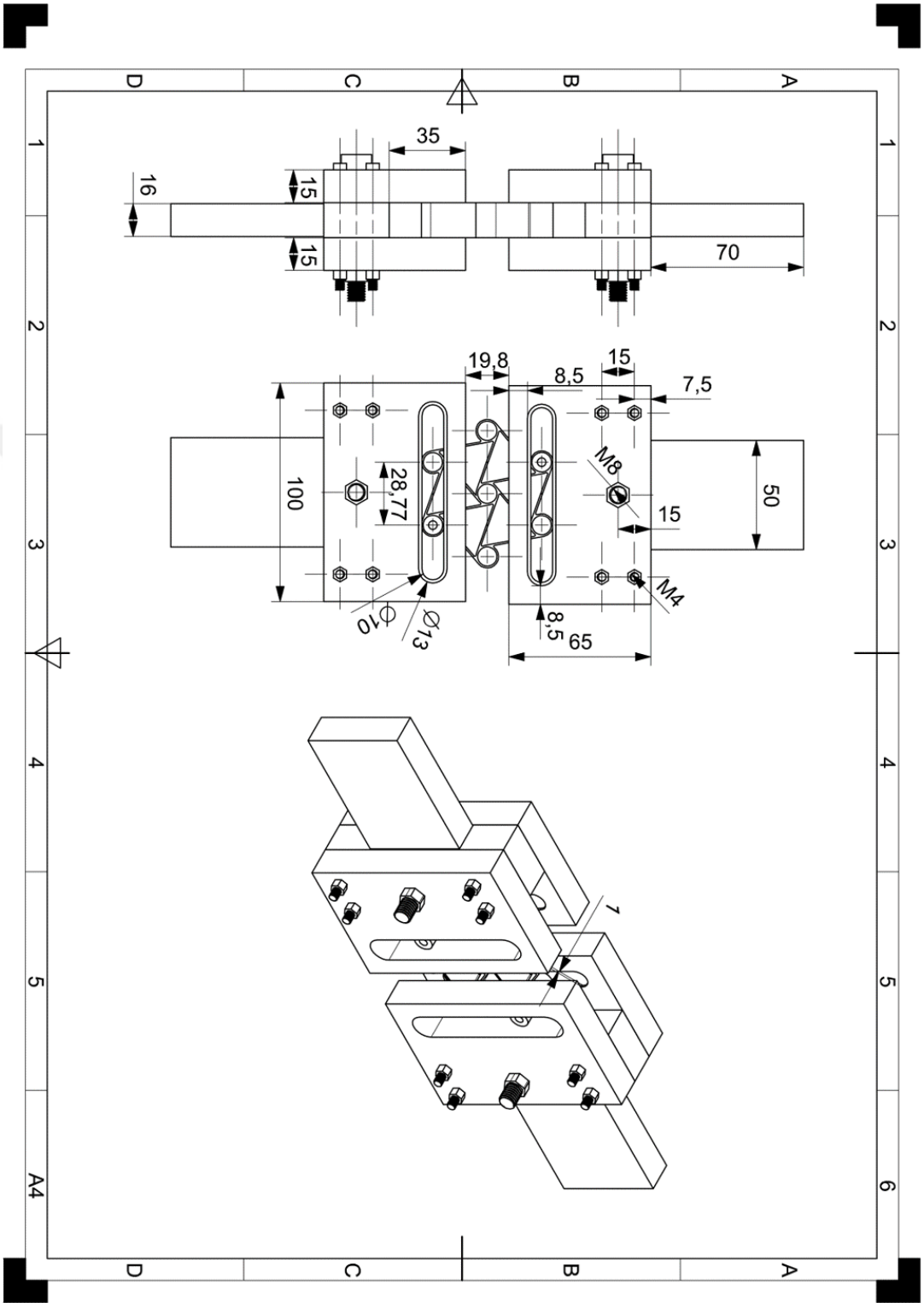

Figure A.1 : Fixture design for chiral cyclic test.

APPENDIX A.4: Subroutine for Boundary Conditions

```
c     user amplitude subroutine
      Subroutine uamp(
C           passed in for information and state variables
     *     ampName, time, ampValueOld, dt, nProps, props,
     nSvars, svars,
     *     lFlagsInfo,nSensor, sensorValues, sensorNames,
     *     jSensorLookUpTable,
C           to be defined
     *     ampValueNew,
     *     lFlagsDefine,
     *     AmpDerivative, AmpSecDerivative, AmpIncIntegral,
     *     AmpIncDoubleIntegral)

      include 'aba_param.inc'

C     svars - additional state variables, similar to (V)UEL
      dimension sensorValues(nSensor), svars(nSvars), props(nProps)
      character*80 sensorNames(nSensor)
      character*80 ampName

C     time indices
      parameter (iStepTime        = 1,
     *           iTotalTime       = 2,
     *           nTime            = 2)
C     flags passed in for information
      parameter (iInitialization   = 1,
     *           iRegularInc       = 2,
     *           nFlagsInfo        = 2)
C     optional flags to be defined
      parameter (iComputeDeriv       = 1,
     *           iComputeSecDeriv    = 2,
     *           iComputeInteg       = 3,
     *           iComputeDoubleInteg = 4,
     *           iStopAnalysis       = 5,
     *           iConcludeStep       = 6,
     *           nFlagsDefine        = 6)

C      Variables used (to be defined )for displacement and force
control
C      maxDisp -> Maximum cross-head displacement
C      targetForce -> Target force value for reloading
C      forceRatio -> Ratio of force between actual and maximum force
C      maxCycles -> Maximum number of cycles
      parameter(maxDisp = 0.7, targetForce = 0.00d0,
     1        forceRatio = 0.10d0, maxLoops = 3)
C
C     Initilialize variables for the procedure
      parameter (zero=0.0d0, one=1.0d0, loading = 1.0,
     1           unloading = -1.0)
      dimension time(nTime), lFlagsInfo(nFlagsInfo),
     1          lFlagsDefine(nFlagsDefine)
      dimension jSensorLookUpTable(*)
C
      integer :: loop
      real :: axialRForce, axialDisplacement, maxRforce
```

```
      real :: fRatio, trigger, utime, Rforce

c     get sensor value
      axialDisplacement  = GetSensorValue('DISPLACEMENT_TRANSDUCER',
     *                                    jSensorLookUpTable,
     *                                    sensorValues)

   axialRForce  = GetSensorValue('FORCE_TRANSDUCER',
     *                                    jSensorLookUpTable,
     *                                    sensorValues)

C
      if (ampName(1:22) .eq. 'LOAD_DISP_CONTROL' ) then
         if (lFlagsInfo(iInitialization).eq. 1) then
            ampValueNew = ampValueOld
         else
            currentTime = time(iStepTime)
         end if
      end if



C ########################################################
C #              BEGIN MAIN PROCEDURE....                #
C ########################################################
C     Estimate the unloading triger point (also time)....
C     A trigger is collected when the maximum displacement (maxDisp)
is achieved
      uTime = svars(1)
      write(7,*), "CURRENT UNLOADING TIME TRIGGER IS->", uTime
      trigger = svars(2)
      write(7,*), "CURRENT PHASE (begining increment) IS ->", trigger
      unloadingTrigger = svars(3)
      write(7,*), "NUMBER OF UNLOADING TRIGGERS IS ->",
      unloadingTrigger
      loop = svars (4)
      write(7,*), "NUMBER OF TOTAL LOOPS IS ->", loop
C     Recall maximum reaction force for the firs loading case
      maxRforce = svars(5)
C     Recall maximum reaction forces for the next cycles
      Rforce = svars(6)
    unitdisplacement=svars(7)
C
   if (loop .eq. 0) then
    aaa=-0.5
    svars(7)=aaa
    else if (loop .eq. 2) then
      bbb=-1.0
      svars(7)=bbb
    else if (loop .eq. 3) then
      ccc=-1.5
      svars(7)=ccc
   end if

      if (axialDisplacement .lt. unitdisplacement) then
       uTime = time(iStepTime)
       write(7,*), "UNLOADING TIME TRIGGER EQUAL TO->", uTime
       trigger = unloading
       svars(1) = uTime
```

```
115         svars(2) = trigger
116 C       Define amplitude value (unloading -> -1)
117         ampValueNew = trigger
118         unloadingTrigger = unloadingTrigger + 1
119         svars(3) = unloadingTrigger
120 C        Loop for estimating the forces at unloading point.
121 
122       write(7,*), "UNLOADING TRIGGER NUMBER EQUAL TO2 ->",
123       1            unloadingTrigger
124 
125         end if
126        write(7,*), "UNLOADING TRIGGER NUMBER EQUAL TO ->",
127       1            unloadingTrigger
128 c
129 c  -----------Displacement limits-----------
130 c  -----------------------------------------
131 C     Control the loading/unloading path
132        if ((svars(2).eq. unloading) .and.
133       1   (axialRForce .lt. targetForce)) then
134         write(7,*), "UNLOADING PHASE..."
135         ampValueNew = unloading
136        else
137          write(7,*), "LOADING PHASE..."
138          ampValueNew = loading
139          trigger = loading
140          svars(2) = trigger
141 C       Count the number of total cycles (loading + unloading)
142          if (axialRForce .gt. targetForce) then
143           loop = loop + 1
144           svars (4) = loop
145           end if
146        end if
147 
148       if (currentTime .ge. 2 .or. axialDisplacement .ge. 1.5) then
149                 lFlagsDefine(iConcludeStep)=1
150              end if
151 
152         return
153         end
154 
155      return M
```

Listing A.1: Subroutine for boundary conditions.

CURRICULUM VITAE

Name Surname: Kadir GÜNAYDIN

Place and Date of Birth: Bor / 01.01.1985

E-Mail: kadirgunaydin@polimi.it, kadirgunaydin@gmail.com

EDUCATION:

- **B.Sc.:** 2008, Erciyes University, Engineering Department, Mechanical Engineering
- **M.Sc.:** 2012, Queen Mary, University of London, School of Engineering and Materials Science, Aerospace Engineering
- **M.B.A.:** 2018, Hasan Kalyoncu University, Faculty of Economics, Administrative Social Sciences, Business Administration

PROFESSIONAL EXPERIENCE AND REWARDS:

- 2010 Cardiff University at the Rapid Protoyping Laboratory.
- 2011 - 2012 M.Sc. Scholarship in Aerospace Engineering, Republic of Turkey Ministry of National Education
- 2015 Ghent University at the Composite Laboratory
- 2017 Computational Methods for the Analysis, Design, and Failure of Composites, International Centre for Mechanical Sciences, Udine, Italy
- 2018 2214-A, International Doctoral Research Fellowship Program, The Scientific and Technological Research Council of Turkey (TÜBİTAK)

PUBLICATIONS, PRESENTATIONS AND PATENTS ON THE THESIS:

- Günaydın K., Eren Z., Kazancı Z., Scarpa F., Grande A. M., Türkmen H. S., 2019. In-plane Compression Behavior of Anti-tetrachiral and Re-entrant lattices. *Smart Materials and Structures*, 28(11), 115028, doi:10.1088/1361-665X/ab47c9.
- Günaydın K., Türkmen H. S., 2019. In-Plane Quasi-Static Crushing Finite Element Analysis of Auxetic Lattices. *9th International Conference on Recent Advances in Space Technologies*, June 11-14, 2019 Istanbul, Turkey, doi: 10.1109/RAST.2019.8767839.
- Günaydın K., Gallina F. G., Airoldi A. A., Sala G., Grande A. M., 2019. Numerical and Experimental Crushing Behaviour Investigation of EBM Printed Auxetic Chiral Lattices. *II International Conference on Simulation for Additive Manufacturing*, September 11-13, 2019 Pavia, Italy.

- Günaydın K., Türkmen H. S., 2018. The Effect of Layer Thickness to the Tensile Stress: Experimental Studies. *International Congress on 3D Printing (Additive Manufacturing) Technologies and Digital Industry*, April 19-211, 2018 Antalya, Turkey.

- Günaydın K., Türkmen H. S., 2018. Common FDM 3D Printing Defects. *International Congress on 3D Printing (Additive Manufacturing) Technologies and Digital Industry*, April 19-211, 2018 Antalya, Turkey.

- Günaydın K., Eren Z., Türkmen H. S., 2018. Quasi-Static Finite Element Analysis of Different Type of Auxetic Lattices. *International Symposium on Dynamic Response and Failure of Composite Materials*, June 12-15, 2018 Ischia, Italy.

- Günaydın K., Eren Z., Türkmen H. S., Scarpa F., 2017. The Crush Performance of Auxetic Filled Composite Tubes. *ASME International Mechanical Engineering Congress Exposition*, November 3-9, 2017 Tampa, Florida, USA.

OTHER PUBLICATIONS, PRESENTATIONS AND PATENTS:

- Usta F., Günaydın K., Türkmen H. S., 2018. Dynamic Impact Behavior of Tapered Nested Tube Structures with and without Imperfection. *2nd International Conference on Impact Loading on Structures and Materials*, May 7-11, 2018 Xi'an, China.

- Günaydın K., Aydın M. D., Türkmen H. S., 2018. The Effect of Adhesives to the Sandwich Structure Crushing Behaviour. *International Symposium on Dynamic Response and Failure of Composite Materials*, June 12-15, 2018 Ischia, Italy.

- Günaydın K., Eren Z., Türkmen H. S., 2018. Dynamic Finite Element Analysis of Auxetic Lattices Filled Tubes. *International Symposium on Dynamic Response and Failure of Composite Materials*, June 12-15, 2018 Ischia, Italy.

- Günaydın K., Eren Z., Türkmen H. S., Kazancı Z., Scarpa F., 2017. Axial Low Velocity Impact Response of Anisotropic Anti-Tetrachiral Filling Lattices. *7th International Conference on Mechanics and Materials in Design*, June 11-15, 2017 Albufeira, Portugal.

- Günaydın K., Eren Z., Scarpa F., 2017. Experimental Investigation of Auxetic Structures Subjected to Quasi Static Axial Load. *8th International Conference on Recent Advances in Space Technologies*, June 19-22, 2017 Istanbul, Turkey, doi: 10.1109/RAST.2017.8002986.

- Günaydın K., Aydın M. D., 2017. The Effect of Different Surface Patterns On The Joint Under Four Point Bending Test. *ASME International Mechanical Engineering Congress Exposition*, November 3-9, 2017 Tampa, Florida, USA.

- Günaydın K., Aydın M. D., 2016. The Effect of Different Surface Patterns on the Joint Strength. *24th Annual International Conference on Composites or Nano Engineering*, June 17-23, 2016 Hainan, China.